



DISSERTATION

EVALUATION OF SPUTTER-DEPOSITED MGO-BASED TUNNELING DIODES FOR SILICON SPINTRONICS

ausgeführt zum Zwecke der Erlangung des akademischen Grades
eines Doktors der technischen Wissenschaften

von

Dipl.Ing.(FH) Thomas Uhrmann

Mat.-Nr. 0527909

Hochstr. 11

D-94121 Salzweg

unter der Leitung von

Ao. Univ. Prof. Dr. rer. nat. Jürgen Smoliner

Technischen Universität Wien

Fakultät für Elektrotechnik und Informationstechnologie

Institut für Festkörperelektronik

Dr. rer. nat. Theodoros Dimopoulos

Austrian Institute of Technology GmbH - AIT

Nano Systems

Salzweg, im Mai 2010

Unterschrift

Erklärung Hiermit versichere ich, dass ich die vorliegende Arbeit selbstständig verfasst und keine anderen als die angegebenen Quellen und Hilfsmittel verwendet habe.

(Thomas Uhrmann)
Salzweg, 5. Mai 2010

Korrektoren:

Ao.Univ.Prof.Mag.rer.nat.Dr.rer.nat Jürgen Smoliner
Ao.Univ.Prof.Dipl.-Ing.Dr.techn. Christoph Eisenmenger-Sittner

Rigorosum: 21. Mai 2010

CONTENTS

Abstract	v
Kurzfassung	vii
Publications and Conference contributions	ix
General Introduction	1
The way to semiconductor spintronics	1
Motivation of this thesis	3
Thesis outline	4
References of General Introduction	8
1 Basics of Spin Injection	9
1.1 Theory of electrical spin injection	9
1.1.1 Spin polarization	9
1.1.2 Spin relaxation	10
1.1.3 Spin transport in all-metallic systems	15
1.1.4 Spin injection in semiconductors	20
1.1.5 Injection through a Schottky barrier	27
1.1.6 Injection through a tunneling barrier	28
1.1.7 Ballistic injection	29
1.2 Characteristic Applications	31
1.3 MRAM concept for silicon spintronics	33
1.3.1 The conventional MRAM design	33
1.3.2 Hybrid MRAM design using spin-polarized current in Si	35
References of Chapter 1	42
2 Experimental techniques	43
2.1 Thin film deposition and patterning	43
2.1.1 Sputter deposition	43
2.1.2 UV lithography	44

2.1.3	Dry etching techniques	45
2.2	Characterization techniques	47
2.2.1	Transmission Electron Microscopy	47
2.2.2	Atomic Force Microscopy	48
2.2.3	Magnetic Force Microscopy	49
2.2.4	Magneto Optical Kerr Effect	50
2.2.5	Electrical transport measurements	52
	References of Chapter 2	54
3	Embedded ferromagnetic silicon diodes	55
3.1	Introduction and scope	55
3.2	Fabrication	57
3.3	Structural characterization	59
3.4	Theoretical background of Schottky and MIS diodes	65
3.5	Electrical characterization of n-Si diodes	70
3.5.1	Ferromagnetic n-Si Schottky diodes	70
3.5.2	Ferromagnetic n-Si MIS tunneling diodes	76
3.6	Electrical characterization of p-Si diodes	81
3.6.1	Ferromagnetic p-Si Schottky diodes	81
3.6.2	Ferromagnetic p-Si MIS tunneling diodes	86
3.7	Discussion	91
3.8	Magnetic characterization	95
3.9	Conclusion	102
	References of Chapter 3	107
4	MgO-based MOS capacitors	109
4.1	Introduction and scope	109
4.2	Fabrication	110
4.3	Structural characterization	111
4.4	Electrical characterization	116
4.5	Conclusion	125
	References of Chapter 4	128
5	Conclusion and Perspectives	129
	List of Figures	135
	List of Tables	139
	Acknowledgements	141
	Curriculum Vitae	143

ABSTRACT

Until today the basic principle of semiconductor devices is the charge manipulation and transfer from one semiconductor region to another, with the metal-oxide-semiconductor field effect transistor (MOSFET) as basic building block for large integrated circuits. The tremendous gain in performance of semiconductor devices has mostly been possible by down-scaling the elements' sizes, following Moore's law, ignoring another inherent property of the electrons: their spin. The conjunction of charge manipulation in the semiconductor with the electron spin could lead to a whole new era in information technology, called *semiconductor spintronics*. The implementation of a so-called spinFET in state-of-the-art CMOS devices is discussed as a possible solution for upcoming scaling limitation. In a spinFET device the conventional source/drain contacts are replaced by ferromagnetic (FM) electrodes, injecting and detecting spin-polarized current in silicon. The main advantage of this approach is the merge of information processing and storage in one device, employing a magneto-current effect that depends on the relative magnetization of the injector and detector electrode. The use of silicon as a host material for spin polarized current features a big advantage: its outstanding spin lifetime.

The present work addresses the fabrication and characterization of sputter-deposited MgO-based tunneling diodes for contact electrodes in such a spinFET device. The so-called conductivity mismatch between the FM contact and silicon is identified as major obstacle for spin injection, which imposes the need of a spin selective interface resistance, such as a Schottky or tunneling barrier. A tunneling barrier inserted at the FM/silicon interface is discussed as most promising solution for the conductivity mismatch, where the diodes' resistance area product has to match a narrow resistance window for successful device implementation.

The structural, electrical and magnetic properties of ferromagnetic Schottky diodes and MgO-based tunneling diodes have been investigated, employing CoFe/NiFe, NiFe and CoFeB ferromagnetic electrodes, different silicon doping densities and different post-deposition annealing conditions. The electrical properties reveal a too high resistance-area product of diodes on n-doped silicon. For low doped p-Si the required resistance-area product is almost matched, where an inversion layer at the interface leads to a vanishing Schottky barrier. Furthermore, it is shown that MgO crystallizes in a cubic phase when deposited on thermally grown SiO₂, which could result in increased spin polarization, while staying amorphous on silicon.

As a result, p-type silicon with a low doping density leads for both spin injection

and spin detection to the most promising results. The results presented in this thesis demonstrate that the close approach of the resistance-area product to the required range, combined with superior dielectric and spin-filtering properties, give the $\text{SiO}_2/\text{MgO}(001)$ bilayer the highest potential for use as tunnel barrier in spinFET ferromagnetic contacts.

KURZFASSUNG

Bis heute besteht das Grundprinzip aller Halbleiterbauelemente in Ladungsträgermanipulation und -transfer zwischen unterschiedlichen Halbleiterregionen, wobei der Metall-Oxid-Halbleiter Feldeffekttransistor (MOSFET) den Grundbaustein für höchstintegrierte Schaltkreise darstellt. Der gewaltige Leistungszuwachs von Halbleiterbauelementen wurde dabei vor allem durch eine Miniaturisierung der Bauteildimensionen erreicht, einem Trend der durch das Moore'sche Gesetz beschrieben wird. In dieser Entwicklung wurde allerdings ein weiterer Freiheitsgrad der Elektronen ignoriert, der Elektronenspin. Die Kombination von Ladungsträgermanipulation mit dem Elektronenspin könnte eine neue Ära der Informationstechnologie einleiten, nämlich die der "Halbleiter Spintronik". Die Integration eines sogenannten spinFET in hochmodernen CMOS Bauelementen wird dabei als eine Lösung diskutiert, um das aufkommenden Miniaturisierungslimit zu umgehen. Bei einem spinFET werden die Source/Drain Kontakte durch magnetische Elektroden ersetzt, welche einen spin-polarisierten Strom in Silizium injizieren bzw. detektieren. Der Hauptvorteil dieses Ansatzes ist die Vereinigung von Datenverarbeitung und Datenspeicherung innerhalb eines einzigen Bauelementes. Dies wird erreicht durch die Verwendung eines Magneto-Strom Effektes, abhängig von der relativen magnetischen Ausrichtung von Injektor und Detektor. Die Verwendung von Silizium als Transportmedium für den spin-polarisierten Strom liefert dabei einen großen Vorteil: eine außerordentlich hohe Spin-Lebensdauer.

Die vorliegende Arbeit beschäftigt sich mit der Herstellung und Charakterisierung von gesputterten, MgO-basierten Tunneldioden, zur Verwendung als magnetische Kontakte eines spinFET. Die größte Hürde stellt hierbei die Fehlanpassung des Widerstandes zwischen Ferromagnet und Silizium dar, was die Verwendung eines spin-selektiven Widerstandes, in der Form einer Schottky- oder Tunnelbarriere, erforderlich macht. Die Verwendung einer Tunnelbarriere wird hierbei als vielversprechendste Lösung angesehen, wobei für die erfolgreiche Umsetzung eines spinFET das Widerstand-Flächen Produkt der Dioden innerhalb eines engen Fensters liegen muss.

Im Rahmen dieser Arbeit wurden die strukturellen, elektrischen und magnetischen Eigenschaften von ferromagnetischen Schottky- und MgO-basierten Tunneldioden untersucht, unter Verwendung von CoFe/NiFe, NiFe und CoFeB Elektroden, unterschiedlicher Siliziumdotierung und thermischer Nachbehandlung. Die elektrischen Diodeneigenschaften im Fall von n-dotiertem Silizium zeigen zu hohe Kontaktwider-

stände. Im Fall von niedrig dotiertem p-Silizium hingegen sind die Kontaktwiderstände nahe dem geforderten Bereich des Widerstand-Flächen Produkts, was durch die Inversion der Silizium Oberfläche und der damit verschwindend kleinen Schottky-Barriere erreicht wird. Des Weiteren konnte gezeigt werden, dass MgO in einer kubischen Phase kristallisiert wenn es auf thermischem SiO₂ abgeschieden wird, wodurch eine höhere Spinpolarisation erreicht werden kann. Bei direkter Abscheidung auf Silizium hingegen bleibt die MgO-Barriere amorph.

Niedrig dotiertes p-Silizium zeigt sowohl für die Injektion als auch Detektion von spin-polarisiertem Strom die vielversprechendsten Resultate. Die gezeigten Ergebnisse belegen, dass die Annäherung an den geforderten Bereich des Widerstands-Flächen Produkts in Verbindung mit den herausragenden dielektrischen und spin-filternden Eigenschaften, der Verwendung einer SiO₂/MgO(001) Doppelbarriere das höchste Potential für den Einsatz in einem spinFET zuteilwerden lassen.

PUBLICATIONS AND CONFERENCE CONTRIBUTIONS

Papers

1. **T. Uhrmann**, T. Dimopoulos, and H. Brückl
"Transport mechanisms of CoFe/MgO/n-Si diodes for spin injection in silicon"
(Letter in preparation)
2. **T. Uhrmann**, T. Dimopoulos, J. Smoliner, and H. Brückl
"Electrical properties of CoFeB/MgO/p-Si diodes for silicon spintronics"
Europhysics Letters (submitted for publication)
3. J. Lee, **T. Uhrmann**, T. Dimopoulos, H. Brückl, and J. Fidler
"TEM Study on Diffusion Process of NiFe Schottky and MgO/NiFe Tunneling Diodes for Spin Injection in Silicon"
IEEE Transactions on Magnetics (accepted for publication Vol.46, No.6, June 2010)
4. A. Kohn, A. Kovacs, **T. Uhrmann**, T. Dimopoulos, and H. Brückl
"Structural and electrical characterization of SiO₂/MgO(001) barriers on Si for a magnetic transistor"
Appl. Phys. Lett. **95** 042506 (2009)
5. **T. Uhrmann**, T. Dimopoulos, A. Kovacs, A. Kohn, S. Weyers, U. Paschen, J. Smoliner, and H. Brückl
"Evaluation of Schottky and MgO-based tunnelling diodes with different ferromagnets for spin injection in n-Si"
J. Phys. D: Appl. Phys. **42** 145114 (2009)
6. T. Dimopoulos, D. Schwarz, **T. Uhrmann**, D. Kirk, A. Kohn, S. Weyers, U. Paschen, and H. Brückl
"Magnetic properties of embedded ferromagnetic contacts to silicon for spin injection"
J. Phys. D: Appl. Phys. **42** 085004 (2009)

7. **T. Uhrmann**, T. Dimopoulos, H. Brückl, V.K. Lazarov, A. Kohn, U. Paschen, S. Weyers, L. Bär, and M. Rührig
 "Characterization of embedded MgO/ferromagnet contacts for spin injection in silicon"
J. Appl. Phys. **103** 063709 (2008)
 selected for Vir. J. Nan. Sci. & Tech. **17** 13 (March 2008)
8. T. Dimopoulos, J. Schotter, **T. Uhrmann**, N. Wiese, R. Heer, C. Stepper, M. Kast, and H. Brückl
 "Fabrication and characterization of sub- μm magnetic cells for embedded front-end MRAM"
J. Magn. Magn. Mat. **316** E948-E952 (2007)

Conference contributions

1. **T. Uhrmann**, T. Dimopoulos, A. Kohn, A. Kovacs, S. Weyers, U. Paschen, J. Smoliner, and H. Brückl
 "Evaluation of Schottky and MgO-based tunneling diodes with different ferromagnets for spin injection in n-Si (001)"
 Spintech V Conference 2009 Krakow, Poland (Poster)
2. P. Schroeder, T. Burchhart, A. Lugstein, **T. Uhrmann**, T. Dimopoulos, and H. Brückl
 "Biomimetic inertia sensor based on nanowires and magnetoresistance"
 Mechanosensors: From Biological to Bionic Systems 2008, Vienna Austria (Poster)
3. **T. Uhrmann**, T. Dimopoulos, D. Schwarz, V.K. Lazarov, A. Kohn, U. Paschen, S. Weyers, and H. Brückl
 "Transport properties of embedded MgO-based MIS diodes for Si spintronics"
 DPG Frühjahrstagung 2008 Berlin, Germany (Talk)
4. D. Schwarz, T. Dimopoulos, **T. Uhrmann**, V.K. Lazarov, A. Kohn, U. Paschen, S. Weyers, and H. Brückl
 "Magnetic characterization of injector / detector contacts for Si spintronics"
 DPG Frühjahrstagung 2008 Berlin, Germany (Talk)
5. A. Kohn, D. Kirk, V.K. Lazarov, A. Kovacs, **T. Uhrmann**, T. Dimopoulos, and H. Brückl
 "Characterization of CoFeB/MgO structures for spin injection in silicon"
 JEMS Conference 2008 Dublin, Ireland (Talk)
6. **T. Uhrmann**, T. Dimopoulos, D. Schwarz, V.K. Lazarov, D. Kirk, A. Kohn, U. Paschen, S. Weyers, and H. Brückl
 "Magnetic characterization of embedded MgO ferromagnetic contacts for spin

- injection in silicon"
Intermag 08 Conference 2008 Madrid, Spain (Talk)
7. T. Dimopoulos, **T. Uhrmann**, D. Schwarz, V.K. Lazarov, D. Kirk, A. Kohn, U. Paschen, S. Weyers, and H. Brückl
"Electrical transport properties of MgO/ferromagnet contacts to p-Si for spin injection and detection"
Intermag 08 Conference 2008 Madrid, Spain (Talk)
 8. V.K. Lazarov, A. Kohn, **T. Uhrmann**, T. Dimopoulos, and H. Brückl
"A TEM structural study of thermal stability of magnetic tunnel junctions integrated with CMOS devices"
EMAG: Electron Microscopy and Analysis Group Conference 2007, Glasgow, U.K. (Talk)
 9. T. Dimopoulos, **T. Uhrmann**, C. Stepper, V.K. Lazarov, A. Kohn, L. Bär, U. Paschen, and H. Brückl
"Spin-polarized transport in silicon using embedded magnetic contacts"
WUN-Spin 07 Conference 2007, York, U.K. (Talk)
 10. **T. Uhrmann**, T. Dimopoulos, C. Stepper, V.K. Lazarov, A. Kohn, L. Bär, U. Paschen, and H. Brückl
"Magnetic and transport properties of embedded magnetic cells for a front-end-of-line MRAM design"
WUN-Spin 07 Conference 2007, York, U.K. (Talk)
 11. V.K. Lazarov, A. Kohn, T. Dimopoulos, **T. Uhrmann**, and H. Brückl
"Structural study of magnetic memory devices embedded in Si"
WUN-Spin 07 Conference 2007, York, U.K. (Poster)
 12. V.K. Lazarov, A. Kohn, T. Dimopoulos, **T. Uhrmann**, H. Brückl, S. Vizzini, H. Oughaddou, H. Achard, F. Arnaud d'Avitaya, and B. Aufray
"A TEM study of thermal stability of magnetic tunnel junctions integrated with CMOS devices"
MMM-Intermag 2007, Baltimore, USA (Poster)
 13. **T. Uhrmann**, T. Dimopoulos, J. Schotter, R. Heer, C. Stepper, M. Kast, V.K. Lazarov, A. Kohn, and H. Brückl
"Magnetic and transport properties of embedded magnetic cells for a front-end MRAM design"
ICPS Conference 2006, Wien, Austria (Poster)
Gordon Research Conference 2006, Oxford, U.K. (Poster)
 14. T. Dimopoulos, J. Schotter, **T. Uhrmann**, R. Heer, C. Stepper, M. Kast, V.K. Lazarov, A. Kohn, and H. Brückl
"Fabrication and characterization of sub-m magnetic cells for embedded front-end MRAM"
Joint European Magnetism Symposia 2006, San Sebastian, Spain (Poster)

GENERAL INTRODUCTION

Until today the basic principle of semiconductor devices is the charge manipulation and transfer from one semiconductor region to another, with the metal oxide semiconductor field effect transistor (MOSFET) as basic building block for large integrated circuits. The tremendous gain in performance of semiconductor devices has mostly been possible by down-scaling of the elements' sizes, following Moore's law [1]. Therefore, the material science went hand in hand with the fabrication technology, pushing the limits to the nanometer scale. One issue arising from this development is the gaining importance of parasitic quantum effects, e.g. increasing tunneling current through the gate oxide. New technological tricks have been introduced in order to further enhance the device performance. However, quantum mechanics and atomic dimensions are introducing a border impossible to cross.

Indeed, the evolution of semiconductors is remarkable; however the information processing is still done through charge transport, ignoring another inherent property of the electrons: their spin. Spintronics refers to the spin-control of electronics and on the same time to the electrical control of the spin itself. The conjunction of charge manipulation in the semiconductor with the electron spin could lead to a whole new era in information technology, called *semiconductor spintronics*.

The research field of *semiconductor spintronics* is rather new, triggered by spintronic effects in all-metallic systems, a history that is introduced briefly in the following.

The way to semiconductor spintronics

Even before quantum mechanics has been introduced, the anisotropic magneto resistance (AMR) has been known as an intrinsic effect in ferromagnetic conductors. The AMR effect is related to a change of the s-d hybridization of the electrons, changing with the magnitude and direction of an applied magnetic field.

In 1971 Tedrow and Meservey [2] have shown, that the spin of a tunneling electron, originating from an Fe layer through an amorphous alumina barrier into superconducting Al, can be conserved. An observation that quickly led to the discovery of the tunneling magneto resistance (TMR) by Jullière in 1975 [3]. The originally used Fe/Ge/Fe trilayer system showed a magneto resistance (MR) amplitude of 14% at

4.2 K. Although, the TMR effect has been already known, the discovery of the giant magneto resistance (GMR) in 1988 by Peter Grünberg and Albert Fert [4, 5], is thought to be the starting point for the research field called "spintronics". A discovery that has been awarded in 2007 with the Nobel Prize in Physics.

The introduction of GMR read heads in hard-drive pushed data storage to a whole new age.

While the conductivity-polarization is determining the GMR, the TMR-effect is linked to the density-polarization. The elaboration of thin film deposition techniques like molecular beam epitaxy (MBE) paved the way for reproducible results on this quantum effect [6].

As a next big step amorphous tunneling barriers, e.g. alumina, were exchanged with a crystalline barrier. Cubic MgO(001) is the most prominent candidate of this group [7, 8, 9], showing extraordinary high effects up to 600% at room temperature [10]. In such systems one certain tunneling electron Bloch wave is selected, commonly referred to as spin filtering. In case of well fitting material combinations the selected spin symmetry can offer almost full spin polarization.

The market hold of the TMR-effect is reasonable low, compared to GMR. Nevertheless, magnetic random access memory (MRAM) devices, exploiting the TMR-effect, found their way to a niche-market featuring non-volatility, radiation hardness and high temperature stability.

Another important experiment has been carried out in 1985 by Johnson and Silsbee, where a spin polarized current has been successfully injected and detected from ferromagnetic contacts in crystalline aluminium, showing a spin diffusion length in the range of 50 μm [11].

The successful spin injection into a metal and the measurable magneto-current effect, initiated the idea to use semiconductors as a host material for spin currents. In 1990 Datta and Das proposed the pioneering concept of a spin field effect transistor (spinFET), giving the starting point to "semiconductor spintronics" (Fig. 0.1) [12]. Spin polarized electrons are injected at the interface from one Fe-electrode into a 2D-electron gas, formed at the interface of (In,Al)As-(In,Ga)As heterostructure. The orientation of the injected spins can be manipulated by Rashba spin-orbit coupling, induced through an electric field from the gate electrode and analyzed by the second ferromagnetic contact. Depending on the relative orientation of the electrode magnetization and the applied gate voltage, the current through the transistor would be modulated.

In semiconductor spintronics, basically three different approaches are considered for generation of a spin-polarized current in a semiconductor.

The first approach is using hybrid structures with ferromagnetic injection and detection contacts to a non-magnetic semiconductor. Already first experiments revealed that the injection of spin polarized electrons is not a trivial task. Schmidt et al. have been the first identifying the "conductivity mismatch" of FM and SC to be the stem of the problem [13]. A theoretic solution has been proposed shortly after [14, 15], to use a spin-dependent interface resistance equilibrating the FM and SC conductivity. Both, Schottky and tunneling barriers, are proven to work in spin LEDs and by magneto-optical experiments [16, 17].

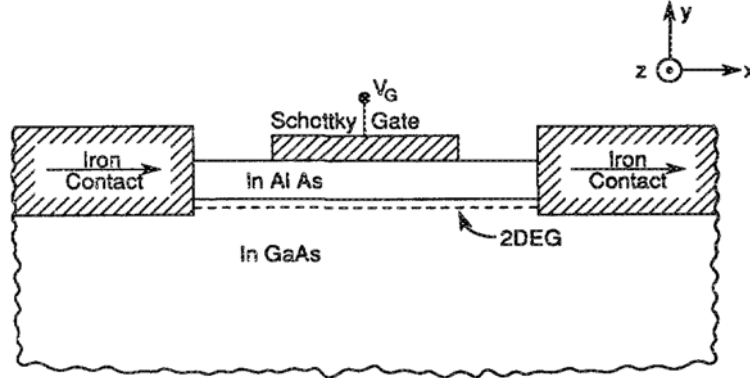


Figure 0.1: *Datta-Das-transistor with a structure similar to a MOSFET device (adapted from [12])*

The second approach is using diluted magnetic semiconductors (DMS). The discovery of the ferromagnetic properties of Mn doped InAs and GaAs gave the starting point for the research on DMS [18, 19]. The control of the magnetic as well as the electrical properties of a semiconductor would come closest to the mean of spintronics [20]. In DMS, the Ga atoms in the basic lattice of GaAs are substituted with Mn acting as acceptor and adding an additional hole. The hole spin and the additional magnetic moment of the Mn-atom align antiparallel. If the concentration of Mn is high enough, the Mn spins align parallel, resulting in a ferromagnetic behavior of the (GaMn)As. The Curie temperature of such alloys are directly proportional to the Mn content and ranging up to 173K [21]. Higher Curie temperatures have not been shown up to now, since from a certain concentration on, the Mn is agglomerating in MnAs clusters or sitting at interstitial places in the GaAs lattice.

Finally, spin-orbit effect, like spin-Hall, Dresselhaus or Rashba effects, can be used to generate a spin-polarized current. The spin-Hall effect, for example, features a spin separation due to spin dependent scattering along a current path. Therefore even non-magnetic semiconductors can be used to generate a spin-polarized current [22, 23, 24].

Although, there is a lot of research work done in this field, the realization of a spinFET has not been achieved, yet. The implementation of spinFETs in today's complementary metal oxide semiconductor (CMOS) circuits is a attractive task. Especially, the conjunction of data-processing and data-storage within the same device is highly interesting.

Motivation of this thesis

The implementation of a spinFET in state of the art CMOS devices is discussed as one possible solution in the ITRS roadmap for the upcoming scaling limitation [25]. The main advantage of this approach is to merge information processing and storage in one structure, due to a magneto current effect depending on the rela-

tive direction of magnetization of the injector and collector electrode. As mentioned above there are different ways for the generation of spin-polarized current in semiconductors. Nevertheless, a hybrid structure featuring ferromagnetic injection and detection contacts to a non-magnetic semiconductor channel is thought to be the most feasible solution from a device point-of-view. The other possibilities, DMS and spin-orbit effects, are restricted to low temperatures, canceling themselves out. The use of silicon as a host material features another big advantage, its outstanding spin lifetime. This is attributed to the absence of a nuclear spin in silicon's main isotope, Si^{28} , as well as the inversion symmetry of silicon's unit cell. The latter results in a low spin-orbit coupling. For these reasons the spin diffusion length of silicon exceeds III-V or II-VI semiconductors by orders of magnitude. On the other hand, the absence of spin-orbit coupling restricts spin-manipulation to magnetic fields in the channel rather than a electric-field introduced by a gate electrode. Having this in mind, the basic transistor layout based for this work is reduced, incorporating only injection and detection electrodes and no gate electrode. A parallel and antiparallel orientation of injector and detector electrode can be achieved by different sized electrodes and hence a different magnetic form anisotropy, leading to different magnetic switching fields. The two adjacent ohmic contact on either side of the magnetic contacts may be used to tailor the band structure and therefore the barrier height of injection and detection [26].

Thesis outline

Following to this general introduction giving a short overview to spintronics research, Chapter 1 expatiates upon the physics needed for semiconductor spintronics. Following the intention to implement a spinFET in current silicon CMOS technology, the different building blocks are individually introduced. Starting with the source of spin polarized current, the ferromagnetic (FM) injection electrode (Section 1.1.1), next the transport and relaxation properties of the silicon host are discussed (Section 1.1.2). As a precursor the spin injection into metals is reconsidered (Section 1.1.3), including the most prominent GMR and TMR effects, which is closely linked to the absorbing topic of spin injection in semiconductors (SC) (Section 1.1.4). From the single FM/SC interface, the picture is extended to a FM/SC/FM two-terminal device geometry. Thereafter realistic injection/detection conditions, comprising Schottky barriers, tunneling barriers or ballistic electron injection, are pictured (Section 1.1.5 - 1.1.7).

Spin currents are already used in metallic systems, therefore the most important device applications are represented. The chapter is enclosed with the Magnetic Random Access Memory (MRAM) concept, firstly in all-metallic systems, followed by the hybrid MRAM device using spin polarized current in silicon.

In Chapter 2 the experimental tools, used in the framework of this thesis, are introduced.

In Chapter 3 the first major part of the experimental work is treated, namely the

characterization of embedded ferromagnetic diodes on silicon. First, their fabrication and the structural characteristics are stretched out. In the following, the magnetic properties sub- μm diodes are studied. Therefore different diode stacks have been deposited, investigating their magnetic switching properties as a function of the ferromagnetic material system, the tunneling barrier thickness and the thermal annealing. Following to the magnetic characterization, the electrical properties of ferromagnetic Schottky and MgO-based tunneling diodes are investigated as a function of the ferromagnetic electrode (CoFe, CoFeB and NiFe), doping-type (n- and p-doped) and doping density (10^{15} to 10^{18}cm^{-3}) as well as their thermal stability. The different diode combinations are discussed for their suitability as spin injection and detection contacts to silicon.

In Chapter 4, the second experimental part, focus is put on the electrical and microstructural properties of MOS capacitors featuring MgO-based dielectrics layers. The aim of this investigation is the growth and characterization of crystalline MgO(001), which is known to show spin filtering properties in combination with the used 3d-ferromagnets.

In Chapter 5 the results found in this thesis are discussed with respect to the needs for obtaining a magneto-current effect using silicon as a host material for spin polarized current.

The thesis is enclosed with the proposal of a future device layout for a MRAM design using a spin-polarized current, with respect to the results gathered in this work.

REFERENCES OF GENERAL INTRODUCTION

- [1] Moore, G. *Electronics* **38**, 19 (1965).
- [2] Tedrow, P. M. and Meservey, R. *Physical Review B* **7**(1), 318–326 (1973).
- [3] Jullière, M. *Physics Letters* **54A**(3), 225 (1975).
- [4] Baibich, M. N., Broto, J. M., Fert, A., Dau, F. N. V., Petroff, F., Eitenne, P., Creuzet, G., Friederich, A., and Chazelas, J. *Physical Review Letters* **61**(21), 2472–2475 (1988).
- [5] Binasch, G., Grünberg, P., Saurenbach, F., and Zinn, W. *Physical Review B* **39**(7), 4829–4831 (1989).
- [6] Moodera, J., Kinder, L. R., Wong, T. M., and Meservey, R. *Physical Review Letters* **74**(16), 3273 (1995).
- [7] Bowen, M., Cros, V., Petroff, F., Fert, A., Boubeta, C. M., Costa-Krämer, J. L., Anguita, J. V., Cebollada, A., Briones, F., de Teresa, J. M., Morellón, L., Ibarra, M. R., Güell, F., Peiró, F., and Cornet, A. *Appl. Phys. Lett.* **79**, 1655 (2001).
- [8] Parkin, S. S. P. *Nature Materials* **3**, 862–867 (2004).
- [9] Yuasa, S., Nagahama, T., Fukushima, A., Suzuki, Y., and Ando, K. *Nature Materials* **3**, 868–871 (2004).
- [10] Lee, Y. M., Hayakawa, J., Ikeda, S., Matsukura, F., and Ohno, H. *Appl. Phys. Lett.* **90**, 212507 (2007).
- [11] Johnson, M. and Silsbee, R. H. *Physical Review Letters* **55**(17), 1790 (1985).
- [12] Datta, S. and Das, B. *Applied Physics Letters* **56**(7), 665 (1990).
- [13] Schmidt, G., Ferrand, D., Molenkamp, L. W., Filip, A. T., and van Wees, B. J. *Physical Review B* **62**(8), 4790 (2000).
- [14] Fert, A. and Jaffrès, H. *Physical Review B* **64**(18), 4420 (2001).

- [15] Rashba, E. I. *Physical Review B* **62**(24), 16267 (2000).
- [16] Stephens, J., Berezovsky, J., McGuire, J. P., Sham, L. J., Gossard, A. C., and Awschalom, D. D. *Phys. Rev. Lett.* **93**(9), 097602 Aug (2004).
- [17] Awschalom, D. D. and Flatté, M. E. *Nature Physics* **3**, 153 (2007).
- [18] Dietl, T., Ohno, H., and and, F. M. *Phys. Rev. B* **63**, 195205 (2001).
- [19] Dietl, T. *Semicond. Sci. Technol.* **17**, 377–392 (2002).
- [20] Ohno, Y., Young, D. K., Beschoten, B., Matsukura, F., Ohno, H., and Awschalom, D. D. *Nature* **402**, 790 (1999).
- [21] Wang, K., Campion, R., Edmonds, K., Sawicki, M., Dietl, T., Foxon, C., and Gallagher, B. *preprint/cond-mat-0411475* (2004).
- [22] Zhang, S. *Phys. Rev. Lett.* **85**(2), 393–396 Jul (2000).
- [23] Kato, Y. K., Myers, R. C., Gossard, A. C., and Awschalom, D. D. *Science* **306**(5703), 1910 – 1913 (2004).
- [24] Koenig, M., Wiedmann, S., Bruene, C., Roth, A., Buhmann, H., Molenkamp, L. W., Qi, X.-L., and Zhang, S.-C. *Science* **318**, 766 (2007).
- [25] *International Technology Roadmap for Semiconductors* , [http: public.itrs.net](http://public.itrs.net).
- [26] Safarov, V. *french patent, No. W0 2004/061856 A2* (2004).

CHAPTER 1

BASICS OF SPIN INJECTION

The introduction lays out the basic theoretical background concerning the physics of a silicon spinFET. We begin with the origin of spin polarization in a ferromagnet and the mechanisms of spin relaxation. We continue with the injection of spin-polarized current in metals and semiconductors. For the latter case, we identify the major obstacle, which is the conductivity mismatch. Contact architectures to overcome this obstacle are presented, focusing on the injection through Schottky barriers, tunneling barriers, as well as on ballistic spin injection. Following, some representative applications based-on spin-polarized currents are presented. Finally, the concept of a hybrid Magnetic Random Access Memory device, utilizing spin polarized current injection and detection in silicon, is illustrated.

1.1 Theory of electrical spin injection

1.1.1 Spin polarization

Electrons are exhibiting a magnetic net moment due to their spin momentum, \mathbf{S} , and their angular momentum, \mathbf{J} .

The reason for ferromagnetic materials to exhibit a measurable magnetic moment is mounted in two quantum-mechanical effects, namely the spin of electrons and the Pauli principle.

The strong localization of the d-electrons is resulting in a large Coulomb repulsion, in case two electrons and with opposite spin occupy the same orbital. For this reason, the parallel alignment of electrons is favored, according to the Pauli principle. On the other hand, the filling of the d-band with electrons of the same spin quantization is increasing the kinetic energy. For energy reduction these two mechanisms have to balance, defining whether ferromagnetic ordering is favored. For ferromagnetic ordering the d-bands are split by the exchange energy E_{ex} [1].

The 4s-electrons are less localized in energy and have a narrow density of states (DOS), resulting in the pronounced charge carrying properties of this band. Depending on the degree of hybridization of 3d and the 4s-electrons the current and density polarization are different for different ferromagnetic metals.

One consequence of these preconditions is that only metals with partially filled d-shell can have a macroscopic magnetic moment, since otherwise spin-up and spin-down components would counterbalance each other. The transition metals Ni, Co and Fe exhibit a measurable magnetization. This splitting is not only causing the materials' magnetic net moment, but also a difference in the DOS, resulting in a difference of the Fermi velocities for spin-up and spin-down electrons.

The density-polarization P_N at the Fermi energy, E_F , is given through the difference in the DOS of the two spin channels $N_\downarrow(E_F)$ and $N_\uparrow(E_F)$:

$$P_N = \frac{N_\uparrow(E_F) - N_\downarrow(E_F)}{N_\uparrow(E_F) + N_\downarrow(E_F)} \quad (1.1)$$

For the case of spin-polarized current injection and ferromagnetic transport phenomena the current-polarization, β , is relevant:

$$\beta = \frac{j_\uparrow - j_\downarrow}{j_\uparrow + j_\downarrow}, \quad (1.2)$$

related to different bulk conductivities $\sigma_{\uparrow,\downarrow}$ for spin-up and spin-down electrons, according to [2]:

$$\sigma_{\uparrow,\downarrow} = eN_{\uparrow,\downarrow}\mu_{\uparrow,\downarrow}, \quad (1.3)$$

where e is the electron charge and $\mu_{\uparrow,\downarrow}$ the spin dependent electron mobility.

For ferromagnetic effects, e.g. spin injection into semiconductors, the GMR-effect or the TMR-effect, different definitions of the spin-polarization are appropriate, clarified in the course of this chapter.

Of course, the degree of spin-polarization of the ferromagnetic material is crucial for the performance of spintronic devices. For this reason, ferromagnetic materials with half-metallic properties hold tremendous technological interest. For half-metallic materials, the occupation probability of one spin sub-band has semiconducting behavior, while the other spin-band has metallic properties. Hence, such materials offer 100% spin-polarization. Different ferromagnetic compound materials like CrO_2 , Heusler alloys such as Fe_3O_4 , Co_2MnSi or manganese perovskite oxides like $\text{La}_{1-x}\text{Sr}_x\text{MnO}_3$ show full bulk spin-polarization [3]. The crystal structure of such materials is very important for their half-metallic character, while interfaces are breaking this symmetry. Indeed, this symmetry interruption is the main reason, that no half-metallic properties have been shown for multilayer structures yet.

1.1.2 Spin relaxation

Spin-relaxation signifies the decay of carrier spin-polarization in metals and semiconductors back to its equilibrium state. Four different spin-relaxation mechanisms for

conduction electrons are especially important, namely the D'yakonov-Perel' mechanism, the Elliot-Yafet mechanism, the Bir-Aronov-Pikus mechanism and the hyperfine interaction.

Figure 1.1 shows an illustration of each mechanism, explained following the excellent review article by ŽUTIČ *et al.* [4]. Thereafter, the exceptional role of silicon as a host material for spin-polarized current is discussed, with respect to spin relaxation.

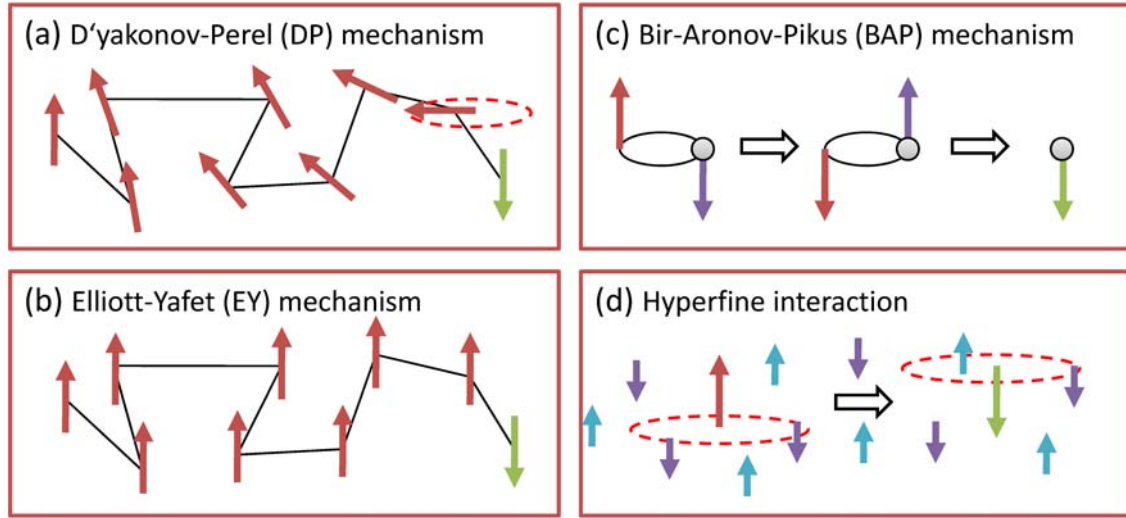


Figure 1.1: Illustration of the different spin relaxation mechanisms: (a) In the D'yakonov-Perel (DP) mechanism the spins precess along a magnetic field depending on the momentum. The frequency and direction of the precession changes randomly with every scattering event. (b) In the Elliott-Yafet (EY) mechanism electrons have a certain chance to flip their spin information by every momentum scattering due to impurities or phonons. (c) In the Bir-Aronov-Pikus (BIP) mechanism the spin of an electron interacts with the spin of a hole. Since spin is conserved, but spin relaxation for holes is faster than for electrons, the spin-information is lost. (d) For confined structures, the electron wave function is confined along with many nuclear spins. The hyperfine interaction results in spin dephasing and relaxation. (adapted from [5])

D'yakonov-Perel' mechanism

The D'yakonov-Perel' (DP) mechanism describes the spin relaxation due to spin-orbit coupling in semiconductors lacking inversion symmetry, e.g. GaAs [6]. Time reversal symmetry dictates that:

$$\mathcal{E}_{n\mathbf{k}\uparrow} = \mathcal{E}_{n-\mathbf{k}\downarrow} \quad (1.4)$$

where \mathbf{k} is the propagation vector and \uparrow, \downarrow the spin orientation. For crystals with inversion symmetry it further holds:

$$\mathcal{E}_{n-\mathbf{k}\uparrow} = \mathcal{E}_{n\mathbf{k}\uparrow} \quad (1.5)$$

As a result from 1.4 and 1.5: $\mathcal{E}_{n\mathbf{k}\uparrow} = \mathcal{E}_{n\mathbf{k}\downarrow}$, meaning that the energy of electrons with the same moment \mathbf{k} but different spin quantization is equal.

However, compound semiconductors, like GaAs, lack inversion symmetry, which translates to:

$$\mathcal{E}_{n-\mathbf{k}\uparrow} \neq \mathcal{E}_{n\mathbf{k}\uparrow} \quad (1.6)$$

In this case 1.4 and 1.6 dictate that: $\mathcal{E}_{n\mathbf{k}\uparrow} \neq \mathcal{E}_{n\mathbf{k}\downarrow}$, resulting in different energies for spin-up and spin-down electrons with the same \mathbf{k} vector. The spin splitting can be described by a \mathbf{k} vector-dependent magnetic field $\mathbf{B}(\mathbf{k})$. The presence of this magnetic field induces electron spin precession, described by the Larmor frequency $\omega = (e/m)|\mathbf{B}(\mathbf{k})|$. Therefore, spin precession can be described by a Hamiltonian in the form:

$$\mathcal{H}(\mathbf{k}) \sim \frac{1}{2}\hbar\boldsymbol{\sigma} \cdot \mathbf{B}(\mathbf{k}) \quad (1.7)$$

where $\boldsymbol{\sigma}$ represents the three Pauli spin matrices. The combination of momentum-dependent spin precession, expressed by $\mathcal{H}(\mathbf{k})$, and momentum scattering with the characteristic momentum relaxation time τ_p , is leading to spin dephasing.

For the conduction of an electron through a crystal without inversion symmetry, the effective magnetic field magnitude and direction are changing randomly with τ_p . The electron rotational angle about the intrinsic field can be described by $\Delta\phi = \omega_{av}\tau_p$, where ω_{av} is the averaged magnitude of the Larmor frequency. Since effective magnetic field change is random, the spin phase is not changing with time, since spin precession is equally probable in clockwise and counterclockwise direction. However, the RMS-value of the spin phase changes over the time, t , according to:

$$(\langle\Delta^2\phi\rangle)^{1/2} \approx (\omega_{av}\tau_p) \left(\frac{t}{\tau_p}\right)^{1/2} \quad (1.8)$$

which is valid for rapid fluctuations with $\omega_{av}\tau_p \ll 1$. This appearance of phase change by random fluctuations is referred to as *motional narrowing* [7].

According to Eq. 1.8 the spin relaxation is defined as the time, τ_s , over which the spin phase fluctuations reach unity:

$$\tau_s = \frac{1}{\omega_{av}^2\tau_p} \quad (1.9)$$

Eq. 1.9 clearly shows that for the D'yakonov-Perel' mechanism the spin relaxation time is decreasing with increasing momentum relaxation time, being the opposite trend to the Elliott-Yafet mechanism, which will be shown in the next section.

The D'yakonov-Perel' mechanism is only present in compound semiconductors, e.g. III-V or II-VI system, while for elemental semiconductors like Si this mechanism is absent.

Elliot-Yafet mechanism

The Elliot-Yafet (EY) mechanism is based on the fact that the spin in the electron wave function of a conduction electron is not a pure spin-up or spin-down state but

an admixture of both due to spin-orbit interaction. According to this, relaxation of electron spins occurs by momentum scattering with phonons or impurities [8, 9]. The Hamiltonian \mathcal{H} of an electron propagating in a crystal potential, $V(\mathbf{r})$, including spin orbit interaction writes:

$$\mathcal{H} = \frac{\mathbf{p}^2}{2m} + V(\mathbf{r}) + \lambda_0 \boldsymbol{\sigma}(\mathbf{p} \cdot \vec{\nabla} V(\mathbf{r})) \quad (1.10)$$

where m is the electron mass, \mathbf{p} the linear momentum operator, $V(\mathbf{r})$ the crystal periodic potential and $\boldsymbol{\sigma}$ is related to the Pauli matrices. The last term of the Hamiltonian accounts for the spin orbit interaction \mathcal{H}_{so} , where λ_0 is a constant. For vanishing spin orbit interaction, $\mathcal{H}_{so} = 0$, Bloch states are spin eigenstates. Though, in reality $\mathcal{H}_{so} \neq 0$ with Bloch states being a admixture of spin-up and spin-down states, so that the wave functions for spin-up and spin-down write [8]:

$$\Psi_{n\mathbf{k}}(\mathbf{r}) = [a_{n\mathbf{k}}(\mathbf{r}) |\uparrow\rangle + b_{n\mathbf{k}}(\mathbf{r}) |\downarrow\rangle] e^{i\mathbf{k}\mathbf{r}} \quad (1.11)$$

where a and b are complex coefficients with the lattice periodicity and \mathbf{r} is the radius vector. It still makes sense to identify spin-up and spin-down states, since one of the coefficients a or b is much smaller than unity. typically $|a|$ is close to unity while $|b| \ll 1$.

Electron states of opposite spin and the same \mathbf{k} can couple via spin orbit interaction. \mathcal{H}_{so} has the period the crystal lattice and is increasing with increasing atomic number. In general, the spin-orbit term in the Hamiltonian is small. However, in combination with momentum scattering the spin-up and spin-down states can efficiently coupled, leading to spin relaxation. Most importantly, phonons, impurities and boundaries can enhance momentum scattering and consequently spin-flip scattering. The spin relaxation time τ_s can be formulated [8]:

$$\tau_s \sim \tau_p (\Delta E / \lambda)^2 \quad (1.12)$$

where τ_p is the momentum relaxation time, λ the spin-orbit coupling amplitude and ΔE the energy separation to the next band with the same symmetry.

The spin relaxation time can be two to six orders of magnitude larger than the momentum relaxation time. For this reason, the spin diffusion length of different semiconductors and metals is highly different. For example, semiconductors or noble metals can show spin diffusion length in the micrometer scale ¹. In contrast to that, ferromagnetic metals have a comparably smaller spin flip time, due to larger spin-orbit interaction, and therefore the spin diffusion length is in range of some tens of nanometers. An increasing doping density of semiconductors is resulting in an increase of momentum scattering, leading to increased spin relaxation.

In general, the EY relaxation mechanism is dominant in semiconductors with a small band-gap with a high spin-orbit coupling and is gaining importance for increasing doping densities.

¹This result is important for spin injection in metals, where Cu and noble metals are used as transport medium for spin currents. Also in GMR multilayers the non-magnetic interlayer has to show low spin-scattering.

Bir-Aronov-Pikus mechanism

BIR *et al.* were the first showing spin relaxation of conduction electrons in p-doped semiconductors through momentum scattering accompanied with hole spin exchange interaction, called the Bir-Aronov-Pikus (BAP) mechanism [10].

The electron-hole interaction is describe by the Hamiltonian \mathcal{H} :

$$\mathcal{H} = A \mathbf{S} \times \mathbf{J} \delta(\mathbf{r}) \quad (1.13)$$

where A is proportional to the exchange interaction between conduction and valence states, \mathbf{S} the electron spin operator, \mathbf{J} the angular momentum operator for holes and \mathbf{r} the relative position of holes and electrons.

The electron-hole exchange interaction results in an effective magnetic field, where the electron spin precesses around the fluctuating hole spin. This relaxation mechanism is dependent on the hole-states and, of course, the acceptor doping density N_a of the semiconductor. For this reason, the spin relaxation time τ_s writes:

$$\tau_s \sim 1/N_a \quad (1.14)$$

Especially at low temperatures and in heavily p-doped semiconductors the Bir-Aronov-Pikus relaxation mechanism gains importance.

Hyperfine interaction

For confined states, e.g. quantum dots, hyperfine interaction (HFI) becomes dominant. For this mechanism, the interaction between the magnetic momentum of electrons and nuclei is causing spin scattering [11]. For free electrons present in a bulk semiconductor, this interaction is weak.

Localized electrons spread over many lattice sites, feeling the magnetic moment of nuclei at every site ($10^4 - 10^6$). Comparing GaAs and silicon, two frequently used semiconductors, the magnetic moment of each lattice site in GaAs is spin 3/2. In contrast, silicon's main isotope, Si^{28} , has no nuclear spin, restricting the hyperfine interaction to Si^{29} , with an abundance of 4.67%, and phosphorus donors, which are both carrying spin 1/2. As a consequence, the magnetic momentum of nuclei in silicon is restricted for localized electrons to around 100 sites. Hence, the hyperfine interaction has very low impact to depolarize the spins.

Silicon as a host for spin-polarized current

For different reasons, silicon is an attractive choice as a host material for spin-polarized currents.

In contrast to zinc-blend semiconductors, like GaAs, silicon's unit cell features inversion symmetry. Therefore the DP-mechanism is absent. As already mentioned,

the DP relaxation is the main reason for the smaller spin lifetime of compound-semiconductors.

Additionally, silicon's main isotope, Si^{28} , has no nuclear spin. As a result, spin-scattering via hyperfine interaction is not an issue.

However, the BAP mechanism may be present, when p-doped silicon is used as a transport medium for spin-polarized electrons.

In conclusion, for n-doped silicon, the EY mechanism is the only remaining mechanism to depolarize the spin-information. For p-doped silicon, however, the EY and the BAP mechanism have to be taken in consideration.

1.1.3 Spin transport in all-metallic systems

Spin transport in all-metallic systems is shown to work in different systems. It is possible to inject and detect spin polarized current in a lateral device geometry, an experiment which has been carried out by JOHNSON and SILSBEE in 1985 [12]. Also the GMR-effect is employing spin-polarized current transport via metallic interlayers, while for the TMR-effect spin-polarized tunneling transport is employed. These three different device structures are reviewed consecutively, offering important concatenation to spin injection in semiconductors.

Johnson-Silsbee experiment

The Johnson-Silsbee experiment is the first evidence of spin-polarized electron injection into a metal, in this case aluminum [12]. A schematic sample layout of the Al-wire and the permalloy injection/detection contacts is shown in Fig. 1.2(a). The data obtained by this experiment have been measured using a non-local measurement geometry.

Spin polarized current is injected at the left FM contact and an electric drift field is applied in the opposite direction to the detection contact. The injection of spin polarized current is causing a spin accumulation under the injection contact. This non-equilibrium spin population is causing a diffusion current spreading hemispherical from the injector, separating the drift current from the spin-diffusion current. A voltage-probe at the detection contact and the far separated end of the sample, where the spin-polarization is equilibrated, is giving a voltage V_s , equivalent to the split in the electrochemical potential under the detection contact. Obviously, the spin diffusion length has to be in the range of the contact spacing for a detectable output signal. Fig. 1.2(b) shows the detection voltage, V_s , for a sweep of the magnetic field, applied along the long-axis of the FM contacts. For large negative as well as large positive magnetic fields the injector/collector pair is parallel magnetized. The marked $B_{0,1}$ and $B_{0,2}$ points reflect the switching fields of the injector and detector contact, respectively, related to a sign change of V_s .

The extraction of the spin diffusion length can be accomplished either by gradually increasing the spacing between injector and detector, which is accompanied by a

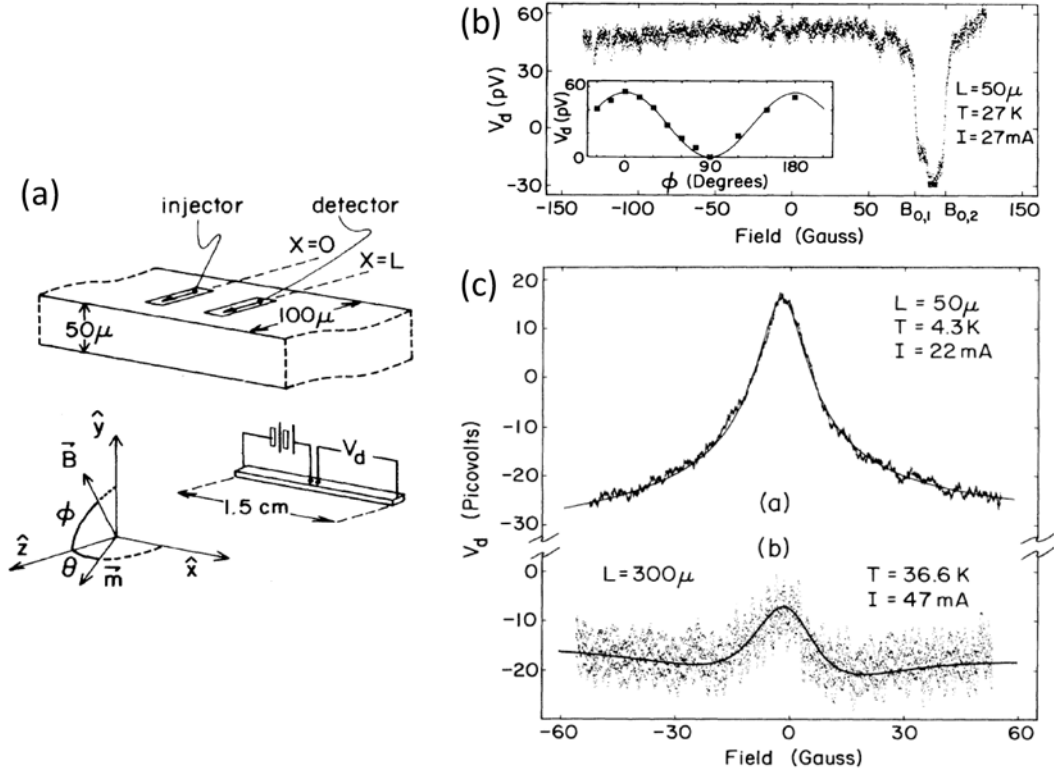


Figure 1.2: (a) Schematic sample layout and probe geometry of the non-local measurement technique. (b) Field sweep vs. detector-voltage V_s of $50\mu\text{m}$ spaced permalloy injection/detection contacts. V_s states the spin-polarization equivalent in a non-local measurement setup. The detected Hanle signal as a function of the orientation-angle ϕ is depicted in the inset. (c) Hanle-curves for different spacing of the injection/detection contacts (adapted from [12])

decrease of V_s [13, 14, 15]. A more efficient way to measure a spin-dependent output signal is by using the Hanle-effect (Fig. 1.2(c)). For this, a magnetic field perpendicular to the magnetization of the injection/detection electrodes is applied, causing a torque on the injected spins, dephasing the spin information as a function of the magnitude and the direction of the applied field. The change in the angle of the applied magnetic bias field gives an oscillatory amplitude of V_s , demonstrating that the Hanle-effect is solely dependent on the perpendicular field component (Fig. 1.2(b)). In such way the spin diffusion length of the injected electrons can be extracted.

Giant Magneto Resistance - GMR

The giant magneto-resistance (GMR) effect has been discovered independently by PETER GRÜNBERG and ALBERT FERT in 1988 [16, 17]. Their work has been awarded with the Nobel Prize in Physics in 2007.

They both found a very large resistance change in alternating ferromagnetic (FM) and non-magnetic metal (NM) Fe/Cr systems, displayed in Fig. 1.3(a). The resis-

tance of such structures is lower for parallel relative alignment of magnetization than for antiparallel alignment. The basic mechanism is the spin-dependent electron scattering in the magnetic layers, according to their relative alignment to the magnetization (Fig. 1.3(b)). A phenomenological explanation is possible according to Mott's two-channel model [18]. In the framework of this theory, spin-up and spin-down electrons are treated as two independent carriers with different conductivities. For parallel alignment the spin-down electrons in a Co/Cr layer-combination have a higher conductivity than the spin-up channel which is subjected to more scattering. Therefore the spin-up channel serves as a shunt resistance, leading to a low resistance. In contrast, for antiparallel alignment each channel has by turns low and high conductivity leading to an increased overall resistance compared to the parallel case. These resistances are defining the magneto-resistance effect $MR = (R_{ap} - R_p)/R_p$, where R_{ap} and R_p are referring to the resistance for antiparallel and parallel magnetic alignment, respectively.

The non-magnetic interlayer serves on one hand as spin transport medium, but also mediates on the other hand the alignment of the magnetic layers by interlayer exchange coupling. The orientation (parallel and antiparallel) and magnetic rigidity of this oscillatory coupling can be set by tuning the non-magnetic spacer thickness [20, 21].

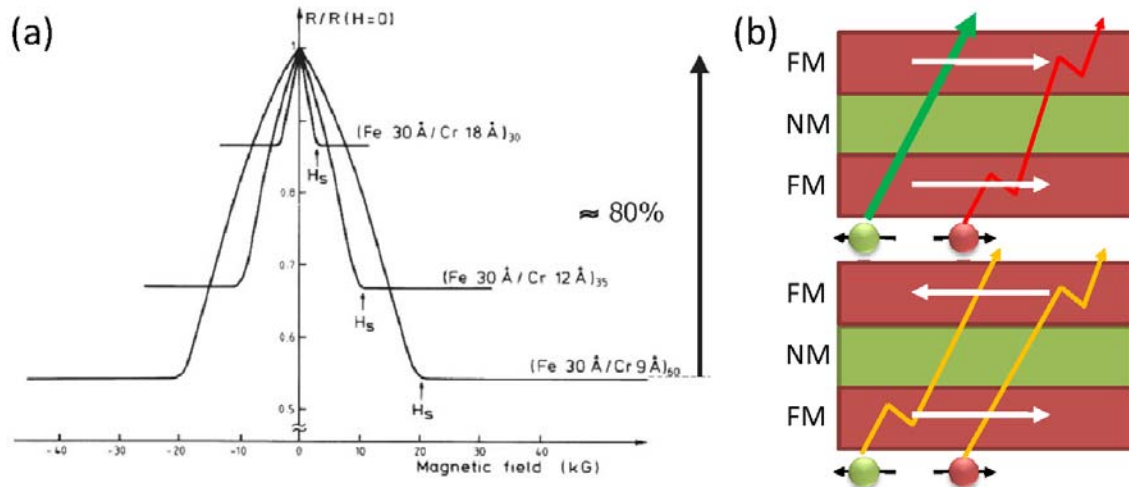


Figure 1.3: (a) Magneto-resistance of Fe/Cr multilayers. (b) Schematic of scattering events in a spinvalve for parallel and antiparallel alignment (adapted from [19])

The impact of this effect is remarkable, used in read-head for hard-drives or magnetic field sensors. While first demonstrating samples elaborated up to 50 Fe/Cr doublelayers, the amount of doublelayers has been further reduced and optimized for different material combinations and different applications [22, 23, 24, 25]. For example, a ferromagnetic/non-magnetic/ferromagnetic metal system is used for read heads and sensor applications. This three layer stack is also known as spin-valve. Through optimization, spin-valves show magneto-resistance effects up to 20% at room-temperature and the switching field can be tuned by engineering of the layer stack as well as structure and size of patterned elements.

Tunneling Magneto Resistance - TMR

The tunneling magneto resistance (TMR) is also discussed in the framework of this section, despite the effect is mounted in spin-dependent tunneling via a thin insulating barrier. For spin injection in semiconductors tunneling diodes are one discussed solution, employing spin polarized tunneling principles and material combinations based on TMR investigations, as discussed later on.

The commonly used device, in order to obtain a TMR effect, is the magnetic tunnel junction (MTJ), consisting of two ferromagnetic electrodes separated by a thin tunneling barrier.

The TMR-effect has been observed for the first time by JULLIÈRE in 1975 in a Fe/Ge/Fe trilayer-system, showing a magneto-resistance (MR) amplitude of 14% at 4.2 K [26]. The introduction of amorphous aluminium oxide tunneling barriers with 3d-ferromagnetic electrodes enabled the observation of TMR-effects at room-temperature [27, 28]. By optimization of the AlOx tunneling barrier and the ferromagnetic stack, MR-effects as high as 70% at RT have been observed [29]. In contrast to the GMR-effect not the current polarization but the density polarization is the crucial parameter for the TMR-effect. The effect is caused by the spin dependent tunneling probability of electrons tunneling through the oxide barrier.

The so-called Jullière-model is directly correlating the MR-amplitude to the density polarization, P_1 and P_2 , of the ferromagnetic electrodes at the Fermi energy, E_F , according to [26]:

$$MR = \frac{R_{ap} - R_p}{R_p} \quad (1.15)$$

$$MR = \frac{2P_1P_2}{1 - P_1P_2} \quad (1.16)$$

In Fig.1.4 the schematic tunneling process, considering the DOS of each spin channel, is sketched for parallel and antiparallel magnetization of the electrodes. The overall current can be described for the parallel case in Fig.1.4(a) by $I \sim N_{1\uparrow}N_{2\uparrow} + N_{1\downarrow}N_{2\downarrow}$ and in the antiparallel case in Fig.1.4(b) by $I \sim N_{1\uparrow}N_{2\downarrow} + N_{1\downarrow}N_{2\uparrow}$, where $N_{x,\uparrow}(E_F)$ and $N_{x,\downarrow}(E_F)$ are the DOS at the Fermi energy, E_F , of majority and minority-spin band of the FM, respectively. Obviously, the current in the parallel case is dominated by the majority carrier contribution, where the DOS is high in both FM layers, leading to a low junction resistance. On the contrary, for antiparallel alignment both spin channels have an equal intermediate conductivity, leading to a larger junction resistance.

Owing to the spin-polarization of 3d-ferromagnets, $P \leq 0.6$, a MR-ratio around 70% marks the so-called Jullière-limit for 3d-ferromagnets. In order to accomplish amplitudes higher than 70%, needed for device operation, different solutions are possible. One proposal is the use of half metallic alloys, featuring a spin polarization of 100%, that should lead, according to Eq. 1.16, to an infinite MR effect. Half metallic properties have already been shown in the bulk, however, their polarization at the interface is lower [3, 31]. Another solution to obtain high MR-effects is the elaboration of coherent spin-dependent transport across crystalline tunneling barriers, like

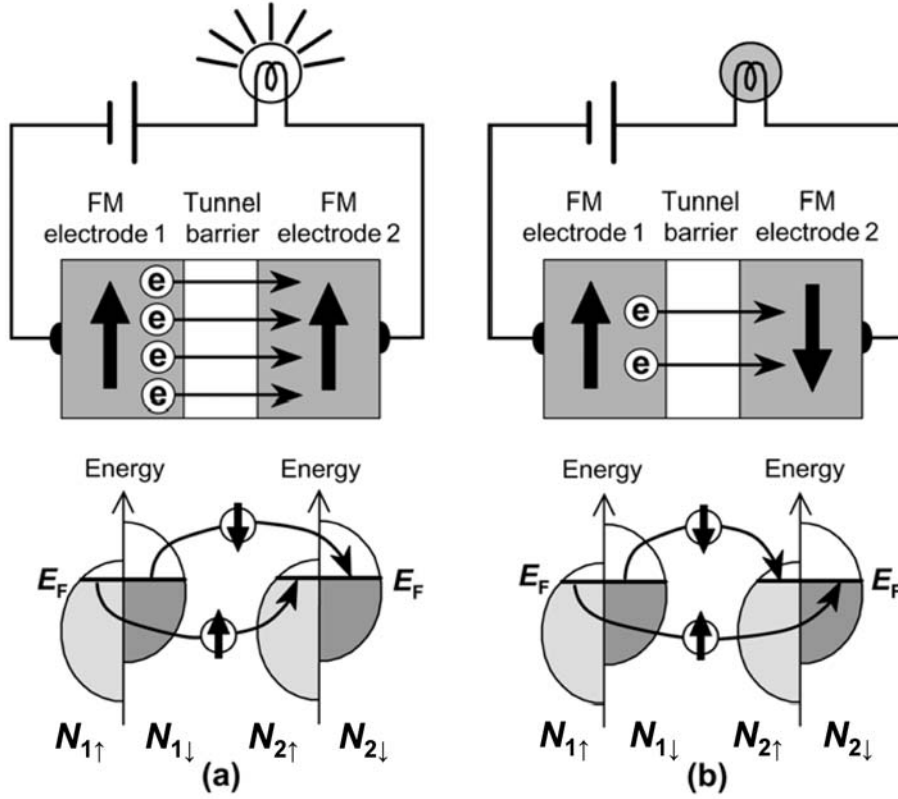


Figure 1.4: Schematic illustration of the TMR-effect for parallel (a) and antiparallel (b) configuration of magnetization. $N_{1/2\uparrow}$ and $N_{1/2\downarrow}$ denote the density of states at the Fermi energy, E_F , for majority-spin and minority-spin bands of both electrodes, respectively (adapted from [30]).

MgO(001).

To understand the coherent tunneling process, a detailed knowledge of the states contributing to the transport is inevitable. Various Bloch states of different symmetries exist in the ferromagnetic electrodes. The Δ_1 state (spd hybridized states) in 3d ferromagnets has generally a large positive spin polarization at E_F . In contrast, the Δ_2 state (pd hybridized states) often have a negative spin polarization. Altogether with the Δ_5 state (d states) the spin polarization of ferromagnetic materials is lower than 1. Fig. 1.5 depicts a schematic of the different current contributions, tunneling through an Al_2O_3 and a MgO(001) barrier in combination with Fe(001). For amorphous tunneling barriers (Fig. 1.5(a)) there exists no structural symmetry. In this case, the different Bloch states (Δ_1 , Δ_2 , Δ_5) can couple to the evanescent states in the barrier, holding comparable tunneling probabilities. This transport is called incoherent tunneling. The earlier described Jullière model assumes, that all the Bloch states have equal tunneling probabilities. However, this assumption is not applicable anymore for coherent tunneling transport, e.g. in the case of MgO(001) tunneling barriers (Fig. 1.5(b)). BUTLER *et al.* have calculated the decay of the ferromagnetic Bloch states for a parallel magnetized Fe(001)/MgO(001)/Fe(001) trilayer (Fig. 1.5 (c)), finding the Δ_1 states' decay rate of the evanescent electron wave function to be

much lower than for the other states. Since the Δ_1 states are featuring a large spin polarization, the current is almost blocked for antiparallel magnetization. Therefore, the obtained MR amplitude for MgO(001) tunneling barriers is exceeding amorphous barriers by far. Indeed, MR-values as high as 1056% in CoFeB/MgO/CoFeB double barrier magnetic tunnel junction have been reported at room-temperature [32].

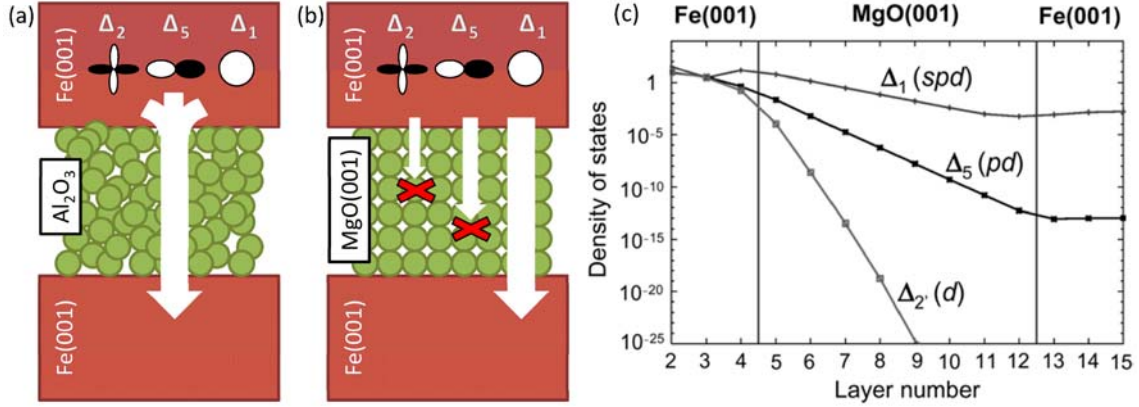


Figure 1.5: Schematic of current contributions tunneling through (a) Al_2O_3 and (b) crystalline $\text{MgO}(001)$ barrier (adapted from [30]). (c) Decay of the available symmetries of Bloch states as a function of the $\text{MgO}(001)$ thickness (adapted from [33])

1.1.4 Spin injection in semiconductors

The indispensable requirement for the implementation of a spinFET, as proposed for the first time by DATTA and DAS in 1990 [34], is the efficient injection of a spin-polarized current into a semiconducting channel. This pioneering concept has already been introduced in the previous chapter, with the basic device layout depicted in Fig. 0.1. However, the implementation of this spin transistor as pure electric analogue of an electro-optical modulator stays still elusive.

Many research groups have tried to set up a spinFET elaborating an InAs heterostructure with ohmic permalloy injection and detection contacts, reporting marginal resistance changes [35, 36, 37, 38, 39, 40]. MONZON *et al.* have shown that the small observed MR ratios can be explained by a local Hall effect under the injection/detection contacts [41]. Later, in a non-local measurement geometry, reducing the spurious local Hall effect and other disturbances, no signal change being related to spin-polarized current transport could be shown [42].

These observations led researchers to realize, that a fundamental problem of ferromagnet-semiconductor contacts hinders efficient spin injection in semiconductors.

Conductivity mismatch

The basic obstacle for spin-polarized current injection from a ferromagnetic metal (FM) into a non-magnetic semiconductor (SC) has been identified by SCHMIDT *et al.* [43]. They showed, that highly different conductivities of FM and SC inhibit efficient spin injection. This problem, commonly known as *conductivity mismatch*, can be intuitively understood with the help of a simple resistor circuit, as shown below.

The conductivity of the semiconductor, σ_{sc} , is not spin dependent, so the partial conductivity of each spin channel, σ_{sc}^\uparrow and σ_{sc}^\downarrow can be written as:

$$\sigma_{sc}^\uparrow = \sigma_{sc}^\downarrow = \frac{\sigma_{sc}}{2} \quad (1.17)$$

Obviously, spin-polarized current can only be introduced in a SC, if a different voltage-drop can be attributed to the different spin channels: $V_\uparrow \neq V_\downarrow$.

In contrast to the SC, 3d-ferromagnets feature direct dependence of the conductivity for each spin channel, depending on the exchange interaction and the hybridization between the 3d and the 4s orbitals. The different conductivity of each ferromagnet spin channel can be expressed with the help of their current polarization β (Eq. 1.2):

$$\sigma_{fm}^\uparrow = \sigma_{fm} \frac{1 + \beta}{2} \quad (1.18)$$

$$\sigma_{fm}^\downarrow = \sigma_{fm} \frac{1 - \beta}{2} \quad (1.19)$$

To introduce spin-polarized current into a semiconductor, a spin-dependent resistance, e.g. a ferromagnet, has to be set in series to the SC. For simplification no spin scattering is considered neither in the ferromagnet nor the semiconductor. Only in this case the spin-up and spin-down electrons can be considered as independent carriers [18]. In realistic systems, the spin diffusion length of semiconductors, especially silicon, is proven to be in the order of micrometers [44, 45]. On the other hand, for the ferromagnetic contacts the spin diffusion length is in the range of tens of nanometers [46].

According to the above, the resistor equivalent of a FM/SC/FM layer stack is a parallel circuit containing two ferromagnetic and one semiconductor resistance for

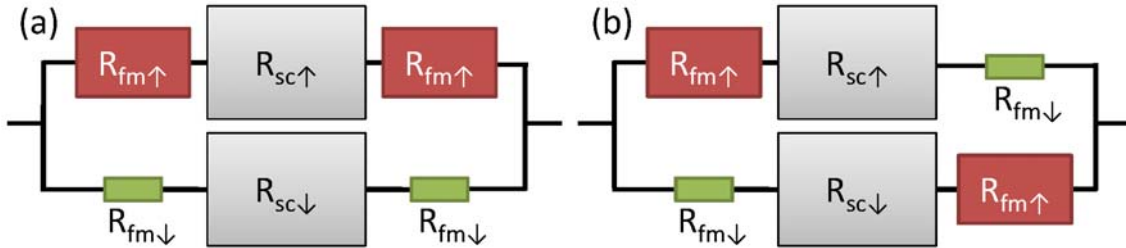


Figure 1.6: Simplified equivalent circuit for a FM/SC/FM hybrid spin-electronic junction in parallel (a) and antiparallel configuration (b)

each spin channel, as displayed in Fig. 1.6.

It can be directly seen, that the current is unpolarized in the case of antiparallel alignment, since the resistances of both spin channels are equal. However, in the case of parallel magnetization the current is spin-polarized. In a simple calculation, using the previously defined resistance values, the spin polarization, α , of the current passing the system can be calculated [47]:

$$\alpha = \beta \frac{R_{fm}}{R_{sc}} \frac{2}{2 \frac{R_{fm}}{R_{sc}} + (1 - \beta^2)} \quad (1.20)$$

The polarization of the overall current α is directly proportional to the spin polarization β , but more important, to the ratio R_{fm}/R_{sc} .

The experimentally accessible value, though, is the magneto-resistance (MR) of the device, being [47]:

$$MR = \frac{R_{antiparallel} - R_{parallel}}{R_{parallel}} = \frac{\beta^2}{1 - \beta^2} \frac{R_{fm}^2}{R_{sc}^2} \frac{4}{\left(2 \frac{R_{fm}}{R_{sc}} + 1\right)^2 - \beta^2} \quad (1.21)$$

In fact, even these equations derived after strong simplifications regarding the spin diffusion length in the FM and SC already show the problem of resistance matching for successful spin injection. In Fig. 1.7 the expectable MR-effect of a FM/SC/FM structure has been calculated for different R_{fm}/R_{sc} ratios as a function of the ferromagnets' current bulk spin polarization, β . In order to see a significant change of the MR-ratio the term R_{fm}^2/R_{sc}^2 is dominant in Eq. 1.21. Since the resistance ratio between FM and SC in reality is around 10^{-4} or less and the spin polarization of the FM is in the range of 50%, the voltage drop over the device mostly happens in the SC, resulting in unpolarized current transport. One

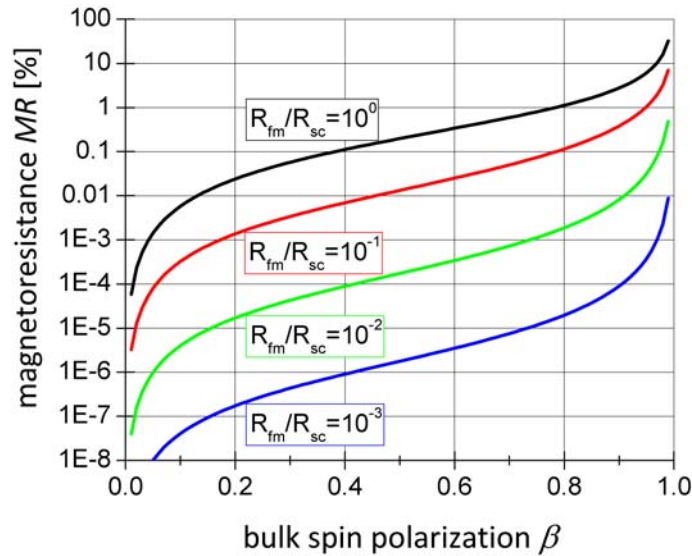


Figure 1.7: Calculation of the expectable MR effect over the spin polarization of the FM for different resistance ratios between FM and SC

possibility to solve the conductivity mismatch problem is the equilibration of R_{sc} and R_{fm} . On the other hand, for a spin polarization β close to 100%, i.e. for half metallic injection/detection contacts, the conductivity mismatch can be overcome as well.

The simple resistor model serves as a basis for the comprehension of the conductivity mismatch issue. For a deeper understanding, a more detailed model is nevertheless needed, as presented in the following.

In the model of FERT and JAFFRÈS the FM/SC interface is considered at flatband condition, where the electric field stemming from the SC space-charge is zero. Fig. 1.8(a) depicts such a contact. On the far left side, in the ferromagnetic bulk, the current is spin-polarized, while in contrast on the right side, in the semiconductor, the current is unpolarized. Close to the interface a transition zone should therefore occur, where mixing of the two spin channels takes place. The spin-accumulation evolution at each side of the FM/SC interface can be derived from the spin-dependent drift-diffusion equations, combined with the spin-dependent continuity equation across the interface [48].

The current density $J_{\uparrow,\downarrow}$ and the electro-chemical potential $\mu_{\uparrow,\downarrow}$ are related with the equations [48]:

$$J_{\uparrow,\downarrow} = \frac{1}{|e|\rho_{\uparrow,\downarrow}} \frac{\partial \mu_{\uparrow,\downarrow}}{\partial z} \quad (1.22)$$

$$J_{\uparrow} + J_{\downarrow} = J \quad (1.23)$$

$$\frac{\partial(J_{\uparrow} - J_{\downarrow})}{\partial z} = \frac{n\Delta\mu}{k_B T} \frac{1}{\tau_s} \quad (1.24)$$

where $\rho_{\uparrow,\downarrow}$ is the spin-dependent resistivity, n the total amount of carriers and $\Delta\mu$ the difference of the electrochemical potential.

Their combination gives the equation for the variation of the electro-chemical potential in z -direction:

$$\frac{\partial^2 \Delta\mu_{\uparrow,\downarrow}}{\partial z^2} = \frac{\Delta\mu_{\uparrow,\downarrow}}{l_{sf}^2} \quad (1.25)$$

The solution of this differential equation yields the spin accumulation at the interface, reflecting the asymmetry of spin populations and expressed as the difference of electrochemical potentials:

$$\Delta\mu = A \exp(-z/l_{sf}^{sc}) + B \exp(z/l_{sf}^{fm}) \quad (1.26)$$

where A and B are constants deriving from the system-dependent boundary conditions. In Fig. 1.8(b) this difference of the electro-chemical potentials is schematically shown.

The spin accumulation degrades away from the interface exponentially over the spin diffusion lengths, l_{sf}^{fm} and l_{sf}^{sc} , of ferromagnet and semiconductor, respectively. For non-degenerated semiconductors l_{sf}^{sc} writes [48]:

$$l_{sf}^{sc} = \sqrt{\frac{k_B T \tau_s}{2ne^2 \rho_{sc}}} \quad (1.27)$$

where k_B is the Boltzmann constant, T the absolute temperature, τ_s the spin relaxation time, n the total number of carriers and ρ_{sc} the semiconductor resistivity. The spin diffusion length of the ferromagnetic contact formulates in a similar way [49]. For the transport across a FM/SC interface the continuity of the spin polarized current and the electro-chemical potential are two boundary conditions that have to be met, yielding as current spin polarization α [50]:

$$\alpha = \frac{\beta}{1 + \frac{(1+\beta)(1-\beta)(l_{sf}^{sc}/\sigma_{sc})}{l_{sf}^{fm}/\sigma_{fm}}} \quad (1.28)$$

The spin diffusion lengths of FM and SC are highly different, with l_{sf}^{fm} typically some tens of nanometers, while l_{sf}^{sc} can be orders of magnitudes larger. For the conductivities the opposite applies. As a result, $l_{sf}^{fm}/\sigma_{fm} \ll (1+\beta)(1-\beta)(l_{sf}^{sc}/\sigma_{sc})$ resulting in a vanishing spin polarization over the FM/SC interface. As a matter of fact, the current is already depolarized by spin-scattering in the ferromagnet before even reaching the interface to the semiconductor, as depicted in Fig. 1.8(c). In comparison, in the case for all-metallic systems, i.e. for similar conductivities, the current's spin polarization is largely maintained over the interface.

In order to establish a considerably high spin polarization in the SC, the spin accumulation at the interface of the SC needs to be higher than the spin accumulation at the FM interface. Therefore, a discontinuity of the electro-chemical potential needs to be introduced, in the form of a spin-dependent interface resistance such as a tunneling or a Schottky barrier. Such interface resistance introduces a spin-dependent drop of the electro-chemical potentials for the spin-up and spin-down channel at the interface, according to [51, 48]:

$$\mu_{\uparrow,\downarrow}(z=0+) - \mu_{\uparrow,\downarrow}(z=0-) = r_{\uparrow,\downarrow} j_{\uparrow,\downarrow}(z=0) \quad (1.29)$$

An interface resistance could therefore enhance the spin accumulation on the SC side and restore the current polarization in the SC.

For a FM/SC transition including an interface resistance $r_b^* = r_{sc} \gg r_{fm}$, the polarization of the current rewrites [48, 51]:

$$\alpha = \frac{\beta r_{fm} + \gamma r_b^*}{r_{fm} + r_{sc} + r_b^*} \quad (1.30)$$

where γ is the spin asymmetry coefficient.

In this case, the polarization of the current can be sustained over the interface, decreasing away from the interface as $\exp(-z/l_{sd}^{sc})$. It should be pointed out, that this equation holds for efficient spin-polarized current injection as well as detection, for low current in the flat-band case. As expected, the current polarization over the interface is directly proportional to the FM spin polarization β . The interface resistance r_b^* and the spin asymmetry coefficient γ offer another possibility to increase the spin injection efficiency by proper design of the barrier. Indeed, both Schottky and tunneling barriers are possible candidates for interface resistances. The FM/SC/FM structure is of especially high interest, resembling to the basic layout of a spinFET.

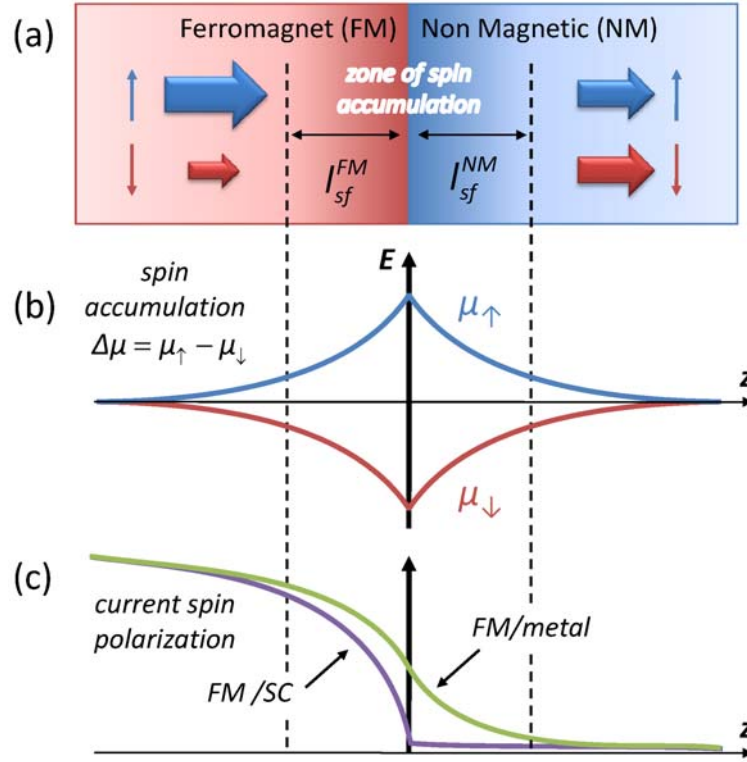


Figure 1.8: (a) Simplified picture of the current contributions from spin-up and spin-down carriers away from the interface region. (b) Splitting of the chemical potentials μ_{\uparrow} and μ_{\downarrow} at the interface. The out of equilibrium spin-split at the zone of accumulation triggers the spin depolarization from left to right. (c) The current spin polarization for spin injection from a ferromagnet into a metal, where spin-flips are equal on both sides, compared to the ferromagnet-semiconductor case, where spin-flips are predominant in the ferromagnet (adapted from [51])

For the injection and detection, symmetric ferromagnetic tunneling diodes are considered. For this reason, finding the optimum contact resistance, r_b^* , is crucial in order to have a high spin-polarization of the injection current, securing a maximum MR effect.

The observable MR effect in a FM/SC/FM structure is derived from calculations of CPP²-GMR structures, developed by VALET and FERT [52], for structures with contact width W being equal to the semiconductor channel depth, as shown in Fig. 1.9. The results of these calculations hold, as in the case of a single FM/SC interface, for flatband condition and low current density.

The calculations by FERT and JAFFRÈS [48, 51] are summarized in Fig. 1.9, where the expected MR effect as a function of the ratio r_b^*/r_{sc} and for different semiconductor channel lengths t_{sc} are depicted.³

The highest MR ratio is obtained in a relatively small symmetric window around

²CPP: current perpendicular to plane

³For the calculation of the expectable MR effect Eq. (23) and (24) in [48] are used.

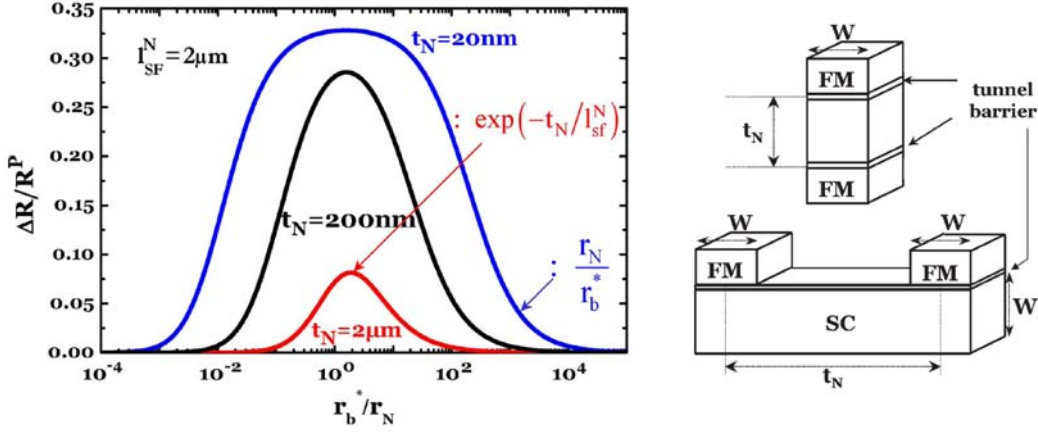


Figure 1.9: (a) Magneto resistance effect of an FM/I/SC/I/FM structure as a function of r_b^*/r_{sc} for different t_{sc}/l_{sf}^{sc} ratios. The calculation elaborated experimental values for Co, with $r_{fm} = \rho_{fm}l_{sf}^{fm} = 4.5 \times 10^{-15}\Omega m^2$, $\beta = 0.47$ and $l_{sf}^{fm} = 60nm$. The spin asymmetry $\gamma = 0.5$ for GaAs with, $N_D = 10^{16}cm^{-3}$, $r_{sc} = \rho_{sc}l_{sf}^{sc} = 4.5 \times 10^{-9}\Omega m^2$ and $l_{sf}^{sc} = 2\mu m$. (b) Magneto resistance effect of an FM/I/SC/I/FM structure as a function of the channel width ratio W/ω with the same values as above and $r_b^* = 5 \times 10^{-7}\Omega m^2$ (adapted from [51])

$r_b^* = r_{sc}$, expressed by [48, 51]:

$$\rho_{sc}t_{sc} \ll r_b^* \ll \rho_{sc} \frac{[l_{sf}^{sc}]^2}{t_{sc}} \quad (1.31)$$

where ρ_{fm} and ρ_{sc} are the resistivity of FM and SC multiplied by the respective spin diffusion lengths, l_{sf}^{fm} and l_{sf}^{sc} . The lower boundary in Eq. 1.31, $\rho_{sc}t_{sc}$ corresponds to a minimum splitting of the electrochemical potential.

The upper boundary in Eq. 1.31, $\rho_{sc}([l_{sf}^{sc}]^2)/t_{sc}$, is the condition for conservation or spin transport in the semiconductor. In order to sustain a spin accumulation, generated at a FM/SC interface, the spin injection rate has to be much higher than the spin relaxation during spin transport to the detection interface.

In real devices, including an insulator (I) as tunneling barrier at the FM/SC interface, the main problem is the large contact resistance arising from the silicon Schottky barrier of the injection/detection diodes for efficient spin injection [53, 54, 55, 56]. Therefore, the upper limit in Eq. 1.31 becomes the crucial condition for spin injection/detection.

According to the calculations in Fig. 1.9 the range of contact resistances for an observable MR effect as well as the MR amplitude is increasing for $t_{sc} \ll l_{sf}^{sc}$. The maximum value of the MR can be found by [48, 51]:

$$\left[\frac{\Delta R}{R_p} \right]^{max} = \frac{\gamma^2}{1 - \gamma^2} \quad (1.32)$$

For this reason, MR ratios a lot higher than 100% can be obtained by such structures, for a spin asymmetry coefficient γ close to 1. For amorphous tunneling barriers like

Al_2O_3 the spin asymmetry is $\gamma \sim 0.5$, corresponding to incoherent tunneling in TMR cells (Section 1.1.3). However, for coherent tunneling, γ values close to unity can be obtained, marking the importance of spin filtering tunneling barriers, e.g. crystalline $\text{MgO}(001)$, for spin injection and detection in semiconductors. Successful spin injection has been observed for different contact architectures. A brief overview concentrating on spin injection in silicon is presented in the following.

1.1.5 Injection through a Schottky barrier

The Schottky contact is one proposed architecture to overcome the conductivity mismatch issue [57, 58, 59].

For the case of highly doped semiconductor interfaces, where the current transport is determined by tunneling through the Schottky barrier, successful spin injection has been shown in GaAs by HANBICKI *et al.* [60], as well as in silicon by ANDO *et al.* [61]. On the basis of this work on spin injection in silicon, the recent work by ANDO *et al.* is briefly introduced in the following.

Fe_3Si Schottky diode on n-type Si(111) with a doping density of $N_D = 4.5 \times 10^{15} \text{cm}^{-3}$ and a Sb delta-doping layer ($N_D = 2.3 \times 10^{19} \text{cm}^{-3}$) 10 nm from the interface are used as injection/detection contacts. For such diodes, a very low current rectification is observed, which is almost independent as a function of temperature confirming that tunneling is the dominant transport mechanism. The schematic band-structure for such diodes is depicted in Fig. 1.10(a).

A four-contact, non-local measurement geometry is employed, which is a frequently used measurement setup in order to separate spurious effects from the spin signal [62, 63]⁴. For this case, the injected current is conducted as drift current from the injection diode to an ohmic side contact, while the non-equilibrium spin accumulation under the injector is causing an isotropically propagating spin diffusion. This spin diffusion current can be detected by a voltage building up between the detection diode and another side contact, corresponding to the spin polarization under the detection diode. Non-local voltage ($\Delta V/I$) measurements are shown in Fig. 1.10(b) as a function of the in-plane field applied along the diodes' long axis. It is shown that for Schottky tunneling diodes efficient spin transport can be achieved with a non-local signal change as high as $\Delta V/I \sim 400 \text{m}\Omega$ at 20 K, demonstrating the feasibility of Schottky tunneling diodes for spin injection in semiconductors.

However, there are certain drawbacks delimiting the device employment of Schottky barriers. During device fabrication temperatures high enough to promote diffusion of magnetic material into the SC apply. Such magnetic impurities act as effective spin scattering centers. On the other hand for low doped semiconductors, conduction by thermionic emission takes place well above the Fermi energy, excluding any spin-dependence of the inserted Schottky barrier .

⁴The non-local geometry has already been introduced for the Johnson-Silsbee experiment in Section 1.1.3

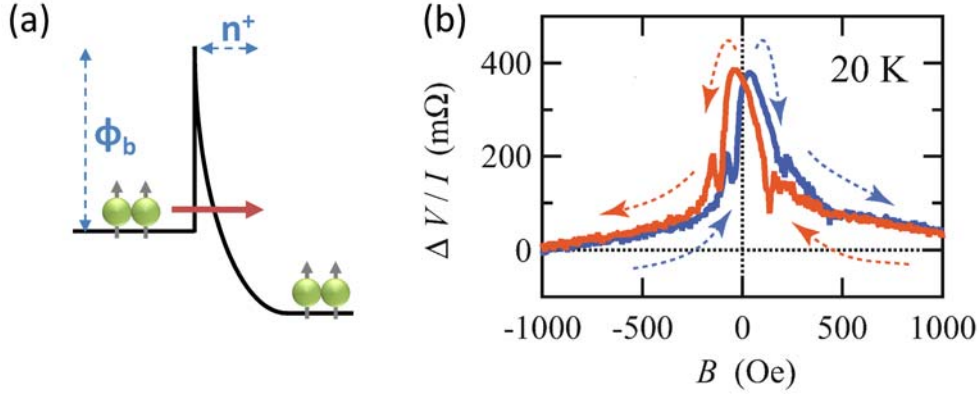


Figure 1.10: (a) Schematic band diagram for a Schottky diode (b) Non-local $\Delta V/I$ as a function of the magnetic in plane field (adapted from [61])

1.1.6 Injection through a tunneling barrier

This is the probably most promising contact architecture and therefore extensively investigated [48, 64, 51, 65, 43, 47, 66]. In contrast to Schottky diodes, the spin-dependent resistance of tunneling barriers can be tuned over a wide range by tuning the barrier parameters, i.e. its thickness and height. Another important parameter is the spin-asymmetry coefficient γ , which is related to the combination of FM and insulator as well as the semiconductor. While the use of 3d-FMs with amorphous Al_2O_3 leads to γ values not exceeding 0.5, the employment of crystalline MgO could lead to γ values considerably higher than 0.5 for the proper choice of SC and FM, as suggested by large MR values in MTJs [30]. The barrier resistance is a critical parameter. For a large barrier resistance the time electrons remain in the semiconductor for a FM/I/SC/I/FM device increases, so does the spin-scattering. On the other hand for low barrier resistance the transmission is high, diminishing the injection efficiency, since the currents' depolarization in the ferromagnetic contacts is facilitated. Therefore, barriers with an intermediate barrier height are predicted to work best for spin injection/detection [67, 63].

Besides, spin injection into semiconductors, spin polarized current may be generated as well by spin-selective extraction. Indeed, for a ferromagnetic tunneling diode the spin dependent tunneling rate is higher for the majority spin channel, leaving back an excess of minority spin carriers, resulting in a minority carrier spin accumulation [68, 69, 70]. Spin extraction has been already shown to work well in metals [12, 71, 72], GaAs [73, 62] and graphene [74]. Especially the bias dependence of tunneling diodes, for injection as well as extraction is of high interest [67, 63, 76].

We now describe one of the most successful spin injection experiments from tunnel contacts to silicon by VAN'T ERVE *et al.* is discussed [75]. A Si(001) epi-layer with a phosphorus doping density close to the metal semiconductor transmission ($N_D \sim 3 \times 10^{18} \text{ cm}^{-3}$) has been used in order to avoid carrier freeze out at low temperature. Magnetic tunneling diodes consisting of Al_2O_3 (1 nm)/Fe (10 nm) have been elaborated as injection/detection contacts to silicon in a non-local measurement

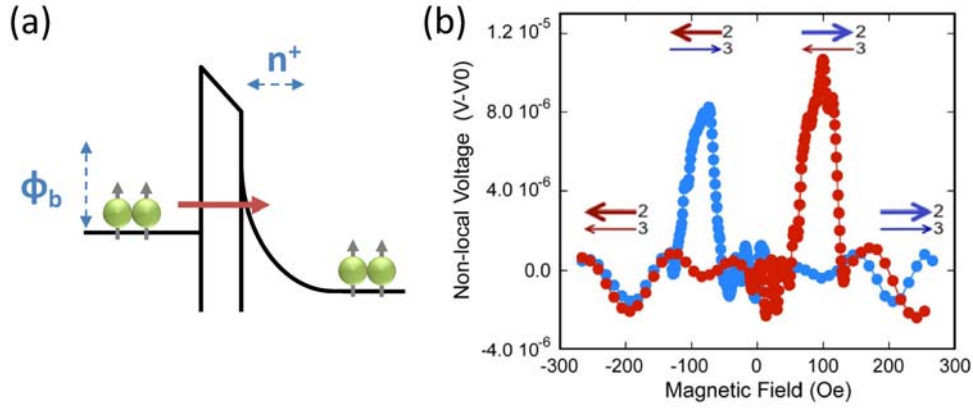


Figure 1.11: (a) Schematic band diagram for a tunneling diode (b) Non-local voltage as a function of the in-plane field for $100 \mu A$ injection current at $10 K$. (from [75])

geometry, a setup that has already been introduced in Section 1.1.3 as well as the previous section. The schematic band diagram of such ferromagnetic-insulator semiconductor diodes is depicted in Fig. 1.11(a). In Fig. 1.11(b) the non-local voltage of such structures is shown as a function of the magnetic in-plane field, measured at $10 K$ with an injection current $-100 \mu A$. The change in the non-local voltage can be directly correlated to the magnetic switching fields of the contacts, attesting successful spin injection into silicon elaborating ferromagnet-insulator-silicon tunneling diodes.

1.1.7 Ballistic injection

Another promising technique to avoid the conductance mismatch and spurious effects, is ballistic spin injection [43, 39]. This concept elaborates the spin-dependent attenuation rate of ballistic electrons for spin injection, frequently referred to as spin-valve transistor [77, 78]. The device introduced in the following, incorporates two spin-valve transistors for spin injection and detection of a spin-polarized hot-electron current in silicon [45, 79, 80, 81, 82].

The schematic band diagram is depicted in Fig. 1.1.7(a), using an Al-based solid state emitter to produce an unpolarized electron current. The hot-electrons are subjected to spin-dependent scattering in the adjacent $Co_{84}Fe_{16}$ electrode, attenuating the minority spin electrons, while the majority electrons are scattered less, holding their energy high. The transition to the float-zone (FZ) silicon layer is providing a Schottky barrier, which can only be surmounted for the majority electrons still holding high enough energy, compared to the minority electrons being filtered. Using such setup, the electrons' polarization is according to the CoFe majority carrier quantization, with a spin polarization that can get close to 100% [45]. In a second spin-valve transistor, consisting of NiFe and Cu, the current is filtered again. In this transport stage only electron spins that are aligned in parallel to the detection of the NiFe layer can traverse to the second silicon region. The carriers that have been

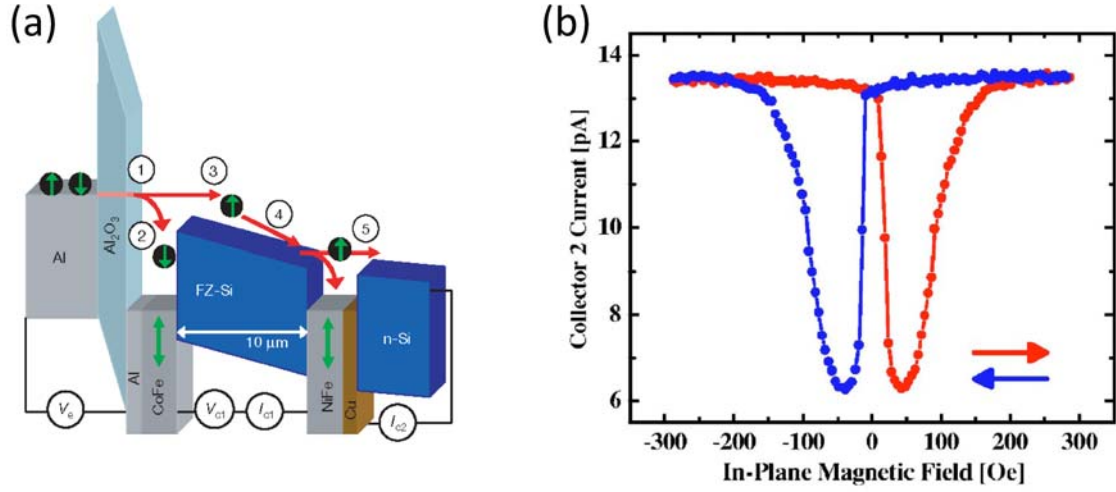


Figure 1.12: (a) Schematic band diagram of the ballistic device layout, showing the layer stack as well as the measured current contributions. (b) In-plane spin-valve effect of $\sim 115\%$, measured at 85 K for an injection bias $V_e = -1.6V$ and $V_{cl} = 0V$. (adapted from [45, 80])

thermalized in the FZ region as well as minority carriers are filtered in the detection spin-valve transistor. The collector current I_{c2} shows a magneto-current with a low current value for antiparallel alignment and a high current value for parallel alignment of the CoFe-injector and the NiFe-detector contact, as shown in (b). The calculation of the magneto-current $MC = (I_{c2}^p - I_{c2}^{ap})/I_{c2}^{ap}$ from parallel and antiparallel magnetic alignment reveals an MC-amplitude in the order of 115%.

This concept of ballistic spin injection shows the feasibility of coherent spin polarized current transport over macroscopic distances up to $350 \mu m$, indeed an astonishing result. Despite the robust nature of this effect, the power dissipation is huge, diminishing the feasibility for device application.

1.2 Characteristic Applications

The possible applications arising from semiconductor spintronics have been widely discussed [83]. The different application domains are introduced in the following.

Storage Storage capacity has been boosted to a whole new level with the introduction of GMR-based read heads in hard-disk drives. Also magnetic random access memory (MRAM) devices, incorporating MTJs, are already commercially available as non-volatile memory devices. Furthermore, spin-torque phenomena are discussed to be incorporated in second-generation MRAM devices [84, 85]. However, all these technologies are based on all-metallic magnetic effects, not involving semiconductors. The successful realization of a MRAM functionality in a semiconductor, involving spin injection and subsequent detection of spin polarized current, is a concept attracting a large amount of research right now. The central advantage of such magnetic transistors features the processing capability and especially the gain of a transistor, linked to non-volatility and the capability of reconfigurable logic circuits. Different cases of magnetic transistors, namely the unipolar spin transistor [86] as well as the bipolar spin transistor [87], have been already proposed.

Logic operations Conventional electronics still work through charge transport from one semiconductor region to another, with the MOSFET as most prominent candidate. In order to operate a transistor, a gate-tuneable barrier needs to be introduced between the source and the drain, switching the MOSFET between a conducting and a non-conducting state. The amount of switching energy is projected to be about 15 eV for a 10 nm-node transistor in 2018 [88]. The minimum entropy for the manipulation of one bit is described by the *Landauer principle* arising at a value of $(\ln 2)kT \sim 23 \text{ meV}$ [89], being 3 orders of magnitude lower than the 10nm-node transistor, leaving space for improvement.

On the contrary, an electron spin is not subjected to such high switching energies, since the spin states of different quantization direction do not intermix in a timescale lower than the spin diffusion length. In order to change the spin-states, a short magnetic field pulse or an effective magnetic field, due to spin-orbit interaction effects, needs to be applied. Even for gated devices, where spin manipulation by electric fields is applied, the switching energy is much closer to the theoretical low-limit than conventional electronic devices [90].

Furthermore, multiple operations could be subjected to carriers before their spin information is thermalized. Even the interference of different spin packets could be thought of, where two spin packets with 90° relative spin orientation are interfering, resulting in a spin-packet with 45° orientation [83]. The interference of electron spins using a semiconductor ring structure has already been shown [91].

One of the most important issues is the processing speed of spintronic devices compared to charge-based semiconducting devices. In charge-based devices the speed is

limited by the capacitance of the device and the device current. Spintronic devices are limited to precession speeds of electrons, ranging from GHz to THz.

Communications Current optical communication systems are using Faraday rotators to distinguish between incoming and outgoing light, where a change of polarization as a function of the propagation direction is achieved. Since the functionality of these device can only be changed by magnetic fields, their size is rather bulky. In ferromagnetic semiconductors magneto-optical effects could feature a comparable functionality on a lot smaller scale, with an electric-field control of the magnetic properties by spin-orbit coupling. Such devices could facilitate a seamless implementation of optical into logic circuits [83].

Quantum computation Probably the most prominent proposition of a semiconductor spintronic device is the quantum computer. Therefore, single qubits (quantum bits) in the form of single defects or quantum dots are embedded into a matrix material with individually addressed sub- μm sized contacts. The control of these individual qubits can be achieved by electric fields [92, 93, 94] or nanomagnetic fabrication [95]. One material system researchers are focussing besides GaAs is diamond. The spin-coherence times of nitrogen vacancies in diamond are exceptionally high, in the range of $350\mu\text{s}$ [96], handing over the possibility to a large number of interactions before the spin information is randomized [97]. The usage of photons to transfer single qubit states offers on the same time a mechanism to source and collect information into/from a quantum computer [98].

1.3 MRAM concept for silicon spintronics

1.3.1 The conventional MRAM design

The Magnetic Random Access Memory (MRAM) has been discussed for a couple of years to replace the commonly used DRAM⁵ cells as a memory device. Even compared to other memory technologies, like SRAM⁶, FRAM⁷ or Flash-memory, MRAM features several advantages. In 2007 the first commercially available MRAM memory by *Freescale Semiconductor* has entered the market. Today all-metallic MRAM cells up to 16Mb are available from *Everspin Technologies*⁸. A comparison of key features for different memory technologies is given in Table 1.1.

All in, the MRAM has the following advantages compared to other memory devices:

Table 1.1: Comparison of MRAM features with other memory technologies [99]

	MRAM	SRAM	DRAM	Flash	FRAM
Read time	fast	fastest	medium	fast	fast
Write time	fast	fastest	medium	low	medium
Future scalability	good	good	limited	limited	limited
Cell density	medium/high	low	high	medium	medium
Non-volatile	yes	no	no	yes	yes
Endurance	infinite	infinite	infinite	limited	limited
Cell leakage	low	low/high	high	low	low
Complexity	medium	low	medium	medium	medium

- non-volatility
- low voltage operation
- unlimited read write endurance
- fast read and write speed

The conventional MRAM cell is integrated on top of a readily processed CMOS carrier, featuring the cell selection, read and write circuitry. Therefore, this conventional MRAM cell is implemented at the back-end of line CMOS process-flow. In Fig. 1.13(a) the schematic MRAM design is depicted, where the each data bit is

⁵Dynamic Random Access Memory

⁶Static Random Access Memory

⁷Ferroelectric Random Access Memory

⁸www.everspin.com

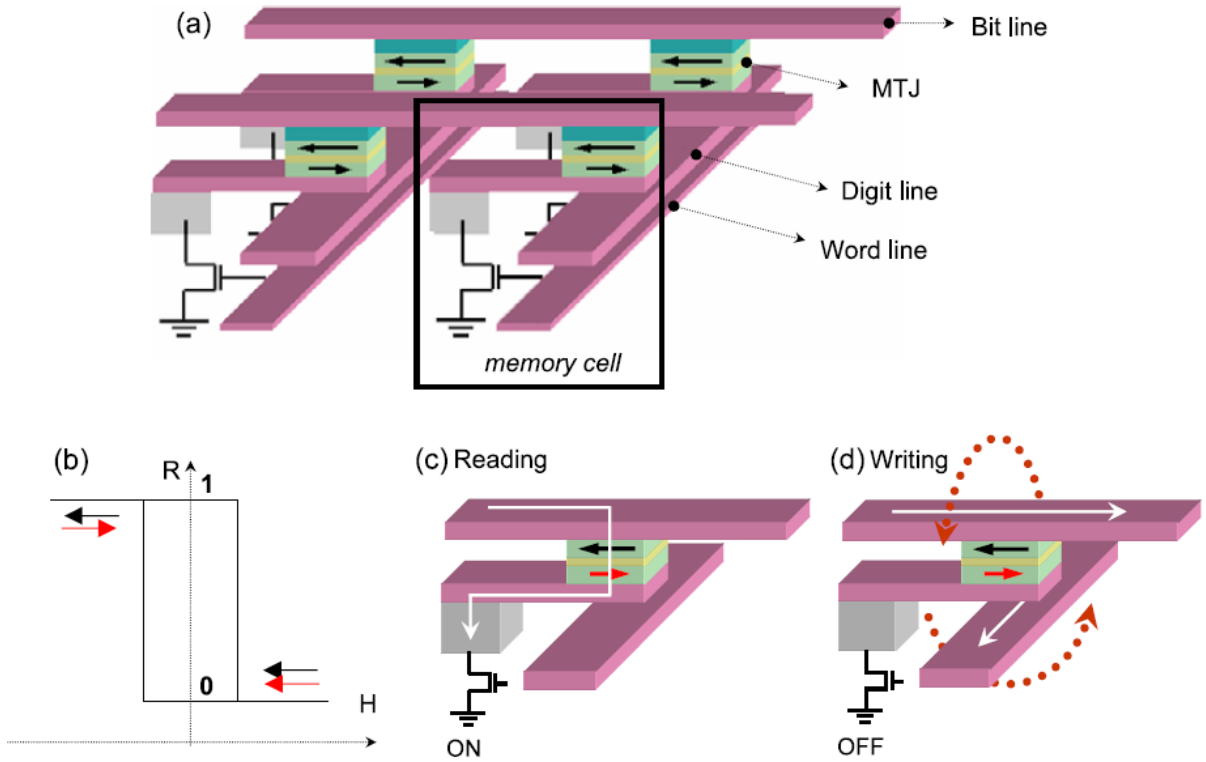


Figure 1.13: (a) Conventional MRAM architecture with MTJs are fabricated at the intersection of metallic writing lines on the top of a selection transistor. (b) Schematic magnetoresistance loop for the magnetic reversal of the magnetic free layer. (c) For reading the stored information the selection transistor and the cell resistance is compared to a normalized resistance. (d) The writing process of a new information is achieved by short current pulses through the word and bit line when the selection transistor is closed, summing up at the intersect and reconfiguring the magnetic state. (adapted from [100])

stored in a single magnetic tunnel junction (MTJ), arranged in an array. The word lines and bit lines connect different junctions.

Each MTJ is controlled by a selection transistor as shown in a schematic in Fig. 1.13(a) [101]. To read out the resistance state of a MTJ the read-out transistor is switched on, detecting the resistance state of the MTJ by comparison with a reference resistance intermediate to the high and low value of the MTJs. This already indicates the main difficulty of the MRAM implementation. For secure operation the MR effects and the resistance of the junctions have to have a low dispersion, a difficult task since the device resistance is exponentially dependent from the tunneling barrier thickness. On the other hand high MR-effects are beneficially for a reproducible read-out. For storing a bit in a MTJs, the read-out transistor is turned off and a current pulses is applied at the same time in the word as well as the bit line. The residual magnetic fields around the current lines are small enough not interacting with adjacent cells, however at the crosspoint the field sum up to switch the soft layer of the addressed MTJ. Another prerequisite of the MRAM is the well controlled size for reliable switching fields, which are highly dependent of the ele-

ments' size and aspect ratio.

In reality, however, the MTJ is not just a trilayer but a complex stack incorporating an antiferromagnet for magnetic rigidity of the hard layer and a synthetic antiferromagnet in order to compensate parasitic magnetostatic coupling effects between the layers. Furthermore, seed layers need to be well engineered in order to enhance the growth of the antiferromagnet as well as promoting a low roughness, inevitable for a high performance. The resultant device structure is a complex multilayer stack. Therefore, a simplified alternative would be highly appreciable.

1.3.2 Hybrid MRAM design using spin-polarized current in Si

One alternative to the all-metallic MRAM design is the front end implementation of a MRAM cell, elaborating spin-polarized current in silicon, which is the device of focus in this work. Such device utilizes ferromagnetic tunneling diodes on silicon for spin injection and detection, as shown in Fig.1.14. Each diode consists of tunneling barrier, ferromagnet and capping layer, embedded in a SiO_2 dielectric layer. Such MRAM concept could be designated as a "front-end-of-line MRAM design" [102]. The basic principle of this device, similar to the Datta-Das transistor, is a change in resistance for parallel and antiparallel magnetic alignment of the injection/detection contact.

This design features certain advantages, compared to the conventional MRAM design:

- The implementation of the magnetic memory parts at the front-end-of-line is simplifying the production, leading to reduced cost.
- The injection and detection diode are separated by couple of hundred nanometers, keeping magnetostatic interactions small

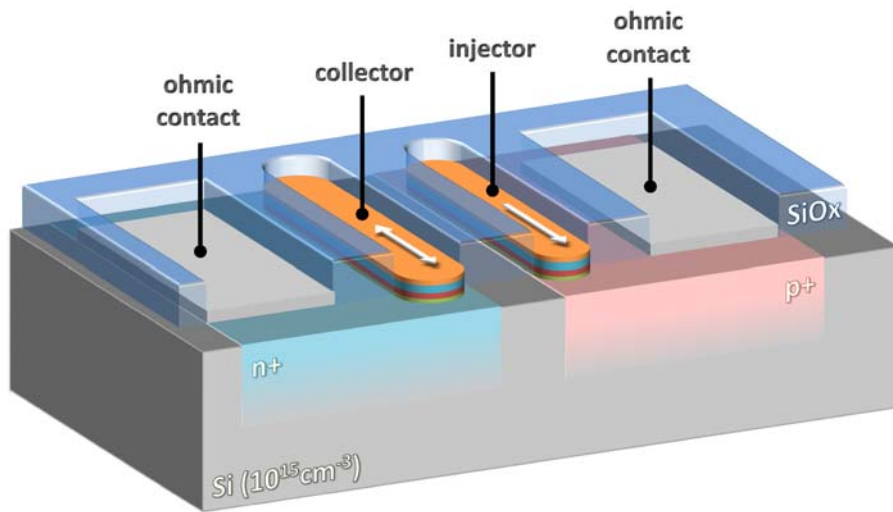


Figure 1.14: Layout of a hybrid MRAM design using spin-polarized current in Si

- The diode stack for injection and detection can be equal, since magnetic switching fields can be tailored by their sizes and shape. Due to reduced roughness and easier processing the writing margin should be decreased.

REFERENCES OF CHAPTER 1

- [1] Fasching, G. *Werkstoffe für die Elektrotechnik: Mikrophysik, Struktur, Eigenschaften*. Springer-Wien, 4. auflage edition, (2004).
- [2] Gross, R. *Spinelektronik*. Vorlesungsskript Walther-Meissner-Institut, (2004).
- [3] Sakuraba, Y., Hattori, M., Oogane, M., Ando, Y., Kato, H., Sakuma, A., Miyazaki, T., and Kubota, H. *Appl. Phys. Lett.* **88**, 192508 (2006).
- [4] Zutic, I., Fabian, J., and Sarma, S. D. *Review of Modern Physics* **76**, 323–410 (2004).
- [5] Fabian, J., Matos-Abiague, A., Ertler, C., Stano, P., and Zutic, I. *acta physica slovacica* **57**, 565 – 907 (2007).
- [6] Dyakonov, M. and Perel, V. (1971).
- [7] Slichter, C. *Principles of Magnetic Resonance*. Springer-Berlin, 3rd edition edition, (1989).
- [8] Elliott, R. J. *Physical Review* **96**(2), 266 (1954).
- [9] Simon, F., Dora, D., Muranyi, F., Garaj, S., Forro, L., Budko, S., Petrovic, C., and Canfield, P. *Phys. Rev. Lett.* , 177003 (2008).
- [10] Bir, G., Aronov, A., and Pikus, G. *Sov. Phys. JETP* **42**, 705 – 712 (1976).
- [11] D'yakonov, M. and Perel', V. *Sov. Phys. JETP* **38**, 177 – 183 (1973).
- [12] Johnson, M. and Silsbee, R. H. *Physical Review Letters* **55**(17), 1790 (1985).
- [13] Johnson, M. and Silsbee, R. *Phys. Rev. B* **37**, 5326 – 5335 (1988).
- [14] Johnson, M. *Journal of Superconductivity: Incorporating Novel Magnetism* **14**(2), 273 (2001).
- [15] Johnson, M. *Semiconductor Science and Technology* **17**, 298–309 (2002).

-
- [16] Baibich, M. N., Broto, J. M., Fert, A., Dau, F. N. V., Petroff, F., Eitenne, P., Creuzet, G., Friederich, A., and Chazelas, J. *Physical Review Letters* **61**(21), 2472–2475 (1988).
 - [17] Binasch, G., Grünberg, P., Saurenbach, F., and Zinn, W. *Physical Review B* **39**(7), 4829–4831 (1989).
 - [18] Mott, F. *Proc. R. Soc. London, Ser. A* **163**, 699 (1936).
 - [19] Fert, A. *Rev. Mod. Phys.* **80**, 1517 (2008).
 - [20] Grünberg, P., Schreiber, R., Pang, Y., Brodsky, M., and Sowers, H. *Phys. Rev. Lett.* **57**, 2442 (1986).
 - [21] Parkin, S., More, N., and Roche, K. *Phys. Rev. Lett.* **64**, 2304 (1990).
 - [22] Parkin, S. S. P., Li, Z. G., and Smith, D. J. *Applied Physics Letters* **58**(23), 2710–2712 (1991).
 - [23] Parkin, S. *Phys. Rev. Lett.* **67**, 3598 (1991).
 - [24] Dieny, B., Speriosu, V., Parkin, S., and Guerny, B. *Phys. Rev. B* **43**, 1297 (1991).
 - [25] Heim, D., Fontana, R., Tsang, C., and Speriosu, V. *IEEE Transactions on Magnetism* **30**, 316 (1994).
 - [26] Jullière, M. *Physics Letters* **54A**(3), 225 (1975).
 - [27] Miyazaki, T. and Tezuka, N. *Journal of Magnetism and Magnetic Materials* **139**(231-234) (1995).
 - [28] Moodera, J., Kinder, L. R., Wong, T. M., and Meservey, R. *Physical Review Letters* **74**(16), 3273 (1995).
 - [29] Wang, D., C, N., Daughton, J., Qian, Z., and Fink, J. *IEEE Transactions on Magnetism* **40**, 2269 (2004).
 - [30] Yuasa, S. and Djayaprawira, D. D. *Journal of Physics D: Applied Physics* **40**, 337–354 (2007).
 - [31] Bowen, M., Bibes, M., Barthelmy, A., Contour, J.-P., Anane, A., Lemaitre, Y., and Fert, A. *Appl. Phys. Lett.* **82**, 233 (2003).
 - [32] Jiang, L., Naganuma, H., Oogane, M., and Ando, Y. *Appl. Phys. Express* **2**, 083002 (2009).
 - [33] Butler, W. H., Zhang, X.-G., Schulthess, T. C., and MacLaren, J. M. *Phys. Rev. B* **63**, 054416 (2001).
 - [34] Datta, S. and Das, B. *Applied Physics Letters* **56**(7), 665 (1990).

-
- [35] Lee, W. Y., Gardelis, S., Choi, B.-C., Xu, Y. B., Smith, C. G., Barnes, C. H. W., Ritchie, D. A., Linfield, E. H., and Bland, J. A. C. *Journal of Applied Physics* **85**(9), 6682 (1999).
 - [36] Hammar, P. R., Bennett, B. R., Yang, M. J., and Johnson, M. *Physical Review Letters* **83**(1), 203 (1999).
 - [37] Gardelis, S., Smith, C. G., Barnes, C. H. W., Linifield, E. H., and Ritchie, D. A. *Physical Review B* **60**(11), 7764 (1999).
 - [38] Hammar, P. R., Bennett, B. R., Yang, M. J., and Johnson, M. *Phys. Rev. Lett.* **84**, 5024 (2000).
 - [39] Monzon, F., Tang, H., and Roukes, M. *Physical Review Letters* **84**(21), 5022 (2000).
 - [40] van Wees, B. *Phys. Rev. Lett.* **84**, 5023 (2000).
 - [41] Monzon, F. G. and Roukes, M. L. *Journal of Magnetism and Magnetic Materials* **198-199**(632-635) (1999).
 - [42] Filip, A. T., Hoving, B. H., Jedema, F. J., van Wees and B. Dutta, B. J., and Borghs, S. *Physical Review B* **62**(15), 9996 (2000).
 - [43] Schmidt, G., Ferrand, D., Molenkamp, L. W., Filip, A. T., and van Wees, B. J. *Physical Review B* **62**(8), 4790 (2000).
 - [44] Kikkawa, J. M. and Awschalom, D. D. *Physical Review Letters* **80**(19), 4313–4316 May (1998).
 - [45] Appelbaum, I., Huang, B., and Monsma, D. J. *Nature* **447**, 295 (2007).
 - [46] Fert, A., Duvail, J. L., and Valet, T. *Physical Review B* **52**(9), 6513 (1995).
 - [47] Schmidt, G. and Molenkamp, L. W. *Semiconductor Science and Technology* **17**, 310–321 (2002).
 - [48] Fert, A. and Jaffrès, H. *Physical Review B* **64**(18), 4420 (2001).
 - [49] Fert, A. and Lee, S. *Phys. Rev. B* **53**(10), 6554 – 6565 (1996).
 - [50] van Son, P., van Kempen, H., and Wyder, P. *Physical Review Letters* **58**(21), 2271 (1987).
 - [51] Fert, A. , George, J.-M., Jaffrès, H., and Mattana, R. *IEEE Transactions on Electron Devices* **54**, 921 (2007).
 - [52] Valet, T. and Fert, A. *Phys. Rev. B* **48**, 7099 (1993).
 - [53] Min, B. C., Lodder, J. C., Jansen, R., and Motohashi, K. *Journal of Applied Physics* **99**(08), 701 (2006).

-
- [54] Min, B. C., Motohashi, K., Lodder, C., and Jansen, R. *Nature Materials* **5**, 817 (2006).
 - [55] Uhrmann, T., Dimopoulos, T., Brückl, H., Lazarov, V. K., Kohn, A., Paschen, U., Bär, L., and Rühlig, M. *Journal of Applied Physics* (2007).
 - [56] Uhrmann, T., Dimopoulos, T., Kovacs, A., Kohn, A., Weyers, S., Paschen, U., Smoliner, J., and Brückl, H. *Journal of Physics D: Applied Physics* **42**, 145114 (2009).
 - [57] Zutic, I. . and Fabian, J. *Nature* **447**, 268 (2007).
 - [58] Jansen, R. *Nature Physics* **3**(8), 521 (2007).
 - [59] Sugahara, S. and Tanaka, M. *Appl. Phys. Lett.* **84**, 2307 (2004).
 - [60] Hanbicki, A., Jonker, B., Itskos, G., Kioseoglou, G., and Petrou, A. *Appl. Phys. Lett.* **80**, 1240 (2002).
 - [61] Ando, Y., Hamaya, K., Kasahara, K., Kishi, Y., Ueda, K., Sawano, K., Sadho, T., and Miyao, M. *Appl. Phys. Lett.* **94**, 182105 (2009).
 - [62] Lou, X., Adelmann, C., Crooker, S. A., Garlid, E. S., Zhang, J., Reddy, K. S. M., Flexner, S. D., Palmstrom, C. J., and Crowell, P. A. *Nature Physics* **3**, 197 (2007).
 - [63] van't Erve, O. M. J., Hanbicki, A. T., Holub, M., Li, C. H., Awo-Affouda, C., Thompson, P. E., and Jonker, B. T. *Applied Physics Letters* **91**(21), 2109–2111 (2007).
 - [64] Jaffres, H. and Fert, A. *Journal of Applied Physics* **91**(10), 8111 (2002).
 - [65] Rashba, E. I. *Physical Review B* **62**(24), 16267 (2000).
 - [66] Schmidt, G. *Journal of Physics D: Applied Physics* **38**, 107 (2005).
 - [67] Jonker, B. T., Kioseoglou, G., Hanbicki, A. T., Li, C. H., and Thompson, P. E. *Nature Physics* **3**, 542 (2007).
 - [68] Zutic, I., Fabian, J., and Sarma, S. D. *Phys. Rev. Lett.* **88**(6), 066603 (2002).
 - [69] Bratkovsky, A. and Osipov, V. *Appl. Phys. Lett.* **96**(8), 4525 (2004).
 - [70] Osipov, V., Petukhov, A., and Smelyansliy, V. *Appl. Phys. Lett.* **87**(20), 202112 (2005).
 - [71] Jedema, F., Filip, A., and van Wees, B. *Nature* **410**, 345 – 348 (2001).
 - [72] Valenzuela, S. O., Monsma, D. J., Marcus, C. M., Narayanamurti, V., and Tinkham, M. *Physical Review Letters* **94**(19), 6601–6604 (2005).

-
- [73] Crooker, S. A., Furis, M., Lou, X., Adelmann, C., Smith, D. L., Palmstrom, C. J., and Crowell, P. A. *Science* **309**, 2191 (2005).
 - [74] Tombros, N., Jozsa, C., Popinciuc, M., Jonkman, H., and van Wees, B. *Nature* **448**(7153), 571 (2007).
 - [75] van't Erve, O., Awo-Affouda, C., Hanbicki, A., Li, C., Thompson, P., and Jonker, B. *IEEE Transactions on Electron Devices* **56**(10), 2343 (2009).
 - [76] Sasaki, T., Oikawa, T., Suzuki, T., Shiraishi, M., Suzuki, Y., and Tagami, K. *Appl. Phys. Express* **2**, 053003 (2009).
 - [77] Monsma, D., Lodder, J., Popma, T., and Dieny, B. *Phys. Rev. Lett.* **74**, 5360 – 5263 (1995).
 - [78] Monsma, D. J., Vlutters, R., and Lodder, J. C. *Science* **281**, 407 (1998).
 - [79] Huang, B. and Appelbaum, I. *Journal of Applied Physics* **100**(03), 4501 (2006).
 - [80] Huang, B., Monsma, D. J., and Appelbaum, I. *Applied Physics Letters* **91**(07), 5201 (2007).
 - [81] Huang, B., Monsma, D. J., and Appelbaum, I. *Physical Review Letters* **99**(17), 7209 (2007).
 - [82] Huang, B., Zhao, L., Monsma, D. J., and Appelbaum, I. *Applied Physics Letters* **91**(05), 2501 (2007).
 - [83] Awschalom, D. D. and Flatté, M. E. *Nature Physics* **3**, 153 (2007).
 - [84] Slonczewski, J. *Journal of Magnetism and Magnetic Materials* **159**, L1 – L7 (1996).
 - [85] Berger, L. *Phys. Rev. B* **54**, 9353 – 9358 (1996).
 - [86] Flatte, M. E. and Vignale, G. *Appl. Phys. Lett.* **78**, 1273 (2001).
 - [87] Flatte, M. E., Yu, Z. G., Johnston-Halperin, E., and Awschalom, D. D. *Applied Physics Letters* **82**(26), 4740 (2003).
 - [88] *International Technology Roadmap for Semiconductors* , [http: public.itrs.net](http://public.itrs.net).
 - [89] Landauer, R. *IBM J. Res. Dev.* **5**, 183 – 191 (1961).
 - [90] Hall, K. C. and Flatté, M. E. *Applied Physics Letters* **88**(16), 2503 (2006).
 - [91] Kato, Y., Myers, R., Gossard, A., and Awschalom, D. *Appl. Phys. Lett.* **86**, 162503 (2005).
 - [92] Loss, D. and DeVincenzo, D. P. *Phys. Rev. A* **57**, 120 – 126 (1998).

-
- [93] Kato, Y. K., Myers, R. C., Gossard, A. C., Levy, J., and Awschalom, D. D. *Science* **299**, 1201 – 1204 (2003).
 - [94] Petta, J., Johnson, A., Taylor, J., Laird, E., Yacoby, A., Lukin, M., Marcus, C. M., Hanson, M., and Gossard, A. *Science* **309**, 2180 – 2184 (2005).
 - [95] Tokura, Y., van der Wiel, W., and adn S. Tarucha, T. O. *Phys. Rev. Lett.* **96**, 047202 (2006).
 - [96] Gaebel, T., Domhan, M., Popa, I., Wittmann, C., Neumann, P., Jelezko, F., Rabeau, J., Stavrias, N., Greentree, A., Prawer, S., Meijer, J., Twamley, J., Hemmer, P., and Wrachtrup, J. *Nature Physics* **2**, 408 (2006).
 - [97] Jelezko, F., Gaebel, T., Popa, I., Gruber, A., and Wrachtrup, J. *Phys. Rev. Lett.* **92**, 047202 (2004).
 - [98] Leuenberger, M., Flatte, M., and Awschalom, D. *Phys. Rev. Lett.* **94**, 107401 (2005).
 - [99] *MRAM Factsheet*, www.freescale.com .
 - [100] I.L.Prejbeanu, Kerekes, M., Sousa, R., H.Sibuet, O.Redon, Dieny, B., and Nozieres, J. *J. Phys.:Condens. Matter* **19**, 165218 (2007).
 - [101] Durlam, M., Tehrani, S., DeHerrera, J. C. M., and Naji, P. *ISSCC Digest of Technical Papers* , 130–134 (2000).
 - [102] Safarov, V. *french patent, No. W0 2004/061856 A2* (2004).

CHAPTER 2

EXPERIMENTAL TECHNIQUES

The samples investigated in this thesis have all been deposited by magnetron sputtering. Besides the deposition a variety of techniques for thin film patterning have been applied. Furthermore, the techniques employed for structural, magnetic and electrical transport characterization are introduced.

2.1 Thin film deposition and patterning

2.1.1 Sputter deposition

In semiconductor industry different fabrication techniques are used for diode structures on silicon, e.g. evaporation, thermal oxidation, atomic layer deposition, chemical vapor deposition, molecular beam epitaxy and sputtering.

The technique applied in the framework of this thesis is sputter-deposition. The main advantage of sputtering is the vast variety of materials that can be deposited, including pure metals, metal alloys, material compounds, semiconductors and insulators. Especially the deposition of alloys with a small change in film composition from the target composition is another big advantage of this technique. Furthermore, the deposited films feature a low roughness and a high uniformity over large areas. Finally, the easy technological transfer from the laboratory to large scale fabrication is an additional advantage [1].

There are different sputtering techniques, that are classified by the plasma generation and the type of sputtering gas. However, the general principle to use a gas plasma and eject atoms from a target material by momentum transfer from the plasma ions, resulting in deposition on a sample, remains the same.

The basic principle to generate a gas plasma in a sputtering recipient is the so-called *glow discharge*, where a static high voltage is applied between the sputtering target (cathode) and the sample holder (anode). The recipient is filled with a gas, typically

an inert gas like Ar, with a pressure in the μbar regime. After applying the static high voltage, free electrons in the chamber are accelerated to the sample holder, colliding and ionizing atoms of the sputtering gas. The created Ar^+ ions are accelerated towards the target, where they knock out surface atoms from the target and create secondary electrons. The generated secondary electrons further ionize sputtering gas on their way to the anode and so on, resulting in a self-sustaining condition, a stable plasma-discharge. The low mean free path inside the recipient, compared to the sample-target distance, results in many scattering events for the sputtered surface atoms before deposition on the sample surface. Therefore sputtering is an isotropic deposition technique.

Using a gas mixture of O_2 or N_2 diluted in inert Ar atmosphere, is called *reactive sputtering* and results in the deposition of oxides and nitrides, respectively. The film stoichiometry can be engineered by changing the reactive gas composition in the recipient.

For sputtering deposition from an insulating target, the static field would result in a charging of the target, prohibiting the ejection of surface atoms by repulsion of the plasma ions. For this reason, a biased radio-frequency (RF) field is applied, discharging the target in every voltage period. Typically, a RF frequency of 13.56 MHz is used, where electrons are mobile enough to follow while ions are too inert due to their higher mass. One advantage of this technique is the lower operation pressure, since a stable plasma discharge can be achieved more easily.

The nowadays commonly used technique is *magnetron sputtering*, where a static magnetic field, the so-called magnetron field, is produced by rare-earth magnets placed behind the target. The magnetron field, parallel to the target surface, in combination with the applied electric field (DC or RF) is causing the secondary electrons to stay in closed orbits in front of the surface. In such a way the plasma efficiency in front of the target is increased, allowing the operation at reduced working pressures and voltages.

A more detailed description of the sputtering process can be found e.g. in the "Handbook of Thin Film Technology" [1, 2].

In this work a custom-built Leybold UNIVEX cluster system with two deposition chambers has been used. The system incorporates six 4" and two 3" DC magnetron sources, as well as one 4" RF magnetron source used for oxide deposition. The base pressure of the system is around 1×10^{-7} mbar. While metallic films have been DC magnetron-sputtered at a power of 20 W at 2 μbar , RF magnetron-sputtering has been used for MgO films at a power of 150 W and 5 μbar . For all the deposited films pure Ar has been used as a sputtering gas and the substrate was kept at a constant temperature of 22°C.

2.1.2 UV lithography

In order to pattern the deposited films in elements or to form electrical contacts, standard ultraviolet (UV) lithography has been used. Despite different resist types

that are used according to application and feature size, the basic patterning steps remain the same. These steps are shortly described in the following.

In a first step after deposition of the sample, the surface is cleaned from contaminants and other residuals. Therefore, an ultrasonic-clean in Aceton and Isopropanol for several minutes each has been carried out. Immediately afterwards the sample is placed on a hot-plate at 120°C for 5 min to evaporate condensed water. As a next step HMDS (Hexamethyldisiloxan) is spin-coated as a primer before the selected photo-resist. The sample is placed on a hot-plate to drive out the solvents, densification and in order to activate the resist, typically around 110 to 120°C for 60 s. Following, the sample is transferred to the mask-aligner (Suess MicroTec MJB4) where the pattern of the mask is transferred to the sample. The used resists feature a maximum absorption in the deep-UV spectra, changing the chemical properties and therefore the solubility in a wet chemical developer. Depending on the resist used, either positive or negative pattern reproduction can be achieved.

The patterned photo-resist can be used in different ways in the following, either for a so-called lift-off process or as mask for further structurization steps. For the first process, material is deposited on top of sample and resist. As the resist is dissolved the material on the resist is lifted-off, resulting in a structure. For the latter, the resist is used as protection for a following etching process, removing materials in the unprotected regions.

2.1.3 Dry etching techniques

Dry etching is a frequently used etching technique in the semiconductor industry. Basically, three different etching approaches are possible, namely pure physical, chemical and a physico-chemical. For this thesis ion beam etching (IBE) and reactive ion etching (RIE) have been used, where the first is corresponding to pure physical, while the latter can be all three. Both techniques are described briefly in the following.

Ion Beam etching

Ion beam etching (IBE) is a highly suitable technique for patterning of elements in the micro- and even nanometer scale. The used machine has been custom-built by *Roth & Rau* featuring an Electron Cyclotron Resonance (ECR) ion source and a Secondary Ion Mass Spectrometer (SIMS) module for real-time etching monitoring. The principle is closely related to sputtering deposition, featuring high etching-homogeneity of stacked films with different physical properties. The whole machine consists in principle of two domains. The ion source and a UHV recipient, where the sample is mounted and exposed to the ion current. The plasma generation in the source is accomplished by an electric field of a microwave (MW) antenna and a superposed magnetic field from permanent magnets. The source is filled with Ar at a pressure around 10^{-4} mbar. The free electrons in the source are accelerated in

circular orbits around the MW antenna ionizing the Ar. Geometrical dimensions of the source are chosen in such way to confine the plasma away from the walls. To accelerate ions out of the plasma two grids are used. The positively charged source grid is confining the plasma and furthermore controlling the plasma current, while the second grid is used to extract and accelerate the ions towards the sample. Ejected surface-atoms are analyzed by a SIMS module in a quadrupole mass spectrometer. The atoms entering the SIMS module are firstly ionized and subsequently filtered in an element specific quadrupole field. This field consisting of a constant and superposed alternating electric field is only accelerating ions with a certain mass to charge ratio to the detector, where the element counts per seconds are recorded, allowing a realtime monitoring of the etching depth into a film stack.

Reactive Ion Etching

The advantages of high uniformity, selectivity and high etching rate has evolved Reactive Ion Etching (RIE) to the most commonly used etching technique in semiconductor manufacturing. The aforementioned tunability of physical, chemical and physico-chemical etching and therefore the control of anisotropy is another benefit of this method [3].

A biased RF electric field is used to generate the plasma, as already discussed in 2.1.1. The field is applied between the recipient wall and the quartz chuck, where the sample is placed. The isolating chuck is charged due to the bias-component in the RF field. This high negative bias potential of the holder is causing an acceleration of the anions in the plasma towards the sample, causing an anisotropic physical etching. The possibility to set the etching-gas mixture inside the recipient allows the usage of reactive gases, like SF_6 , CF_4 or C_2F_6 just to name a few. These gases are cracked up into radical ions within the plasma, reacting in a selective way with the substrate, forming volatile products. The reaction products are leaving the surface either thermally, if the vapor pressure is sufficiently high, or by ion bombardment. For this reason, the right combination of reactive and inert gas has to be chosen, resulting in a suitable etching process. Furthermore, the RF power is another parameter in order to tune etching rate and profile in a wide range.

The used equipment for patterning SiO_2 is the *Plasmalab 80+* from *Oxford Instruments*, using a gas mixture of 10 sccm Ar and 20 sccm SF_6 at 50 mTorr with a power of 50 W. This process has been found to give the best pattern reproduction from a resist mask to the underlying SiO_2 dielectric layer, paired with a well reproducible etching rate.

2.2 Characterization techniques

2.2.1 Transmission Electron Microscopy

For analysis of the microstructure Transmission Electron Microscopy (TEM) has been applied. One big advantage of TEM is the analysis of a sample in real space (imaging mode) and reciprocal space (diffraction mode).

A beam of monochromatic electrons is produced in an electron filament. Different filaments are possible, e.g. a wolfram hairpin of a LaB_6 crystal for thermionic emission of electrons or a wolfram field emitter. Following to the emission, the beam is focussed and driven into a condenser aperture, blocking high angle electron contribution. The focussed electron beam is then traversing through an ultra thin specimen and more importantly interacting with the specimen. The sample under investigation is therefore thinned prior TEM characterization, which is the most time consuming part for TEM measurements. After traversing the sample, the modified electron beam is projected on a fluorescent screen or a CCD camera, resulting in a largely magnified image of the sample. Depending on the type of interaction there is a large amount of analysis techniques, for structural as well as chemical properties, applicable. In the following the different operational modes of a TEM microscope are introduced briefly [4, 5].

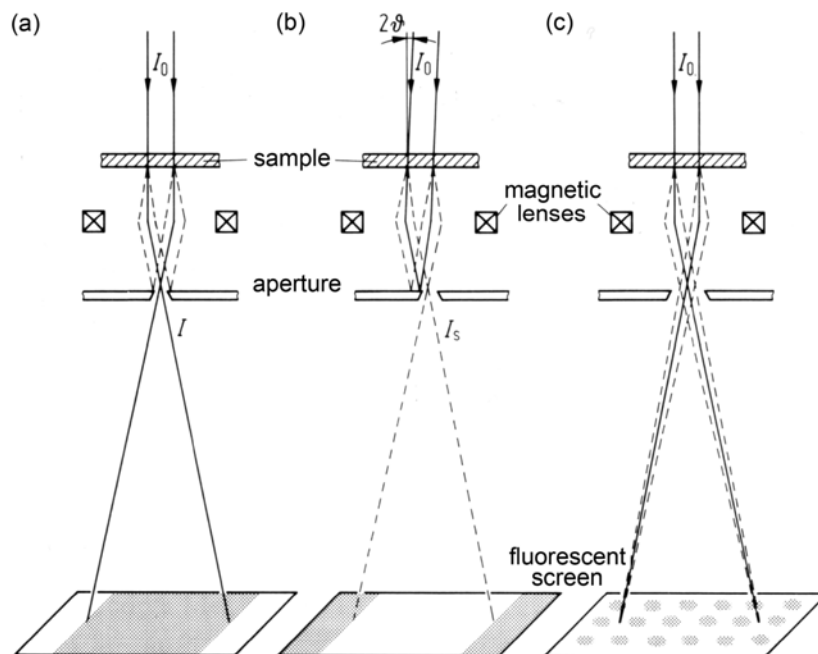


Figure 2.1: Schematic of different TEM modes: (a) Bright-field (b) Dark-Field and (c) electron diffraction mode (from [4])

Bright Field (BF) mode An aperture is placed in the back focal plane of the objective lens, allowing the direct beam to pass, however blocking the diffracted beam contributions. Dark contrast in the real space image obtained in this mode gives direct correlation of thicker areas or areas enriched with heavy elements (Fig. 2.1 (a)).

Dark Field (DF) mode The back focal plane aperture is shifted and therefore one or more diffracted beams can pass, while the direct beam is blocked. In this case, electrons have interacted stronger with the specimen than in the BF mode, comprising useful information e.g. structural disorder or elemental diffusion (Fig. 2.1 (b)).

Electron diffraction (ED) mode Electron diffraction is a collective scattering phenomenon, where electrons are nearly elastically scattered. The incoming electron wave is interacting with the atoms in the specimen and secondary electrons are created, interfering with each other [5]. The interference can be either constructive or destructive, giving an electron diffraction pattern on the screen according to the Bragg law. Since in a TEM microscope the wavelength of the electrons is known, interatomic distances and crystal orientation of the specimen can be calculated. The diffraction pattern also gives valuable information about the crystallinity of the sample (Fig. 2.1 (c)).

The main part of TEM investigations has been carried out at Oxford University (Department of Materials) by Amit Kohn, Andras Kovacs, Daniel Kirk and Vlado Lazarov. A minor part of TEM characterization has been done at the facilities of the USTEM at the TU Wien in collaboration with Jehyun Lee and Josef Fidler.

2.2.2 Atomic Force Microscopy

In 1986 the first concept of an Atomic Force Microscope (AFM) has been presented by BINNING *et al.* [6]. AFM is another follow-up technique of the scanning tunneling microscope (STM), covered under the umbrella term *scanning probe microscopy* (SPM). The SPM techniques feature a high dynamic range, highly applicable in real space surface profiling and characterization.

The principle setup of an AFM is shown in Fig. 2.2(a). A cantilever with a sharp tip is attached to a piezo-electric drive system and scanned over the surface of a sample. In a distance close to the surface the tip starts to interact with the surface, deflecting the cantilever. The deflection is measured by an optical system, where a laser beam that is reflected from the cantilever to a four-quadrant photo detector, reading out the horizontal as well as the vertical deflection. The deflection read-out is sent via a feedback loop to the controller electronics resetting the tip-to-sample

distance, corresponding to the topographic information of the sample.

The tip-to-sample interaction is due to different forces. For short tip-to-sample distance a repulsive force originating by the Pauli principle is dominant, while for longer distances the attractive van-der-Waals forces are determinant, as depicted in Fig. 2.2(b). Depending on the tip-to-sample distance there are different modes of AFM operational modes, namely *contact mode* (repulsive force regime) and *non-contact mode* (attractive force regime). The AFM system used in this work is an *Agilent 5500* operated in AC Mode for all the shown measurements [7].

In AC mode the cantilever is driven close to its resonance frequency. At the lower turning point of the swing, repulsive forces are countervailing the motion of the tip, causing a change in the resonance frequency and amplitude. The feedback regulation is resetting the z-position of the tip until the initial amplitude is accomplished again. According to this, the regulation distance is mapped, giving the topographic image.

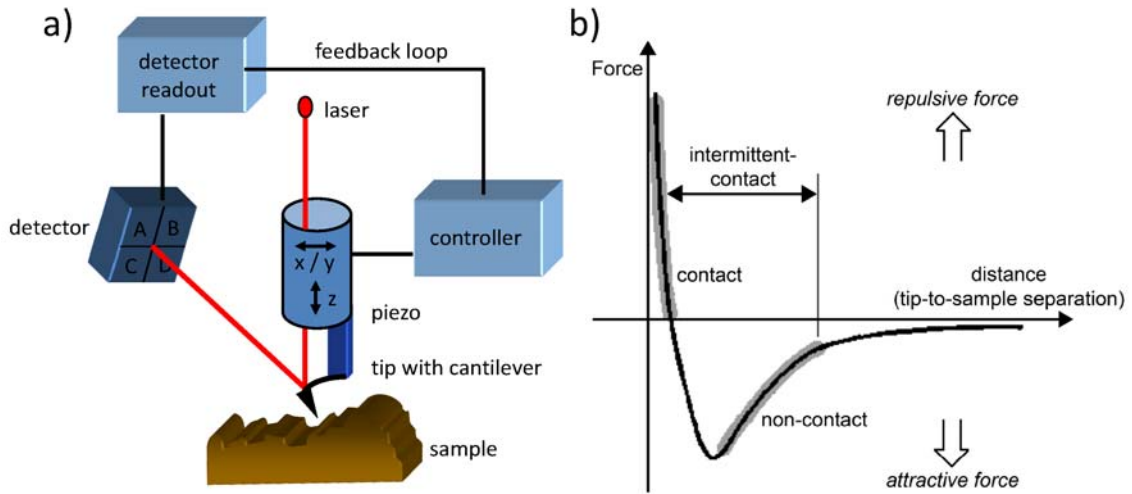


Figure 2.2: (a) Schematic setup of an atomic force microscope; (b) Force to distance curve as a function of the tip-to-sample separation [8]

2.2.3 Magnetic Force Microscopy

An additional feature provided by the atomic force microscope is the magnetic force microscopy (MFM). A tip dedicated for the AC mode is therefore coated with a magnetic layer [9, 10]. For sensitivity reasons of MFM measurements, cantilevers with a length $l \sim 225 \mu\text{m}$ with a force constant $c \sim 2.8 \text{ N/m}$ and a resonance frequency $f \sim 75 \text{ kHz}$ are used. The used tip have a magnetic coating of 35 nm of CoNi on one side of the pyramidal shaped tip. This should lead to high topographic resolution and furthermore to a well defined low magnetic moment, keeping the magnetic interaction low enough, securing that the domain structure of the investigated sample remains practically unaltered. For MFM imaging two different scans are comprised

in order to get the magnetic mapping of the sample. In a first scan the topography is recorded in AC mode in the same way as it has been described above. Subsequently, the same line is scanned again at a certain interleave height above the sample (in the range of some tens of nanometers) with the feed-back loop switched off, following the topographic features recorded in the first scan. In this way, the short range Van der Waals forces are not exerting any interaction, while long range magnetic forces are. Such magnetic forces are resulting from stray fields of domain walls as well as magnetic film boundaries.

In the presence of a force gradient, such as produced by a magnetic stray field, the phase as well as the resonance frequency are changing, where the shift of the resonance frequency is directly proportional to the force gradient. For this reason, higher contrast formation is possible for smaller interleave heights. The shift in the resonance frequency can be detected either by phase detection or amplitude detection. Phase detection measures the oscillation phase relative to the piezo driving frequency, while for amplitude detection the oscillation amplitude is measured. The obtained signal is for both cases proportional to the second derivative of the dispersion emanated from the sample [11]. For the results shown in this thesis phase detection has been employed, where the sensitivity is higher and therefore better suited for diodes with an in-plane magnetization and a relatively small magnetic net moment. In this way only a qualitative measurement is possible. However, a qualitative picture of the domain structure as well as single elements switching fields are satisfactory for the defined magnetic prerequisites defined previously.

2.2.4 Magneto Optical Kerr Effect

Two effects, the Faraday effect [12] and the Kerr effect [13, 14], are describing the interaction of polarized light and matter for transparent and reflective samples, respectively. The description of the effects is closely related and based on Maxwell's equations [15]. Also a microscopic discussion of the effect is possible using quantum theory [16]. In the following only the macroscopic picture will be present, though. For magnetized media, the effect is based on the different optical constants depending on the direction of magnetization. Treating linearly polarized light as a superposition of two circularly polarized components, the reflection and transmission is depending on the dielectric properties of the medium. For this reason the two light components face a different propagation velocity penetrating the medium, causing the rotation of the polarization plane. Another effect is based on the change of absorption of the two circular components with the direction of magnetization, causing a change in ellipticity of the resulting beam.

Depending on the direction of the magnetization with respect to the polarization of the incident light and the surface normal, three different setups for MOKE measurements are possible [17].

For the polar Kerr effect (Fig. 2.3 (a)) the magnetization is pointing parallel to the surface normal, resulting in a rotation of the polarization.

The longitudinal Kerr effect (Fig. 2.3 (b)) and (c) is observable for a sample with

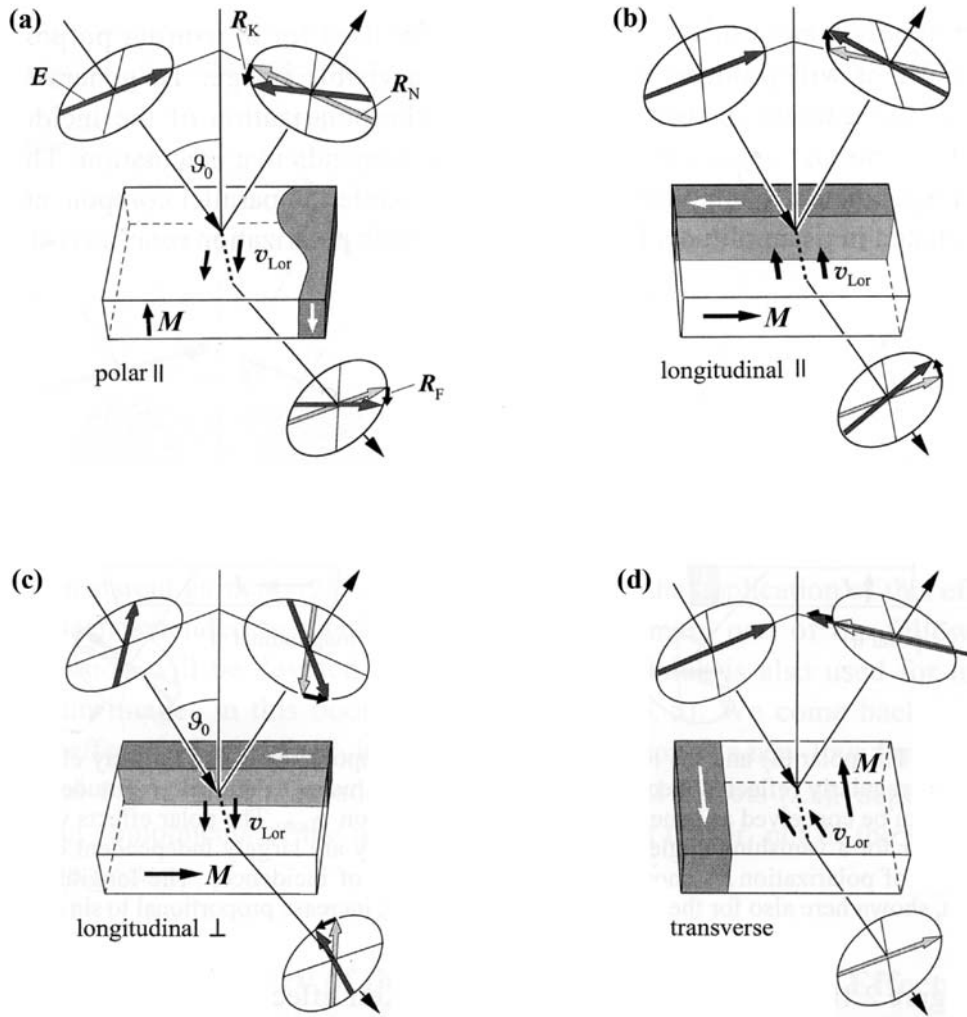


Figure 2.3: (a) Polar, (b) longitudinal (parallel polarization), (c) longitudinal (perpendicular polarization) and (d) transverse measurement geometry of the magneto-optical Kerr effect in magnetic samples. R_N is the electric amplitude of the regular reflection. The magneto-optical Kerr-amplitude, R_K , and the Faraday-amplitude, R_F , can be conceived as generated by the Lorentz motion v_{Lor} (adapted from [17])

in-plane magnetization parallel to the plane of incidence. The amplitude of the effect is proportional to $\sin(\vartheta_0)$ [17]. Furthermore, the polarization can be either parallel or perpendicular to the incident plane, showing the same effect but with different sign.

Finally, for the transverse Kerr effect (Fig. 2.3 (d)) magnetization is perpendicular to the incident plane. The reflected polarization shows a change in the amplitude, while for the transmitted component no change can be observed for this effect.

In this thesis the parallel longitudinal effect is used (Fig. 2.3 b). A setup elaborating the longitudinal Kerr effect been constructed and programmed in the framework of this thesis. A laser diode with a wavelength of 650 nm has been pulsed at a frequency of 2 kHz. The linear polarized laser beam is focussed on the sample, reflected and

interacting with the samples' magnetization and analyzed. The analyzer is set to some tens of degrees off perpendicular to the polarizer, resulting in a almost extinguishing beam. The intensity of the light passing through the analyzer, which is a function of the sample magnetization, is measured by a photo-diode with internal amplification. A lock-in amplifier has been used to trigger the detection with the driving-frequency. The noise-filtered signal is then processed and analyzed by a LabView program, resulting in a normalized hysteresis loop.

2.2.5 Electrical transport measurements

For electrical transport measurements have been carried out in a two-point measurement geometry using a top side ground contact or a back-side ground contact for the diode characterization and the MOS capacitor investigations, respectively. For current-voltage (IV) measurements a semiconductor parameter analyzer *Agilent/HP 4156C* has been used, featuring high measurement accuracy down to 1 fA and 0.2 μ V resolution [18]. For MOS capacitor testing different capacitive measurements have been carried out using a *Agilent 4284A LCR-Meter*, offering capacitive measurements between 20 Hz and 1 MHz[19]. All measurements have been carried out in the dark on a *PM5* measurement station from *Suess MicroTec* mounted on an air-table in an ESD shielded box [20]. For temperature dependent measurements an A150 heatable chuck system from ATT Systems has been elaborated [21].

REFERENCES OF CHAPTER 2

- [1] Maissel, L. *Handbook of Thin Film Technology*, chapter Applicaiton of Sputtering to the Deposition of Films, Chapter 4. McGraw Hill (1983).
- [2] Wehner, G. and Anderson, G. *Handbook of Thin Film Technology*, chapter The Nature of Physical Sputtering, Chapter 3. McGraw Hill (1983).
- [3] Hilleringmann, U. *Silizium Halbleitertechnologie: Grundlagen mikroelektronischer Integrationstechnik*. Vieweg + Teubner, 5. auflage edition, (2008).
- [4] Bergmann and Schaefer. *Lehrbuch der Experimentalphysik - Festkörper*. De Gruyter, (1992).
- [5] *Transmission Electron Microscopy*. <http://www.microscopy.ethz.ch/elmi-index.htm>.
- [6] Binning, G., Quate, C., and Gerber, G. *Physical Review Letters* **56**(930) (1986).
- [7] *Datasheet: Agilent 5500 Atomic Force Microscope*. www.agilent.com.
- [8] Howland, R. and Benatar, L. Technical report, Park Scientific Instruments, (1993 - 2000).
- [9] Rugar, D., Mamin, H., Guethner, P., Lamber, S., Stern, J., Fayden, I., and Yogi, T. *Journal of Applied Physics* **68**, 1169 (1990).
- [10] den Boef, A. *Appl. Phys. Lett.* **56** (1990).
- [11] Grütter, P., Mamin, H., and Rugar, D. *Scanning Tunneling Microscopy II, Springer Series in Surface Science* **281**, 151 (1992).
- [12] Faraday, M. *Trans. R. Soc.* **50**, 592 (1846).
- [13] Kerr, J. *Philos. Mag*, **3**, 339 (1877).
- [14] Kerr, J. *Philos. Mag*, **5**, 161 (1878).
- [15] Maxwell, J. *Elictricity and Magnetism* (1873).

- [16] Qiu, Z. and Bader, S. *Rev. Sci. Instr.* **71**, 1243 (2000).
- [17] Hubert, A. and Schäfer, R. *Magnetic Domains. The Analysis of Magnetic Microstructures*. Springer-Berlin, (1998).
- [18] *Datasheet: Agilent 4156C Precision Semiconductor Parameter Analyzer.* www.agilent.com.
- [19] *Datasheet: Agilent 4284A/4285A Precision LCR Meter Family.* www.agilent.com.
- [20] *Datasheet: Manual Probe System PM5.* www.suess.com.
- [21] *Datasheet: Hot Chuck System A150.* www.att-systems.com.

CHAPTER 3

EMBEDDED FERROMAGNETIC SILICON DIODES

In this chapter, silicon diode structures are analyzed for their suitability as injection/detection contacts in a two-terminal device geometry. After a brief introduction, the fabrication process is stretched out. In the following, the structural properties of diodes, with varying MgO tunneling barrier thickness and ferromagnetic electrode, are analyzed. Their magnetic properties are then investigated by means of MOKE and MFM measurements. The focus in this chapter is put on the electrical characterization. Therefore, an extended evaluation of Schottky and MgO-based ferromagnetic tunneling diodes is carried out, varying the silicon doping type and density, the ferromagnetic electrode material, the MgO-tunneling barrier thickness and the post-deposition annealing conditions. Based on this, the suitability of the investigated contacts for spin injection/detection is discussed.

3.1 Introduction and scope

The most important components of a hybrid MRAM or a spinFET are the ferromagnetic source and drain contacts, injecting and detecting spin polarized current into/from silicon. In Fig. 4.5 a reduced two-terminal device layout is sketched. The development of such contact structures is the main topic covered in this chapter. As it has been discussed previously, the condition for the observation of a significant MR-effect is coupled to the resistance-area product of the contacts. From the different possible architectures that can be employed, tunneling diodes - in our case elaborating MgO as a barrier - are considered to be the most promising one, as the junction resistance can be additionally tuned by modifying the barrier thickness and high spin-polarization efficiency is anticipated in combination with 3d-ferromagnetic electrodes. For comparison, Schottky contacts are also investigated along with the tunneling diodes.

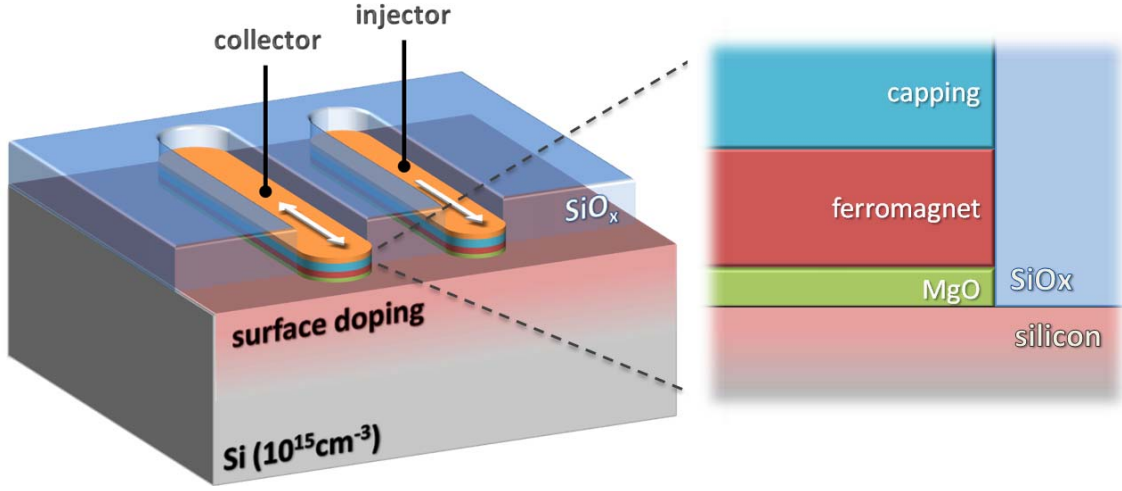


Figure 3.1: *Schematic layout of ferromagnetic source and drain contacts to silicon*

The structural characteristics of the MgO barrier and the ferromagnetic electrode play an important role for the magnetotransport properties (e.g. coherent tunneling of highly spin-polarized states). The diffusion of ferromagnetic material into silicon is also particularly important, since magnetic impurities are efficient spin scattering centers, limiting the spin coherence length. In Sec. 3.5 these structural issues of contacts to silicon with different ferromagnetic electrodes and MgO-thickness are addressed for annealing temperatures up to 400°C.

On the other hand the magnetic requirements for the successful implementation of a spinFET can be summarized as follows: (i) small switching field, (ii) high remanent magnetization and (iii) magnetic selectivity. In a final device layout the magnetic switching should be accomplished by current lines, limiting the attainable magnetic field. For this reason, the contact's switching field has to be adequately low. Furthermore, a well defined parallel and antiparallel magnetic state between injector and detector requires a high remanent magnetization for both contacts. Moreover, the switching field should be ideally the same for equally-sized diodes and tunable solely by shape anisotropy. Most importantly, between injection and detection contacts, comprising identical multilayers, significantly different magnetic switching fields must be obtained, referred here as magnetic selectivity.

The requirements concerning the magnetotransport properties of the contacts have been already laid out in the previous chapter. They are summarized into topics as follows: (i) efficient spin-polarized current injection into silicon, (ii) spin conserving transport through the silicon channel, (iii) efficient spin detection at the adjacent detection electrode. It has been shown that the range of the interface resistivity is crucial for these topics. The spin conserving transport length is already proven to be large enough in silicon, where spin relaxation is relatively low compared to other semiconductors.

In the following we investigate MgO-based tunneling diodes with respect to their suitability for silicon spintronics based on the previous requirements. Apart from the

structural and magnetic characterization, an extended evaluation of Schottky and tunneling diodes has been carried out, as a function of the MgO barrier thickness (0, 1.5 and 2.5 nm), the ferromagnetic electrode material ($\text{Co}_{70}\text{Fe}_{30}$, $\text{Co}_{40}\text{Fe}_{40}\text{B}_{20}$, $\text{Ni}_{80}\text{Fe}_{20}$), the silicon doping density and doping type (10^{15} to 10^{18}cm^{-3} for n- and p-doping), as well as the post-deposition annealing conditions (as deposited, $300^\circ\text{C}/30\text{min}$ and $400^\circ\text{C}/30\text{min}$ in Ar atmosphere).

3.2 Fabrication

Si(001)-wafers with a diameter of 8" and a phosphorus or boron bulk doping density of 10^{15}cm^{-3} have been used as substrate material. For some of the wafers the doping densities have been increased using ion implantation and a subsequent high temperature annealing step, healing dislocations in the silicon and activating the dopants. In this way, further surface doping densities of 10^{16} , 10^{17} and 10^{18}cm^{-3} have been accomplished. As a next step, 50 nm thick thermal silicon oxide has been grown, featuring a Si/SiO₂ interface with low interface state density. Standard deep-UV lithography has been used to define the sub- μm diode structures. For better feature definition, a backside anti-reflective coating (BARC) layer has been spin-coated prior to the photo-resist, shown in Fig. 3.2(a).¹ In the following step the resist structure has been transferred to the SiO₂ dielectric. For this scope, ion beam as well as reactive ion etching have been evaluated, finding RIE etching with a SF₆/Ar gas mixture to work best for accurate pattern reproduction. Furthermore, this etching process has been found to be accurate and reproducible enough, stopping couple of nanometers before the Si/SiO₂ interface without inducing any damage to it. Thereafter, the samples have been dipped in buffered HF to remove the residual oxide layer, revealing the bare silicon surface (Fig.3.2(b)). Immediately after the wet etching, the samples have been transferred into the sputtering system, for deposition of different diode structures. Three ferromagnetic electrode materials have been employed, namely $\text{Co}_{70}\text{Fe}_{30}/\text{Ni}_{80}\text{Fe}_{20}$, $\text{Co}_{40}\text{Fe}_{40}\text{B}_{20}$ and $\text{Ni}_{80}\text{Fe}_{20}$ (subscripts correspond to the target material composition in at%). These materials were deposited either directly on Si or onto the MgO tunneling barrier. A capping of Ta and Au has been deposited on top of the FM films to prevent oxidation. All metals were DC magnetron-sputtered, while MgO was deposited by RF-sputtering from a ceramic target (Fig.3.2(c)). After patterning of the diodes by lift-off processing (Fig.3.2(d)), the BARC layer has been removed in an oxygen plasma process (Fig.3.2(e)). Samples in this fabrication step have been used for magnetic and structural characterization. For electrical characterization, though, DC-sputtered Al top-side contacts have been fabricated using standard UV lithography in combination with lift-off processing (Fig.3.2(f) - (h)). The diodes' properties have been determined for the as-deposited state and after post-metallization rapid thermal annealing at 300°C , as well as 400°C for 30 min in Ar atmosphere.

¹Pre-structured wafers fabricated in the CMOS facility of Fraunhofer IMS Duisburg

For investigation of the dielectric as well as the interface properties of the MIS diodes, another type of samples has been fabricated on n- and p-doped wafers with a doping density in the order of 10^{15} cm^{-3} . In these samples the Si substrates comprised a 700 nm thick pre-metallic dielectric layer, which was patterned by deep-UV-lithography combined with dry etching techniques, to form trenches of different shapes, sizes and aspect ratios, down to the Si wafer. Shortly before deposition the wafers were dipped into low concentration HF-solution to remove any native SiO_2 film from the bottom of the trenches. $\text{MgO}/\text{Co}_{75}\text{Fe}_{25}/\text{TaN}$ and $\text{MgO}/\text{Co}_{60}\text{Fe}_{20}\text{B}_{20}/\text{TaN}$ contacts were subsequently deposited by RF and DC magnetron sputtering. The MgO film

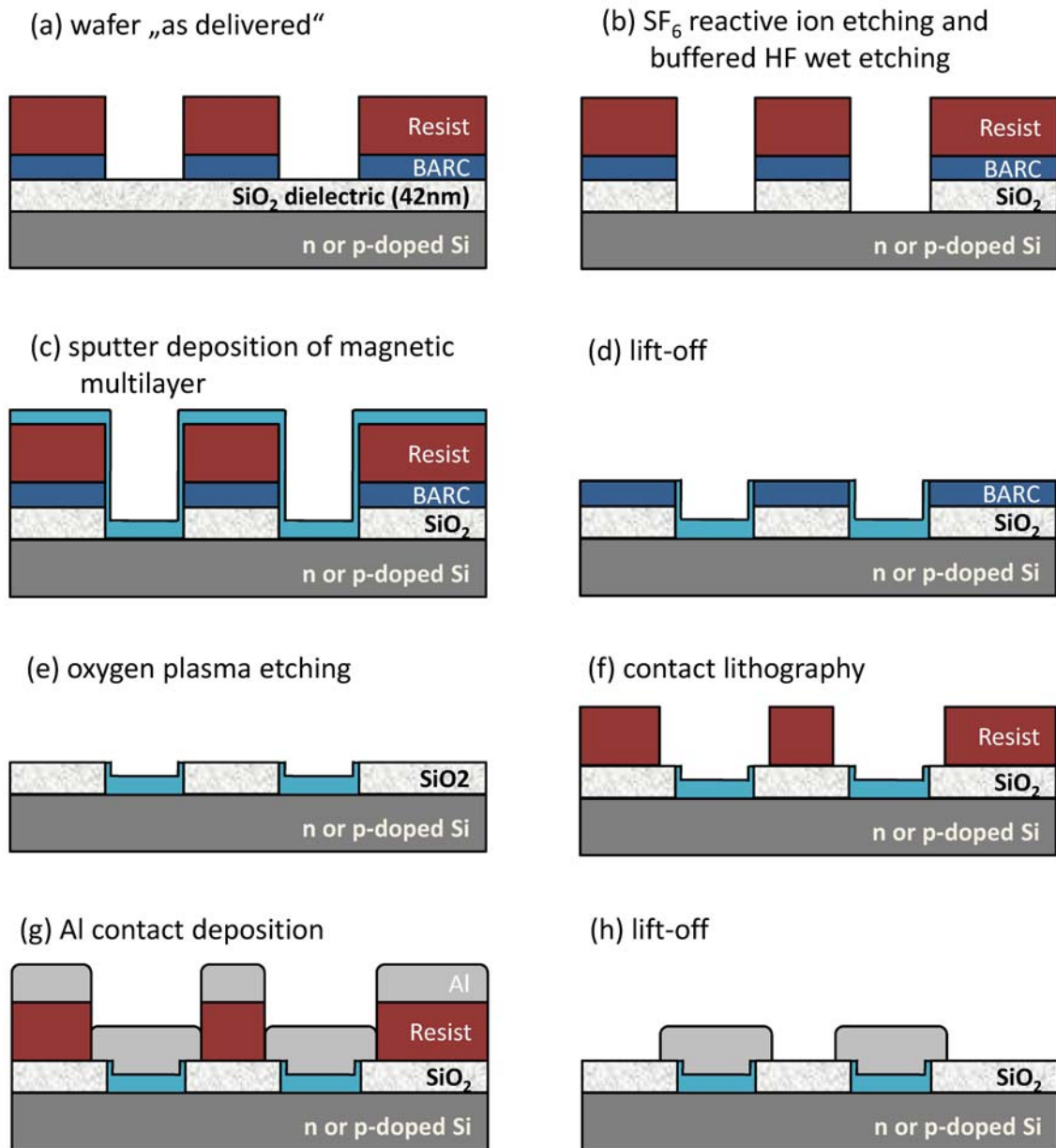


Figure 3.2: Processing steps of embedded diodes

was sputtered from a ceramic target. The deposition followed a chemical-mechanical polishing (CMP) process to remove the layers from the top of the pre-metallic dielectric. Approximately 50-100 nm of the dielectric were also removed by the CMP process. Top Al-contacts were then fabricated by UV-lithography. Finally, Al ohmic back-side contacts to the silicon wafer were also sputtered followed by rapid thermal annealing at 400°C for 15 min.

3.3 Structural characterization

In Fig. 3.3 AFM images of an array of elements with a nominal size of 450nm×3000nm is shown. Such arrays have been used for magnetic and structural investigation. The actual element size is around 50nm larger in every direction compared to the nominal one, as a result of the RIE and HF chemical over-etching. The contacts' shape is characterized by blunt, smooth ends (Fig. 3.3(b)). The length to width ratio of the circular end parts of the contacts is approximately 0.5 (Fig. 3.3(c)). In some cases edge defects are present, resulting from the etching and lift-off

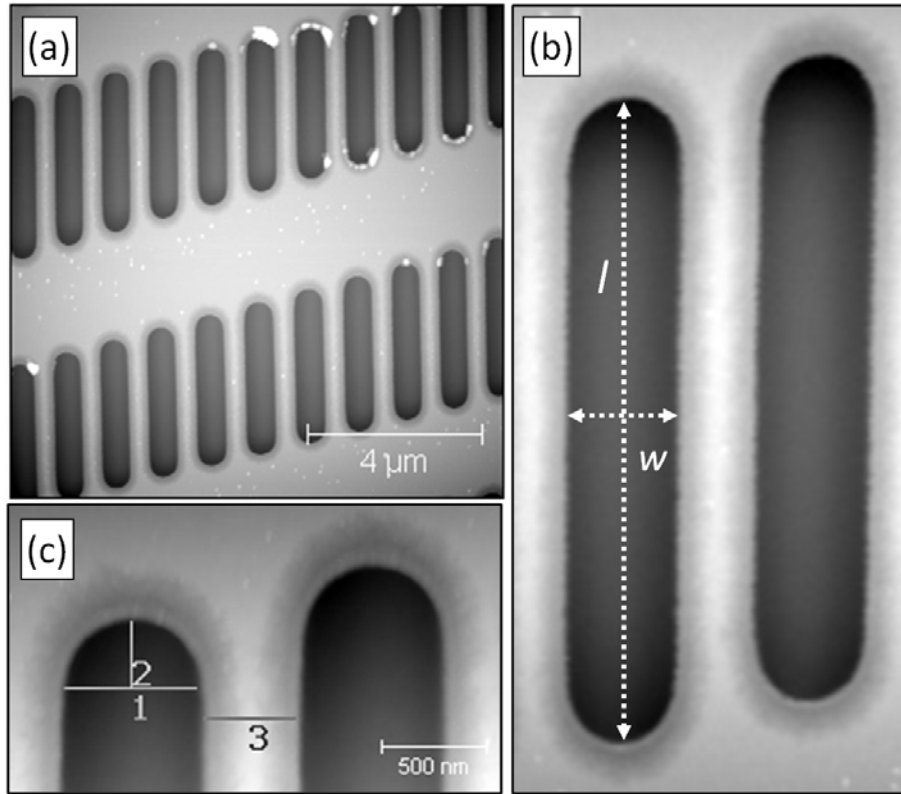


Figure 3.3: (a) AFM image of an array of contacts with a nominal size of 450nm×3000nm. (b) Zoom-in showing the shape of two adjacent contacts. (c) Zoom-in showing the shape of the ends of the contacts.

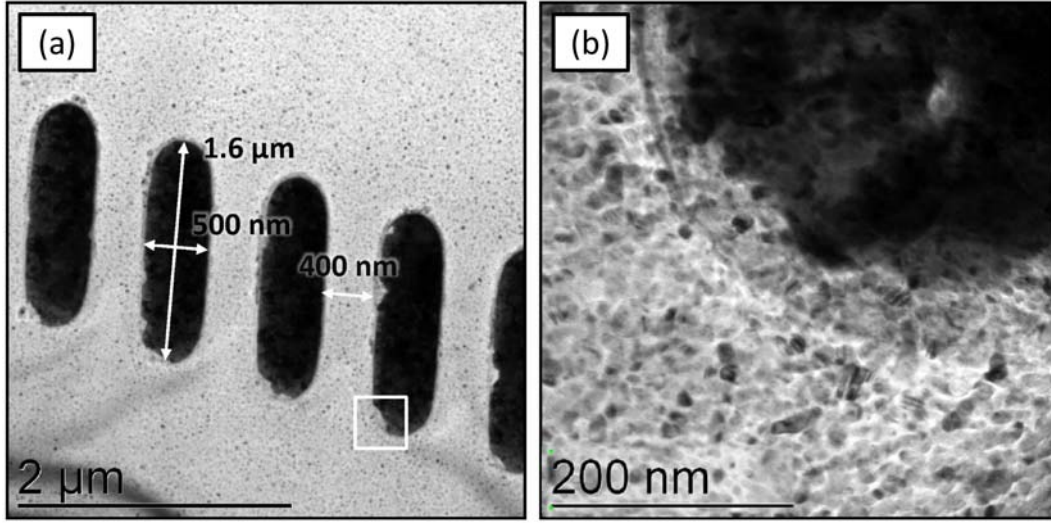


Figure 3.4: (a) Low-resolution plain-view TEM image of NiFe(10 nm)/Ta/Au Schottky diodes; (b) High-resolution image of the marked region (in collaboration with J. Lee and J. Fidler from the TU Wien)

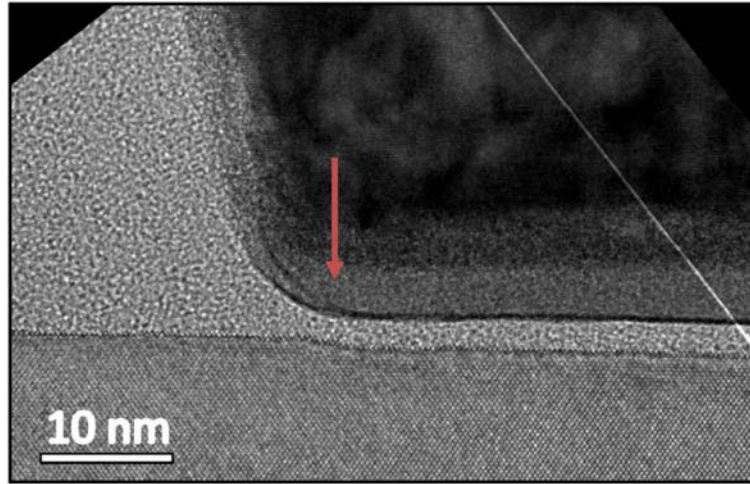


Figure 3.5: High resolution TEM image of a MgO(1.5 nm)/CoFeB(6 nm)/Ta/Au diode annealed at 300° C and subsequently at 400° C for 30 min in Ar (in collaboration with A. Kovacs and A. Kohn from Oxford University).

process. These defects are situated at the top of the trenches or the sidewalls and are therefore not expected to influence the magnetization switching characteristics.

In-plane TEM investigation has been carried out to probe the electrically active area of the contacts. Fig. 3.4 depicts plane-view TEM images of NiFe Schottky contacts in the as-deposited state. The frame in the low magnification image (Fig. 3.4(a)) denotes the region shown in the high-resolution TEM (HRTEM) image (Fig. 3.4(b)). The bright polycrystalline SiO₂ can be clearly identified in both images. SiO₂ can be as well observed inside the contact region, resulting to an electrically active area that is smaller than the topological area, by approx. 50 nm in each direction. As a

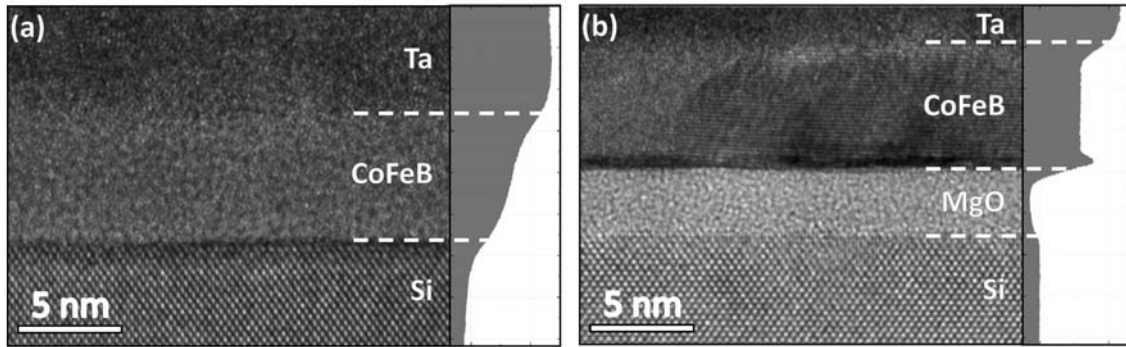


Figure 3.6: High resolution TEM images of (a) as-deposited n-Si/CoFeB(6 nm)/Ta/Au Schottky diode and (b) n-Si/MgO(2.5nm)/CoFeB(6 nm)/Ta/Au MIS diode annealed at 400°C for 30min, with the corresponding HAADF intensity line scans attached to the right side of each TEM image (in collaboration with A. Kovacs and A. Kohn from Oxford University).

result, for the electrical characterization the active area is considered the same as the nominal one.

In Fig. 3.5 a cross-view HRTEM image of the contact's edge-region for a MgO(1.5 nm)/CoFeB(6 nm)/Ta/Au diode is depicted. Also here a SiO₂ transition region is observed, marked by an arrow in Fig. 3.5. Due to this remanent SiO₂, edge currents can be neglected for all investigated samples. It should be noted that the metallic layers' thickness is a bit smaller at the edge of the contacts compared to the middle, due to shadowing effects.

The microstructure of the diodes has been also investigated by high-angle annular dark-field (HAADF) scanning TEM (STEM). All the presented results in this section have been obtained for diode structures on n-Si with a uniform doping den-

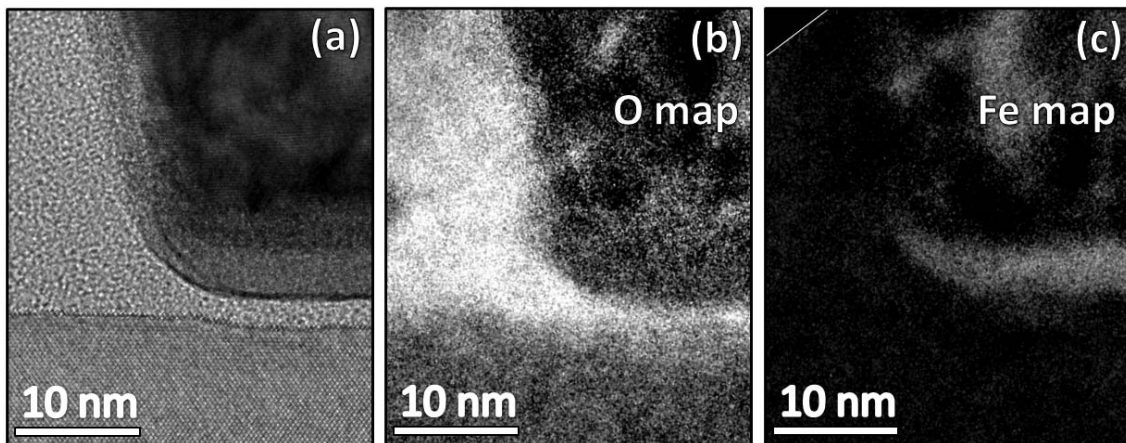


Figure 3.7: Energy filtered TEM characterization of a MgO(1.5 nm)/CoFeB(6 nm)/Ta/Au MIS diode annealed at 300°C and subsequently at 400°C for 30 min. The TEM image (a) is depicted along with EFTEM images for oxygen (b) and iron (c) (in collaboration with A. Kovacs and A. Kohn from Oxford University)

sity of 10^{15}cm^{-3} . Fig.3.6 presents HRTEM images of a CoFeB Schottky diode in the as-deposited state (Fig. 3.6(a)) and a CoFeB MIS diode with a 2.5 nm thick MgO insulating layer, annealed at 400°C (Fig. 3.6(b)). The panel to the right of each HRTEM image corresponds to HAADF STEM intensities across the various layers. The STEM intensity is related to the atomic number of the layers, thus enabling, along with the HRTEM images, to identify remnant silicon oxide and interdiffusion at the interfaces. The HRTEM image of the as-deposited Schottky diode (Fig.3.6(a)) shows an amorphous CoFeB layer on an atomically flat Si surface. Remanent silicon oxide is not observed in the HRTEM or HAADF STEM images. The MgO insulating layer in figure 3.6(b) is continuous, amorphous and exhibits low roughness at the interfaces, even after intense thermal annealing. The lack of crystallinity in such thin MgO layers is attributed to the large lattice mismatch of 22.5% [1] between MgO(001) and the Si(001) substrate. In the CoFeB film, extended bcc-textured grains with (110)-orientation appear after annealing at 400°C (Fig. 3.6(b)), marking the onset of crystallization for the amorphous ferromagnet. Lower magnification bright-field TEM images show uniform film thicknesses and low roughness of the MgO/Si and MgO/CoFeB interfaces over a field of view of several hundreds of nanometers. The HAADF STEM images of the MIS diode do not indicate significant interdiffusion at either MgO interfaces.

A more detailed investigation by means of element specific analysis has been carried out for a MgO(1.5 nm)/CoFeB(6 nm)/Ta/Au MIS diode annealed at 300°C and subsequently at 400°C for 30 min. Fig. 3.7 shows an energy filtered TEM (EFTEM) analysis of a diode's edge region. Low loss EELS verified that the sample thickness is below one inelastic mean free path of the incident electrons, enabling quantitative analysis. It should be pointed out that the oxygen map supports the increase of the barrier region at the diode edge, where SiO_2 and MgO overlap, as already mentioned before. Furthermore, the MgO barrier is an efficient diffusion barrier, continuous, with no evidence of pinholes. This is supported by the Fe-map in Fig.3.7(c), showing a confined CoFeB layer, without any sign of diffusion in silicon.

Samples featuring CoFe/NiFe and NiFe magnetic electrodes have also been characterized by TEM. Figure 3.8(a) depicts a cross section TEM image of a MgO(2.5 nm)/CoFe(2 nm)/NiFe(8 nm)/Ta/Au diode, after annealing at 300°C and subsequently at 400°C for 30 min in Ar. The Si/MgO interface is atomically flat, while the MgO layer itself has low roughness, is continuous and amorphous as before. The CoFe and NiFe layers are polycrystalline in the as-deposited state and after annealing at 400°C . However, no differentiation between NiFe and CoFe is possible in the HRTEM images. For this reason, an energy filtered TEM (EFTEM) analysis is carried out mapping the oxygen, cobalt and iron content of the layers (Fig.3.8(b-d)). The oxygen map reveals also for this sample a continuous and well defined tunneling barrier. The differentiation between CoFe and NiFe is an additional information that can be extracted from the Co and Fe-mapping shown in Fig.3.8(c) and (d), respectively. We find a Fe signal within the whole ferromagnetic electrode while Co is only present in the first part adjacent to the tunneling barrier. Furthermore, magnetic material can be detected neither within the tunneling barrier nor in silicon. Therefore, we can conclude that MgO also for thicknesses as low as 1.5 nm works

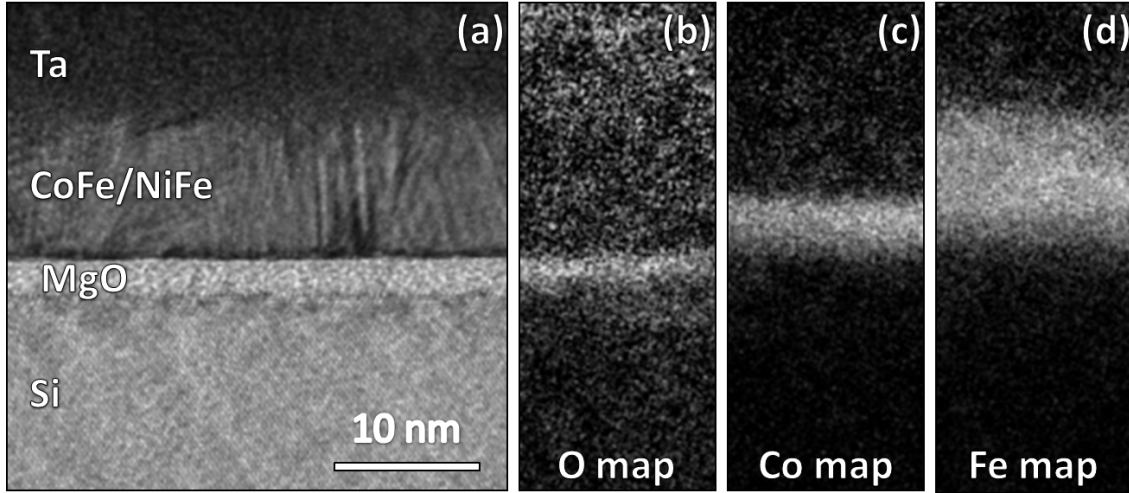


Figure 3.8: Energy filtered TEM characterization of a MgO(2.5 nm)/CoFe(2 nm)/NiFe(8 nm)/Ta/Au MIS diode annealed at 300°C and subsequently at 400°C for 30 min. The TEM image (a) is depicted along with filtered images for oxygen (b), cobalt (c) and iron (d) (in collaboration with A. Kovacs and A. Kohn from Oxford University)

satisfactory as a diffusion barrier up to 400°C.

To further demonstrate the importance of the MgO barrier in inhibiting interdiffusion, Schottky diodes have also been investigated for their thermal stability. In Fig. 3.9 we present cross-section TEM images of Schottky and MIS diodes annealed at 300°C and subsequently at 400°C for 30 min in Ar. The tunneling diodes, where no detectable intermixing takes place, are displayed on the right side of Fig. 3.9. For CoFe/NiFe and NiFe Schottky diodes pronounced diffusion of ferromagnetic material into the silicon bulk is present, while the CoFeB Schottky contacts show no sign of interdiffusion. The difference in the diffusion behavior of the Schottky diodes as a function of the FM electrode may be related to different factors. Firstly, Ni has been shown to diffuse most easily into silicon even at temperatures lower than 300°C, followed by Co and Fe [2, 3, 4], while B has a much lower diffusion coefficient [4]. This explains well the pronounced NiFe diffusion into Si. The fact that no obvious diffusion is present in the TEM image for CoFeB/Si is for sure a surprising result. However, interfacial diffusion below the resolution limit of the TEM image may be present. Electrical characteristics are a more accurate and reliable measure for diffusion than structural imaging. In fact, the electrical characterization of CoFeB Schottky diodes on n- and p-doped silicon, examined in Section 3.5 and 3.6, shows significant deterioration of the diodes' properties, concluding that the diffusion of the CoFeB is below the resolution limit of the TEM images.

Conclusion - Structural characterization

In summary, the structural characteristics of sputter-deposited ferromagnetic Schottky diodes and MgO-based tunneling diodes have been investigated. For both diode

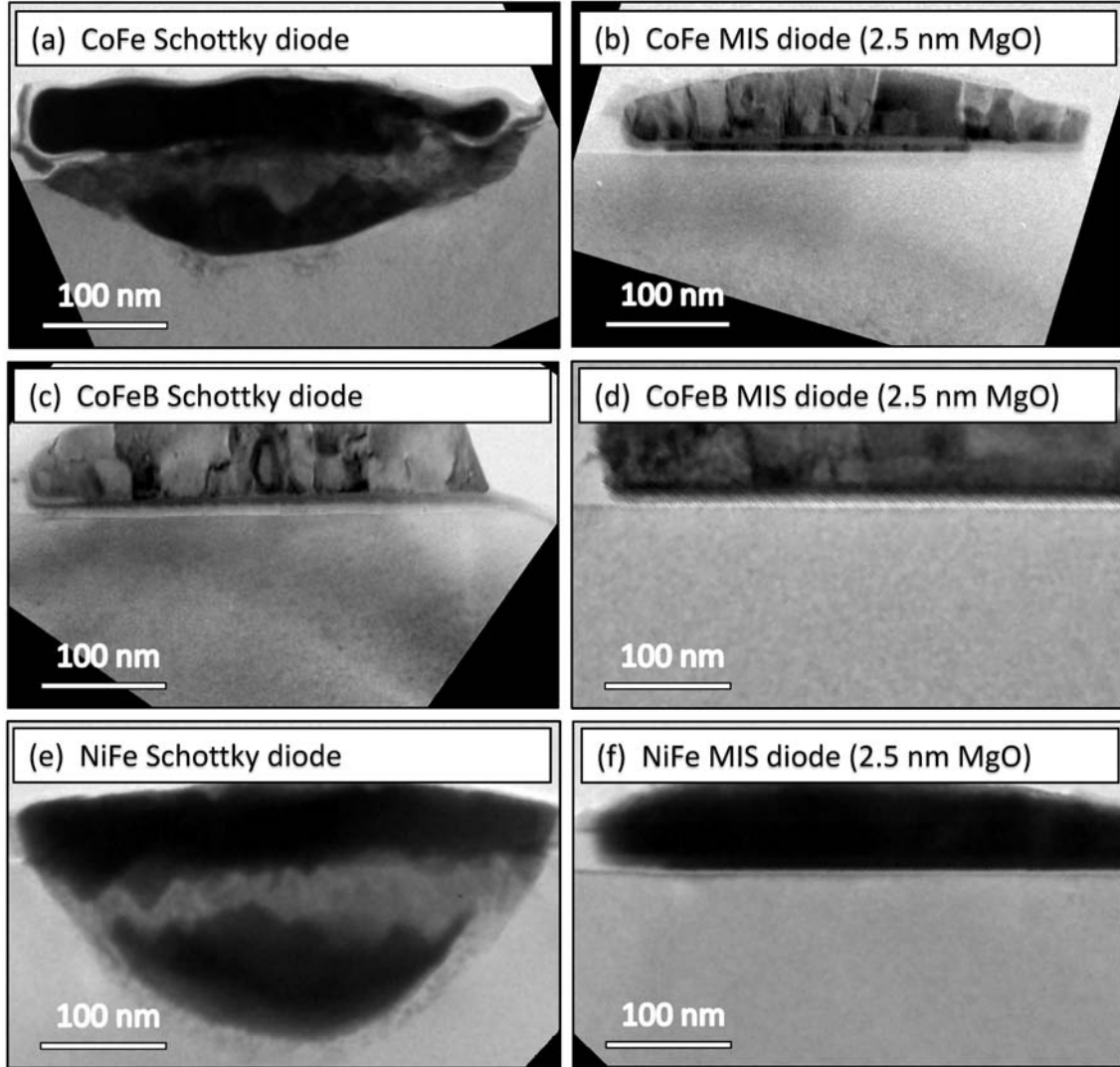


Figure 3.9: Cross-section TEM images of Schottky and MIS diodes annealed at 300°C and subsequently at 400°C for 30 min (in collaboration with A. Kovacs and A. Kohn from Oxford University).

structures an almost atomically flat silicon surface without remanent silicon oxide is achieved. The sputter-deposited layers have sharp interfaces. Different FM electrodes, namely CoFe/NiFe, NiFe and CoFeB have been investigated. The CoFe and NiFe layers are polycrystalline, while CoFeB is amorphous in the as-deposited state and shows dispersed crystallites after annealing up to 400°C, setting the onset of bulk crystallization. In the case of the tunneling diodes, the MgO barrier is amorphous after deposition and annealing up to 400°C. This lack of crystallization is attributed to the large lattice mismatch of crystalline MgO and Si. Furthermore, the thermal stability has been investigated by means of EFTEM, showing no significant intermixing in the case of the tunneling diodes, where MgO is working as an efficient diffusion barrier, even for thicknesses as low as 1.5 nm. For the Schottky

diodes, strong intermixing is present for CoFe/NiFe and NiFe, as expected for these materials. In the case of CoFeB, interdiffusion seems to be below the resolution limit of the used techniques.

3.4 Theoretical background of Schottky and MIS diodes

Prior to the electrical characterization of the spin injection/detection diodes, this section lays out the theoretical background related to semiconductor diode structures.

The energy diagram of an ideal metal/semiconductor and metal-insulator-semiconductor (MIS) diode with zero work function difference between metal and semiconductor is depicted in Fig.3.10, where the symbol explanation is given in the figure caption. In this ideal case, silicon's valence band, E_v , conduction band, E_c , and intrinsic energy, E_i , are flat, corresponding to zero band bending, $\Psi_s = 0$. Furthermore, the silicon/insulator and silicon/metal interface is assumed to be abrupt and trap-free, silicon's doping density is continuous and the oxide is free of traps/charges.

A bias applied at the ferromagnetic electrode either repels or attracts majority carriers from/to the semiconductor surface for thermal equilibrium, resulting in three different occupation states: accumulation, depletion and inversion. These three states, shown in Fig. 3.11, are discussed in the following for the case of a MIS

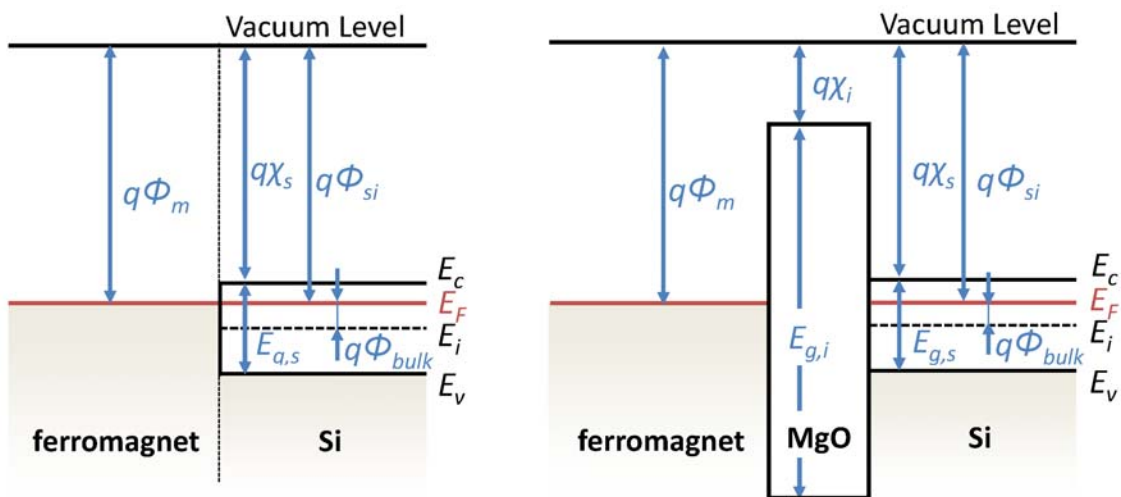


Figure 3.10: Energy diagram of an ideal Schottky and MIS diode on n-Si, with the metal work function ϕ_m , silicon work function ϕ_{si} , Fermi potential ϕ_{bulk} , insulator electron affinity χ_i , semiconductor electron affinity χ_s , silicon band gap $E_{g,s}$ and insulator band gap $E_{g,i}$.

diode on n-doped Si.

Accumulation: For positive metal bias, $V_m > 0$, the majority carriers in n-doped silicon, i.e. electrons, are accumulated at the silicon/insulator interface, while minority carriers (holes) are repelled (Fig. 3.11(a)). The electrons generate a negative charge at the interface, causing a positive band bending $\Psi_s > 0$.

Depletion: For $V_m < 0$ the electrons are repelled from the Si surface, leaving back the positively ionized donor atoms (Fig. 3.11(b)). The depletion of majority carriers results in a negative band bending $\Psi_s < 0$. For further negative V_m midgap is reached, where E_F coincides with E_i , resulting in a vanishing surface potential ϕ_s . At this point, the band bending is equal to the Fermi potential, $\Psi_s = \phi_{bulk}$. Lowering the bias cannot be compensated by dopant ionization anymore, marking the onset of the inversion. The extent of the depletion region reached its' maximum, where any further decrease of V_m is compensated by minority carriers.

Inversion: Two cases are distinguished at inversion, namely weak and strong inversion. For weak inversion (Fig. 3.11(c)) the ionization of donors cannot compensate for the applied bias anymore, causing thermally generated holes to drift from the silicon bulk to the interface region. However, electrons still overbalance holes as mobile carriers in the depletion region. The band bending is ranging between $\phi_{bulk} < \Psi_s < 2\phi_{bulk}$. For more negative V_m values, $\Psi_s = 2\phi_{bulk}$, which marks the beginning of strong inversion, where holes become the dominating carriers at the Si/insulator interface.

This ideal picture is not the usual case, though, for most metal-semiconductor combinations where $\phi_{ms} \neq 0$. In these cases ϕ_{ms} can be calculated according to [5, 6]:

$$\phi_{ms} = \phi_m - \chi_s - \frac{E_{g,s}}{2} + \phi_{bulk} \quad , \text{ for n-doped Si,} \quad (3.1)$$

$$\phi_{ms} = \phi_m - \chi_s - \frac{E_{g,s}}{2} - \phi_{bulk} \quad , \text{ for p-doped Si.} \quad (3.2)$$

The Fermi/bulk potential, ϕ_{bulk} , is defined as:

$$\phi_{bulk} = \frac{k_B T}{q} \ln \left(\frac{N_d}{n_i} \right) , \text{ for n-doped Si,} \quad (3.3)$$

$$\phi_{bulk} = \frac{k_B T}{q} \ln \left(\frac{N_a}{n_i} \right) , \text{ for p-doped Si,} \quad (3.4)$$

where k_B is the Boltzmann constant, T the absolute temperature, q the elementary charge, N_d the n-Si doping density, N_a the p-Si doping density and n_i is the intrinsic carrier density, being $1 \cdot 10^{10} \text{ cm}^{-3}$ for silicon at room temperature.

Another characteristic of Schottky and MIS diode structures is the Schottky barrier

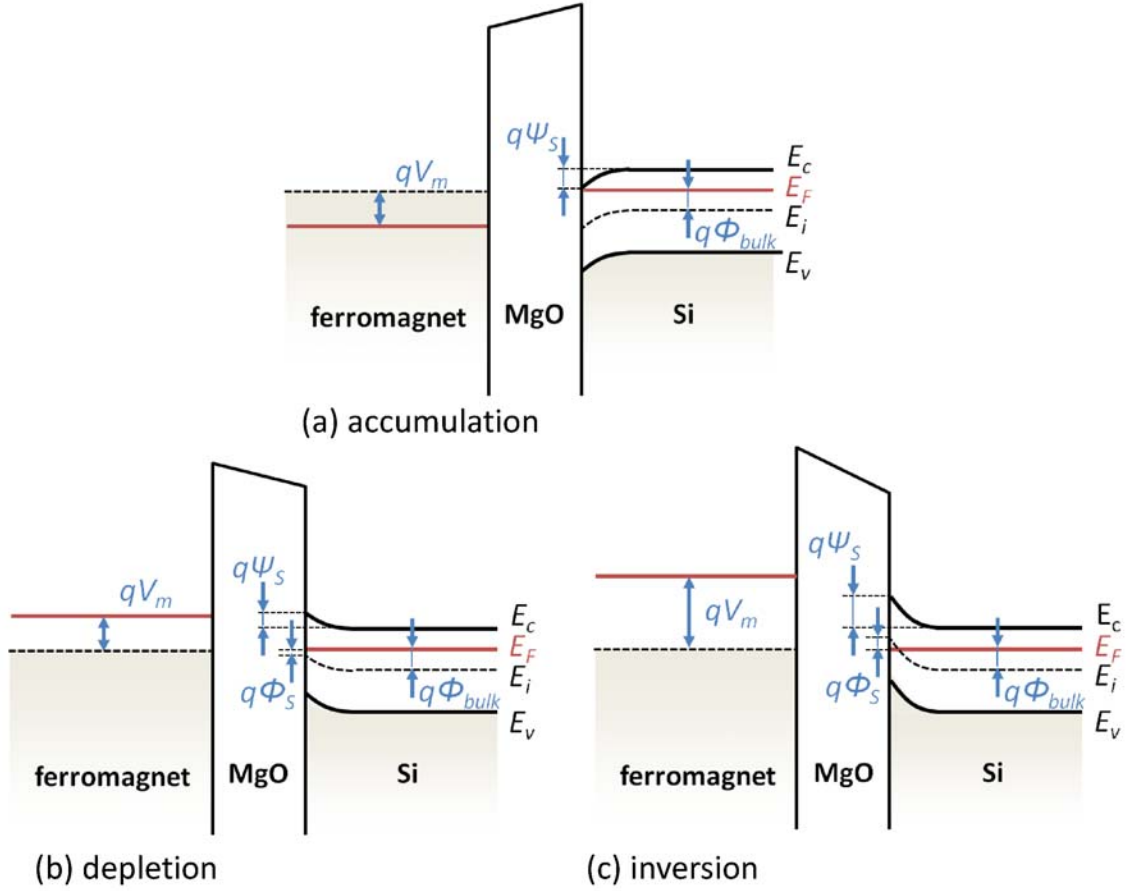


Figure 3.11: Energy diagram of ideal MIS diode on *n*-Si in (a) accumulation, (b) depletion and (c) inversion

height, ϕ_B , defined as the difference of the metal work function, ϕ_m , and the majority band edge of the semiconductor:

$$\phi_B = \phi_m - \chi_s \quad \text{n-doped Si,} \quad (3.5)$$

$$\phi_B = \frac{E_g}{q} + \chi_s - \phi_m \quad \text{p-doped Si.} \quad (3.6)$$

Obviously, ϕ_B is an inherent material property determined by metal and semiconductor, being unaffected by the metal bias. The formation of the Schottky barrier has been also attributed to other factors like pinning due to interface traps or metal induced gap states. Charges of different origin are also responsible for band bending. Such charges can be categorized as follows [5, 6]:

Interface Trapped Charge: These positive or negative charges are located at the Si/insulator interface, resulting from structural imperfections, oxidation-induced defects, metal impurities or any other bond breaking mechanism. The energy states of the interface traps are situated within the Si band gap. Depending on the surface potential, these traps can be charged or discharged,

staying in permanent electrical contact to silicon. Their ability to capture and emit carriers of different type, is altering the diode from the ideal case.

Fixed Oxide Charge: These positive charges within the oxide are immobile and their charge cannot be changed. They are caused by a non-stoichiometric oxide growth. While in thermally grown SiO_2 these charges are situated within less than 2 nm from the Si interface, for sputter deposited oxides their distribution may be continuous over the whole oxide thickness. Unlike the interface traps, fixed oxide charges are not in electrical communication with silicon.

Oxide Trapped Charge: These charges can be positive or negative due to holes or electrons being trapped in the oxide. The trapping may result from hot carrier injection, Fowler-Nordheim tunneling, ionizing radiation or other mechanisms. Most of these charges can be compensated by low-temperature annealing, although neutral traps may remain.

Mobile Oxide Charge: The amount of mobile charges in the oxide is dependent on the deposition technique, where e.g. Na^+ and K^+ ions are generated by thermal oxide growth.

The width of the depletion region sets another characteristic parameter for the diodes' transport properties. The maximum depletion width W_m can be calculated for any given doping density N_D by solving the Poisson equation [6]:

$$W_m = \sqrt{\frac{4\epsilon_s k_B T \ln(N_D/n_i)}{q^2 N_D}} \quad (3.7)$$

Increasing the silicon's doping density from 10^{15}cm^{-3} to 10^{18}cm^{-3} limits the width of the depletion region from 900 nm down to 20 nm.

Characteristic energy band parameters for ferromagnetic Schottky and MIS diodes are shown in Table 3.1. It should be pointed out that all 3d-ferromagnets employed in this work, have a metal work function around $\phi_m \sim 5$ V. Applying the values from Table 3.1, gives a $\phi_{ms} = 0.38$ V for n-doped and $\phi_{ms} = -0.24$ V for p-doped Si, i.e. in both cases the Si surface should be depleted at zero applied bias. In the absence of parasitic charges the ϕ_{ms} values correspond to the flat-band voltage. In the special case of MIS diodes also tunneling through the insulator has to be considered. The tunneling barrier heights for electrons, ϕ_B^{el} , and holes, ϕ_B^{h} , can be calculated from the following relations:

$$q\phi_B^{\text{el}} = q\phi_m - q\chi_i = 3.3\text{eV} \quad (3.8)$$

$$q\phi_B^{\text{h}} = E_{g,i} + q\chi_i - q\chi_s - E_{g,s} = 3.25\text{eV} \quad (3.9)$$

Due to the similarity of the barrier height values as well as the effective masses of electrons and light holes (Table 3.1), significant tunneling contributions from both types of carriers can be expected. This is in contrast to the case of SiO_2 , where the barrier height for holes is significantly larger than for electrons [6].

Table 3.1: Energy band parameters for ferromagnetic Schottky and MIS diodes

Metal work function for CoFe ϕ_m	4.8 V
Metal work function for CoFeB ϕ_m	4.8 V
Metal work function for NiFe ϕ_m	5.0 V
MgO energy gap $E_{g,i}$	7 eV
MgO electron affinity χ_i	1.5 V
MgO effective mass of electrons m_e^*	$0.35m_e$ [7]
MgO effective mass of holes m_h^*	$0.33m_e$ [7]
Si energy gap $E_{g,s}$	1.1 eV
Si electron affinity χ_s	4.15 V
Work function of n-doped Si ($1 \cdot 10^{15} \text{ cm}^{-3}$) ϕ_{si}	4.42 V
Work function of p-doped Si ($1 \cdot 10^{15} \text{ cm}^{-3}$) ϕ_{si}	5.04 V

While thermionic emission of the carriers over the Schottky barrier is dominating for low doping densities, the tunneling contribution through the edge of the Schottky barrier gains importance for larger doping, referred to as field emission. The current, I , as a function of the metal bias, V , across a metal-semiconductor contact can be described by the thermionic emission theory according to the equation [5, 6]:

$$I = I_s \exp\left(\frac{qV}{nk_B T} - 1\right) \approx I_s \exp\left(\frac{qV}{nk_B T}\right), \text{ for } qV > 3k_B T. \quad (3.10)$$

q is the elementary charge, k_B the Boltzmann constant, T the absolute temperature and n the ideality factor of the Schottky diode. The saturation current, I_s , writes:

$$I_s = AA^* T^2 \exp\left(-\frac{q\phi_{B,eff}}{k_B T}\right), \quad (3.11)$$

where A is the diode area, A^* the Richardson constant of the Si and $\phi_{B,eff}$ the effective Schottky barrier height (SBH), which is the zero-bias SBH reduced by the image force and other non-idealities. The n and I_s can be determined from the slope and the intersect of the linear fit of the $\log(I)$ - V plot at low forward bias (Eq. 3.10). From temperature-dependent IV measurements and the equation:

$$\ln(I_s/T^2) = \ln(AA^*) - \frac{q\phi_{B,eff}}{k_B T} \quad (3.12)$$

we can extract the $\phi_{B,eff}$ as the slope of the Arrhenius plot. This technique provides accurately the area-independent $\phi_{B,eff}$, even if the Richardson constant is not accurately known [6].

To describe the effect of the tunneling barrier on the diodes' IV characteristics, Eq.3.11 has to be modified as follows:

$$I_s = AA^* T^2 \exp(-\alpha_T \phi_T^{-1/2} d) \exp\left(-\frac{q\phi_{B,eff}}{k_B T}\right) \quad (3.13)$$

so as to include the tunneling probability $\exp(-\alpha_T \phi_T^{-1/2} d)$. α_T depends on the carrier effective mass inside the barrier, d is the insulator thickness and ϕ_T is the insulator barrier height.

The applied bias drops partly in the semiconductor and partly in the insulator. In the presence of an extended depletion region the current is semiconductor-limited, since its resistance is dominating the one of the tunneling barrier. Fixed oxide charges add an additional electric field, which modifies the band bending at the silicon surface. In addition, the interface trap density can be altered in the presence of the oxide, compared to the Schottky diodes.

3.5 Electrical characterization of n-Si diodes

As mentioned earlier, the conductivity mismatch can be circumvented by introducing a spin-dependent resistance, in the form of a Schottky or tunneling barrier, at the interface to Si [8, 9, 10]. The presence of an insulator film as tunneling barrier is considered necessary to inhibit material interdiffusion. The interfacial resistance must be tuned to a narrow window to ensure considerable spin-polarized current injection. Tuning parameters are the Schottky and the tunneling barrier's thickness and height. Since the Schottky barrier, originating from the depleted Si surface, dominates the total resistance, its restriction is critical. The Schottky barrier height depends on the ferromagnet work-function and its width on the silicon doping density [11, 12, 13]. Gd, due to its low work-function leads to a low Schottky barrier height in n-Si, but its spin polarization and the Curie temperature are relatively low [14]. On the other hand, restricting the Schottky barrier width by increasing the silicon doping density, results in a smaller spin diffusion length [15, 16]. From the above, we understand that finding the right combination of parameters, that ensure high spin injection efficiency, is not a trivial task and a systematic study is therefore required. We begin our study with the investigation of Schottky and MgO-based tunneling diodes on n-doped silicon (001).

3.5.1 Ferromagnetic n-Si Schottky diodes

In Fig.3.12 we present typical JV measurements of $10 \times 15 \mu\text{m}^2$ rectangular diodes as a function of the FM electrode and N_D , taken at room-temperature (RT). At reverse bias, electrons flow from the metal to the semiconductor (spin injection), while under forward bias electrons flow from the semiconductor into the metal (spin detection). The IVs on the left side correspond to as-deposited diodes and on the right side to annealed diodes at 400°C . All the IVs have been recorded in the dark using a HP4156C parameter analyzer and a temperature-controlled chuck. The electrical ground contact to the substrate has been established at the top side of the wafer, on the doped Si layer. The rectification of the as-deposited IVs is around 10^6 for N_d

$= 10^{15}\text{cm}^{-3}$, decreasing to about 10^4 for $N_d = 10^{18}\text{cm}^{-3}$. Since Schottky contacts are majority carrier devices, this high rectification is related to a large electron SBH [6]. The current density for large forward bias (>0.5 V) is limited by the R_s of the substrate and measurement apparatus. For larger doping densities the R_s is smaller and therefore the current density is higher. Typical values for R_s range from 2.5 k Ω down to 250 Ω for N_d of 10^{15} and 10^{18}cm^{-3} , respectively. The current's reverse bias dependence is small for diodes with $N_d \leq 10^{17}\text{cm}^{-3}$, with current densities in the range of 1-100 A/m². For the case of 10^{18}cm^{-3} the diodes exhibit a relatively pronounced bias dependence, with a current density up to 10^4 A/m² at -1.25 V. The IVs of the diodes annealed at 300°C show similar current densities to the as-deposited ones. Only after annealing at 400°C, changes were observed in the IV characteristics, which strongly depend on the FM electrode material. The most moderate changes occur for the CoFe Schottky diodes. While still showing a pronounced rectifying behavior, the current density is increased by one order of magnitude for low forward and reverse bias and up to two orders of magnitude for the case of $N_d = 10^{18}\text{cm}^{-3}$. On the other hand, the most markeable changes occur for CoFeB and especially NiFe diodes, for which the current density increases after annealing by several orders of magnitude, depending on N_d . These changes of the electrical properties with the annealing are further discussed with respect to the SBH and n in the following.

In accordance to Eq.3.10 we have extracted the n and I_S from a linear fit of the low forward bias regime, between 0.1 and 0.2 V. The area-independent SBH is extracted from the Arrhenius plots for temperatures ranging from 298 K to 358 K, in steps of 10 K. Fig.3.13 depicts such Arrhenius plots for $N_d = 10^{15}\text{cm}^{-3}$ for different FM electrodes and T_A . The good linear fit of the experimental data shows that thermionic emission accurately describes the transport properties. The extraction of the basic diode parameters has been carried out for rectangular diodes, with surface area from 200 down to 6 μm^2 . In Fig.3.14 we summarize the extracted average values for the SBH and n at RT as a function of N_d and T_A for the different FM electrode materials. The ideality factor, n , of the as-deposited diodes is very close to unity for all ferromagnets, which indicates that there is no residual oxide at the interface with Si, in accordance with the HRTEM results (Fig.3.12). The increase of n with N_d is due to the exponential increase of the tunneling current through the depletion region with the square root of N_d [6]. Indeed, for the highest doping ($N_D = 10^{18}\text{cm}^{-3}$) the calculated ratio of thermionic emission to tunneling current through the Schottky barrier is in the range of 10 [6]. The same reason accounts for decrease of the effective barrier height with increasing N_d in combination with the doping-dependent image force lowering [6, 17].

The SBH of the as-deposited diodes is close to 0.7 eV for $N_D = 10^{15}\text{cm}^{-3}$ and independent of the FM metal work function, Φ_m , which is 4.8 eV for CoFe(B) and 5.0 eV for NiFe. This shows that Fermi level pinning due to interface states may be determining for the Schottky barrier formation [5, 6, 18]. Annealing at 300°C results to slightly reduced SBH and increased n , without altering their general trend as a function of N_d . On the contrary, the SBH is dramatically decreased after annealing at 400°C for the NiFe and CoFeB diodes, especially for low doping densities. The decrease of the SBH is accompanied by an increase of n . Changes are limited for

CoFe diodes.

In the structural investigation it has been shown that NiFe-based diodes degrade the most after annealing due to the large diffusion coefficient of Ni. On the other hand, the diffusion of CoFeB was below the resolution limit of TEM and certainly much smaller than for CoFe. The investigation of the transport properties, nevertheless, yields different results; i.e. the degradation of the CoFeB diodes is larger than the one of the CoFe diodes. This actually shows that the transport measurements are much more sensitive on atomic-scale diffusion than TEM investigations. Any diffusion of boron at the SC's interface can lead to a change of the doping profile since boron acts as an acceptor. This would certainly give rise to altering of the transport properties of the n-Si diodes.

Noteworthy, the highest doped CoFeB and NiFe diodes present larger thermal stability than the low doped. This is in contradiction to the reported increase of Co and Fe solubility in Si with increasing doping density [19], as well as to the small dependence of Ni solubility on N_d [20]. On the other hand, though, increased doping can result to mechanically stiffer lattices to be distorted or substituted [21].

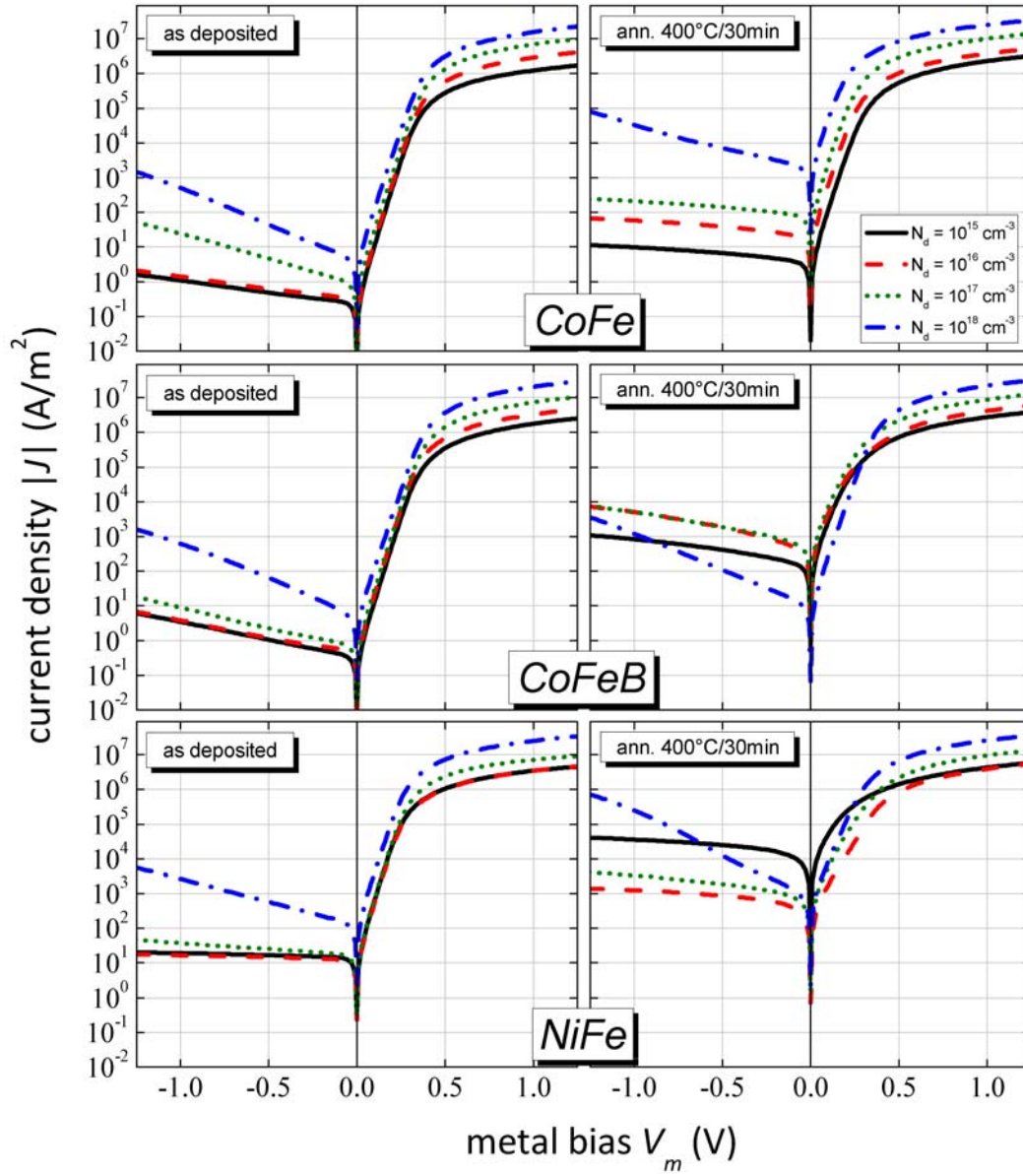


Figure 3.12: Room temperature IV measurements of ferromagnetic Schottky diodes on n-Si(100) with four different doping densities of 10^{15}cm^{-3} (black full), 10^{16}cm^{-3} (red dashed), 10^{17}cm^{-3} (green dotted) and 10^{18}cm^{-3} (blue chain) for rectangular elements of $10\times 15\mu\text{m}^2$. The IVs for the as deposited case are shown on the left hand side and for an annealing of 400°C for 30min in Ar on the right hand side for three different ferromagnetic materials CoFe (top row), CoFeB (middle row) and NiFe (bottom row).

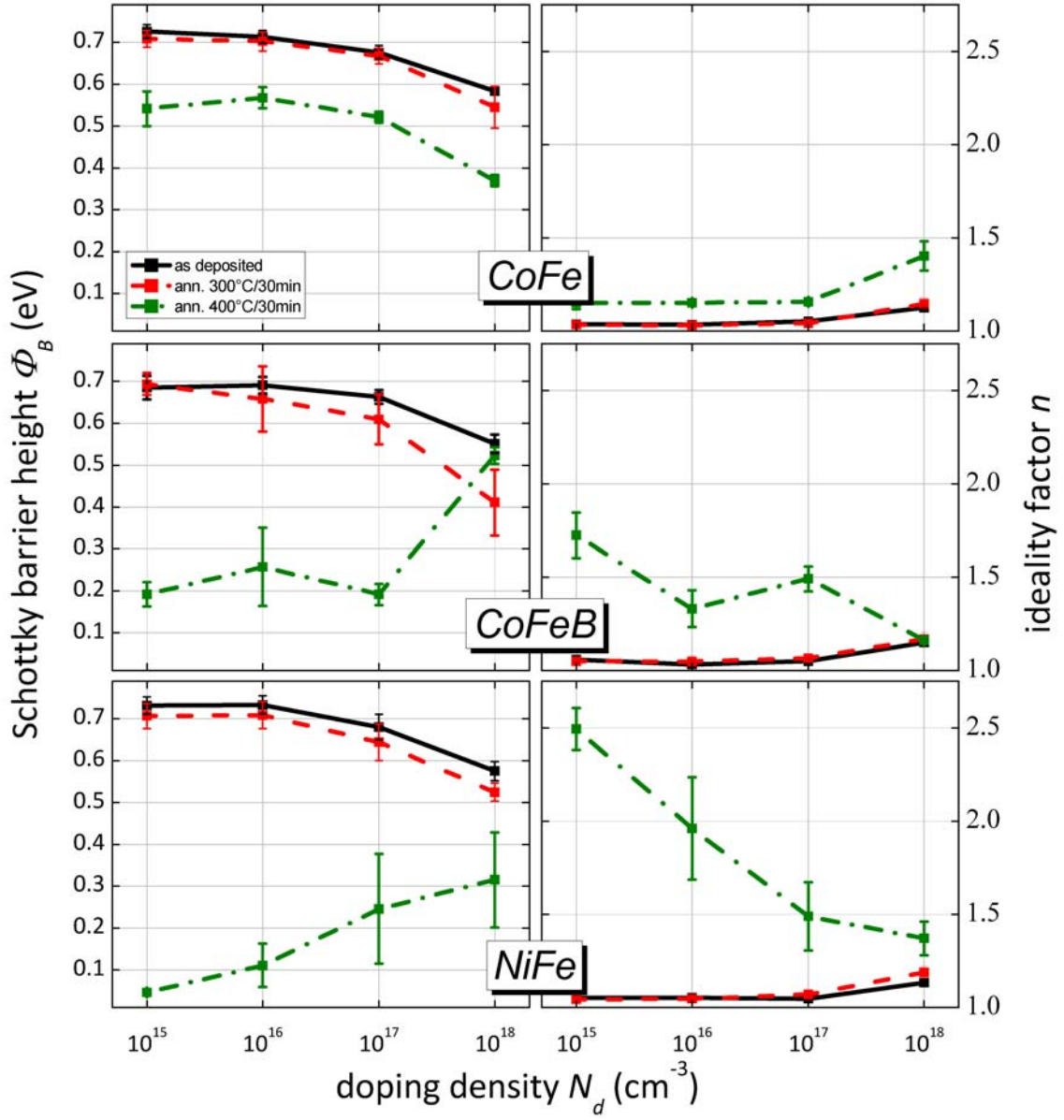


Figure 3.13: Plots of the average SBH and ideality factor for different FM electrodes over the doping density, for the as-deposited diodes (black full), annealed at 300°C (red dashed) and 400°C (green chain).

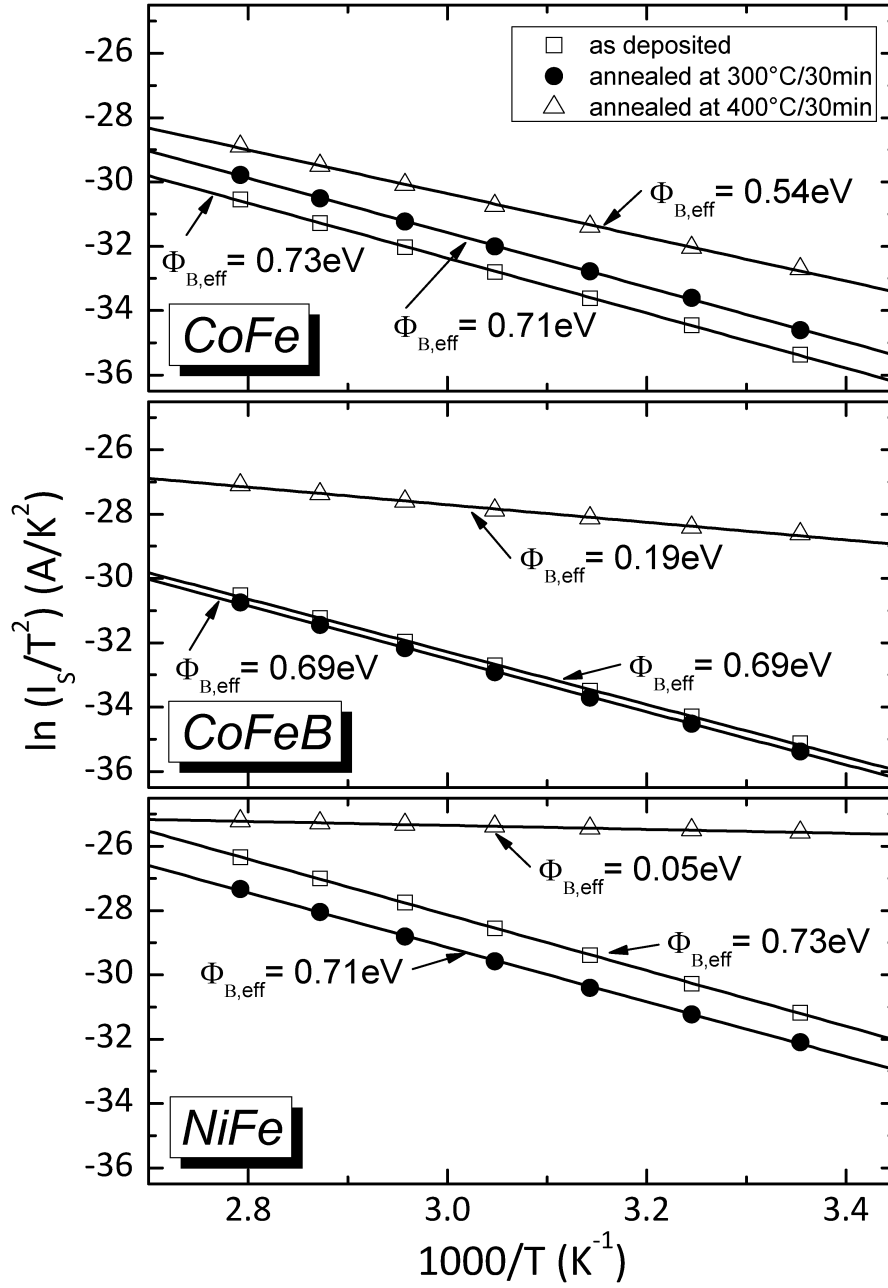


Figure 3.14: Arrhenius plots of the saturation current $\ln(I_s/T^2)$ versus $1/T$ for 10^{15} cm^{-3} doped n-Si with CoFe (top), CoFeB (middle) and NiFe (bottom). The effective barrier height $\Phi_{B,eff}$, corresponding to the slope of the linear fit, is depicted for the as-deposited case (open square), annealed at 300°C (full circle) and 400°C (open triangle).

3.5.2 Ferromagnetic n-Si MIS tunneling diodes

At the left side of Fig.3.15 and 3.16 we present RT IVs of the as-deposited MIS diodes for $d = 1.5$ and 2.5 nm, respectively. For MgO, the calculated barrier heights for electrons and holes are 3.3 and 3.25 eV, respectively. Similar effective masses for electrons and light holes are extracted from band structure calculations, with values of $0.35m_e$ and $0.33m_e$, respectively [7]. As a result, both carrier types can have considerable contributions to current transport [11]. Nevertheless, the measured IV characteristics are consistent with non-equilibrium type MIS diodes, dominated by majority carrier transport and/or surface states [22, 23]. This is mainly supported by the small temperature dependence of the IVs for low forward and reverse bias (not shown here), where the current is semiconductor-limited [22, 23].

From Eq.3.13, the tunneling probability through the MgO barrier should cause the decrease of the current density compared to the Schottky contacts. In contrast to this, the MIS diodes incorporating 1.5 nm MgO (Fig.3.15) feature increased current density for reverse and low forward bias compared to the Schottky diodes. More precisely, the reverse current, which is relevant for electron injection in the semiconductor, is increased by a factor of 10^2 to 10^3 for $N_D = 10^{15}\text{cm}^{-3}$ and by 10 to 10^2 for $N_D = 10^{18}\text{cm}^{-3}$. In addition, we notice from Fig.3.15 and 3.16 that the position of the current plateau at reverse bias is shifted to more negative bias values as the MgO thickness increases. This shift is approximately $\Delta V = 0.31\text{V}$ for the diodes with $d = 2.5$ nm, compared to the Schottky ones. If ΔV is exclusively attributed to the positive oxide charges in the insulator, then their density, Q_f , can be calculated from the formula:

$$Q_f = C_{ox}\Delta V = \frac{\epsilon_0\epsilon_r}{d}\Delta V, \quad (3.14)$$

where ϵ_0 is the vacuum permittivity and $\epsilon_r = 8.4$ is the relative dielectric constant of MgO, extracted from capacitance-voltage measurements [24].

The calculation yields $Q_f \approx 6 \times 10^{12}\text{cm}^{-2}$, which is about an order of magnitude higher compared to values reported for SiOx [25, 26]. A large positive fixed oxide charge density is, nevertheless, expected for sputter-deposited MgO in pure Ar atmosphere due to oxygen deficiency. Apart from the Q_f , the interface trap density of the sputter-deposited MgO diodes is shown to be as high as $8 \times 10^{13} \text{ eV}^{-1}\text{cm}^{-2}$ [11]. The combination of both factors can explain the increased current density of the $d = 1.5$ nm MIS diodes, compared to the Schottky ones. However, increasing the MgO thickness to 2.5 nm (Fig.3.16) leads to a significant increase of the contact resistance by a factor of 10 to 100 for low forward and low reverse bias ($< |0.5|$ V) compared to the case of $d = 1.5$ nm. This applies to all investigated diodes.

From the temperature-dependent IVs and the resulting Arrhenius plots $\ln(I_r/T^2)$ versus $(1/T)$:

$$\ln(I_r/T^2) = \ln(AA^*) - \left(\alpha_T\phi_T^{-1/2}d\right) - \frac{q\phi_{B,eff}}{k_B T} \quad (3.15)$$

we have extracted the $\phi_{B,eff}$ for all reverse bias values. In contrast to the Schottky diodes, where the effective SBH is bias-independent, for the MIS it is only the case

when $V < 0.25$ V for $d = 1.5$ nm and $V < 0.75$ V for $d = 2.5$ nm. At the right column of Fig.3.15 and 3.16 we plot the effective SBH for MIS diodes as a function of the FM electrode, N_d and T_A , using the current density values, which correspond to a bias of -0.3 V for $d=1.5$ nm and -1 V for $d = 2.5$ nm. Fig.3.17 shows the Arrhenius plots for rectangular MIS diodes of $10 \times 15 \mu\text{m}^2$ with $d = 1.5$ nm in the as-deposited state. The obtained $\phi_{B,eff}$ for all MIS diodes are more than halved compared to the Schottky diodes. This, for one, reflects the pronounced non-idealities induced by the presence of MgO, with diode ideality factors ranging from 2.9 to 3.1. These n values are related to the high interface trap density of the MgO/Si interface. Besides, the positive fixed oxide charges have been shown to lower considerably the SBH for electrons [26]. Many authors have tried to use the correlation between n and $\phi_{B,eff}$ in order to extract a bias-independent SBH defined at flat-band conditions [27, 28, 29, 30, 31]. The resulting correction gives rise to a higher SBH value. Nevertheless we consider that the "uncorrected" $\phi_{B,eff}$ values are representative of the overall diodes' non-ideal transport properties.

The general trend of decrease of $\phi_{B,eff}$ with N_D (Fig.3.15 and 3.16) is merely the effect of image force lowering and increased tunneling contribution through the depletion region. Independent of the FM, d and N_d , annealing at 300°C for 30 min in Ar is decreasing the SBH by around 0.03 eV. The same can be observed after annealing at 400°C for 30 min in Ar, lowering the SBH by another 0.06 eV. This is reflected on an increasing current density for every bias regime with annealing. Since the TEM investigation showed no intermixing up to 500°C for CoFe and CoFeB MIS diodes we can attribute again these changes to structural and chemical modifications beyond the TEM resolution limits.

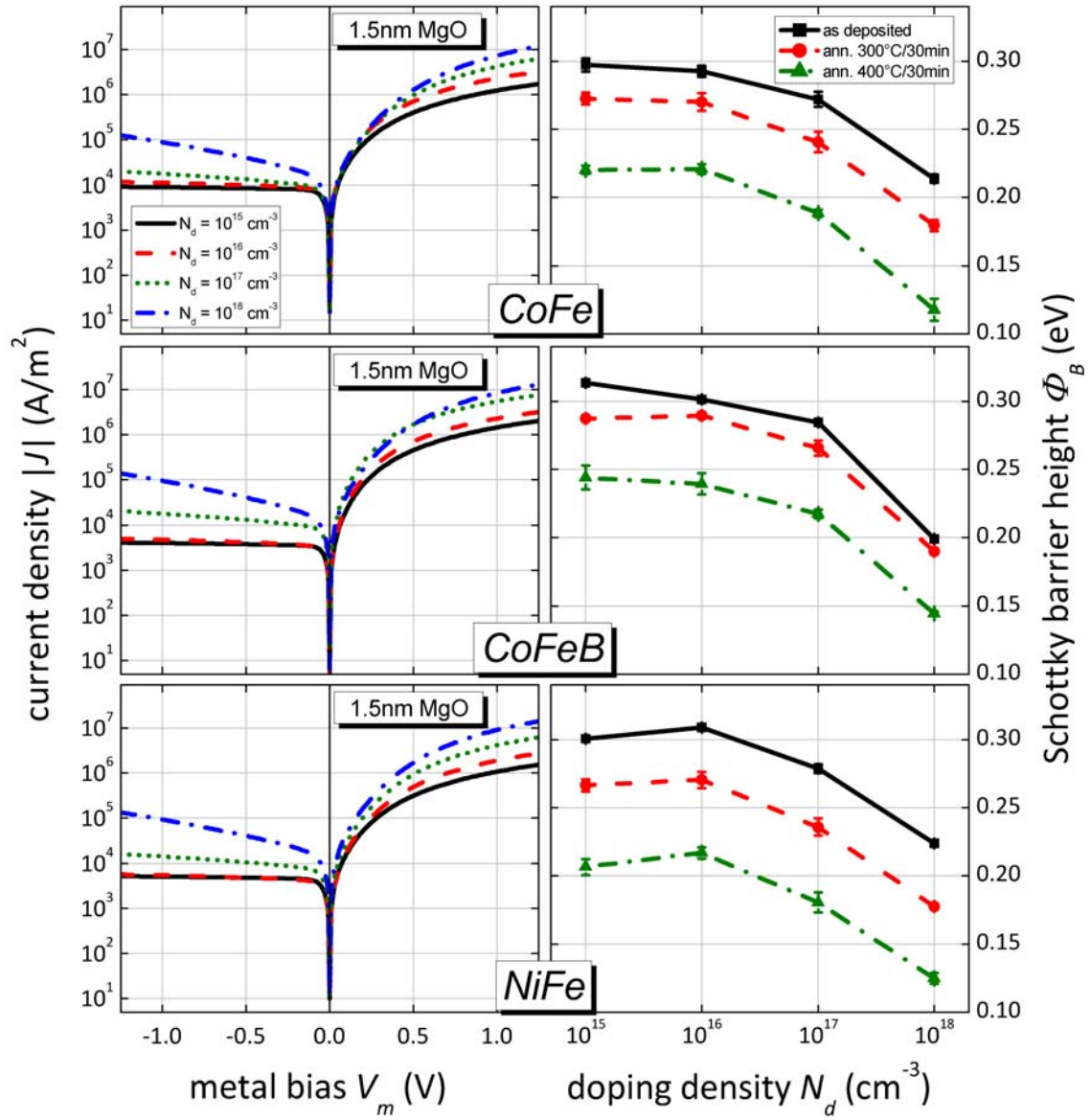


Figure 3.15: Room temperature IV measurements of ferromagnetic MIS diodes with a 1.5 nm MgO tunneling barrier on n-Si(100) with four different doping densities of 10¹⁵ cm⁻³ (black full), 10¹⁶ cm⁻³ (red dashed), 10¹⁷ cm⁻³ (green dotted) and 10¹⁸ cm⁻³ (blue chain) for rectangular elements of 10x15 μm². The corresponding Schottky barrier heights (right side) have been extracted from temperature dependent IV measurements for the as deposited case (black full), annealed at 300° C (red dashed) and 400° C (green chain) for 30min in Ar.

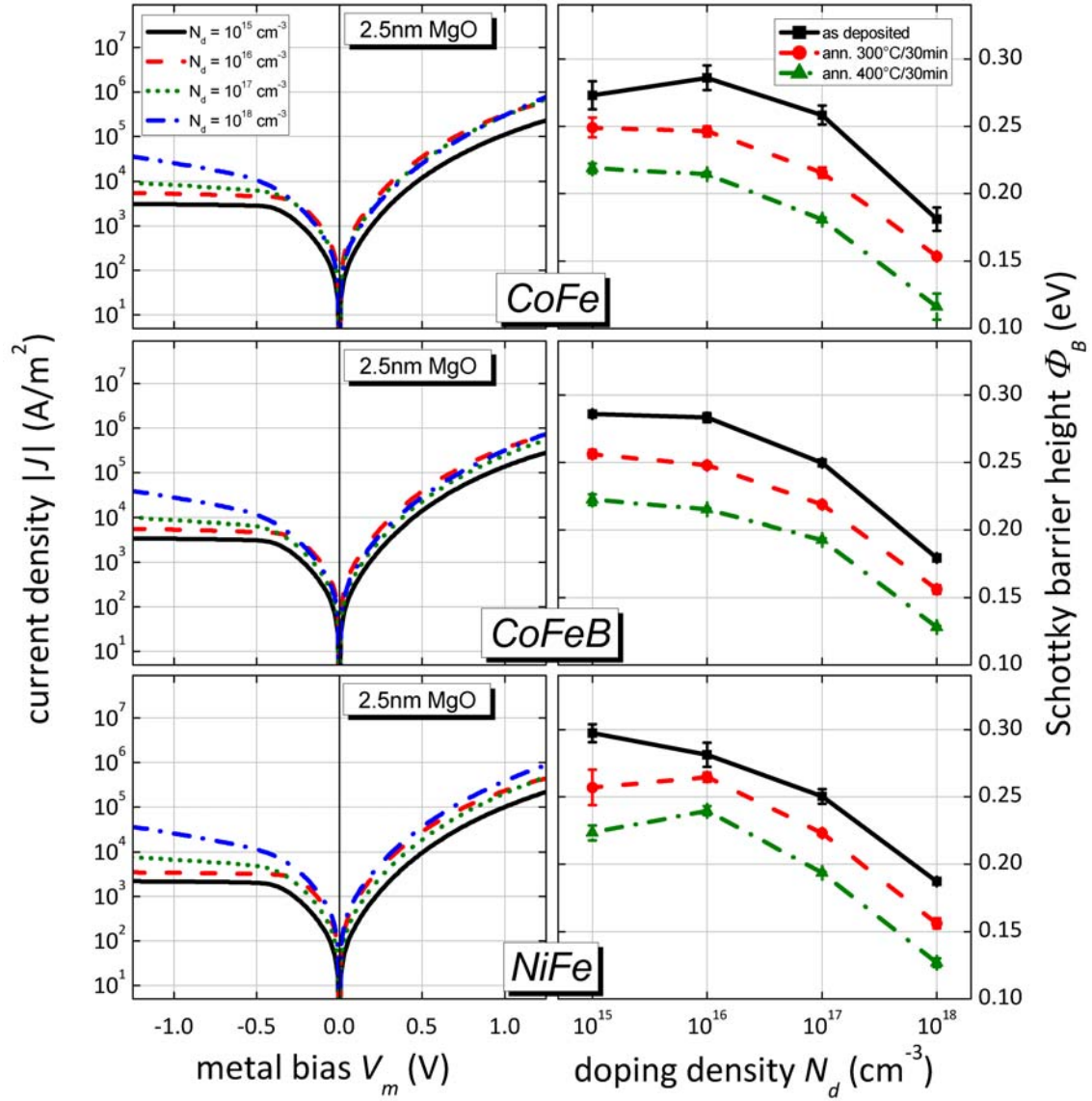


Figure 3.16: Room temperature IV measurements of ferromagnetic MIS diodes with a 2.5 nm MgO tunneling barrier on n-Si(100) with four different doping densities of 10^{15} cm^{-3} (black full), 10^{16} cm^{-3} (red dashed), 10^{17} cm^{-3} (green dotted) and 10^{18} cm^{-3} (blue chain) for rectangular elements of $10 \times 15 \mu\text{m}^2$. The corresponding Schottky barrier heights (right side) have been extracted from temperature dependent IV measurements for the as deposited case (black full), annealed at 300°C (red dashed) and 400°C (green chain) for 30min in Ar.

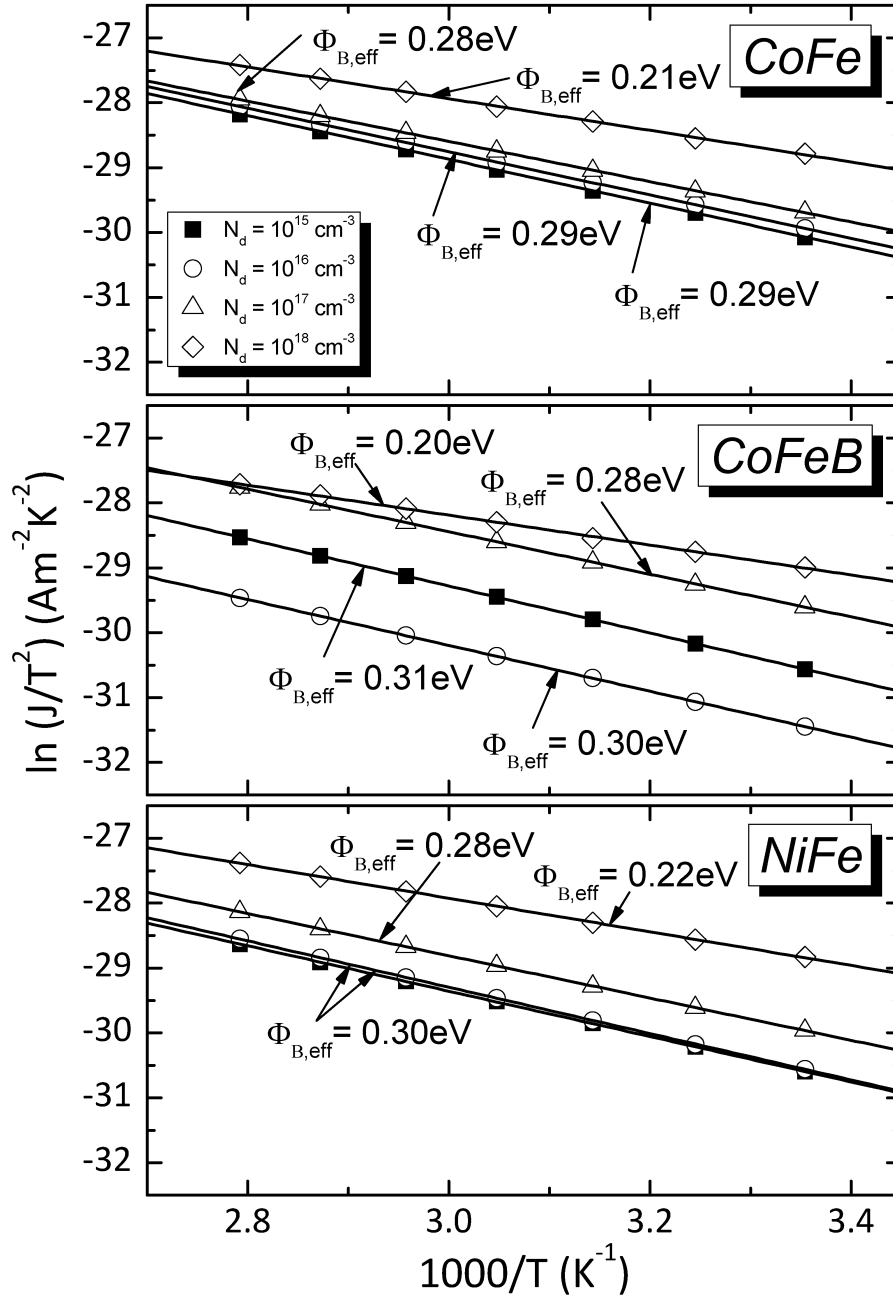


Figure 3.17: Arrhenius plots of the reverse current $\ln(I_R/T^2)$ versus $1/T$ at -0.3V for a 1.5nm MgO tunneling barrier and CoFe (top), CoFeB (middle) and NiFe (bottom) as a ferromagnetic electrode. Linear fit of the barrier height at different doping densities of 10^{15} cm^{-3} (full square), 10^{16} cm^{-3} (open circle), 10^{17} cm^{-3} (open triangle) and 10^{18} cm^{-3} (open diamond) for the as deposited case of $10 \times 15 \mu\text{m}^2$ rectangular junctions.

3.6 Electrical characterization of p-Si diodes

Up to now, solely n-doped Si, featuring less spin scattering than p-Si, has been considered as a host medium for spin-polarized current. However, as it has been shown in the previous section, reverse-biased, n-Si contacts present low injection currents, originating from an extended depletion region [32, 12]. Increasing the doping density to restrict the depletion region, acts detrimentally for the spin relaxation time, τ_s , since this is scaling as $\tau_s \sim 1/N_a$ [16]. In the following we present a different approach to circumvent the conductivity mismatch issue in two-terminal devices, using MIS diodes on p-Si, where spin injection takes place under forward bias [33]. The expected decrease of spin life time due to the electron-hole interaction can be compensated by using lower doping levels in the semiconductor. These aspects will be discussed in the following.

3.6.1 Ferromagnetic p-Si Schottky diodes

In Fig.3.18 we present typical room-temperature (RT) current density versus voltage (JV) measurements of $50 \mu\text{m}^2$ rectangular Schottky diodes in the as-deposited state and after annealing at 400°C as a function of the p-Si doping density N_a . For diodes that have not been annealed, a clear interface without interdiffusion is obtained, as already stretched out in the structural characterization. For p-Si diodes, forward bias (positive V_m) corresponds to electron injection, while reverse bias (negative V_m) corresponds to electron detection. Electrical transport in Schottky diodes is dominated by majority carriers - in the particular case, holes. Consequently, the SBH for holes will determine the transport property to a large extent. At forward bias, the hole current is directed from the silicon to the metal, while at larger bias electrons drift from the metal to silicon's conduction band. The current density at this regime is limited by the series resistance of the semiconductor and measurement apparatus. At reverse bias, hole current flows into the semiconductor, while minority carriers drift towards the metal at larger bias.

CoFeB diodes show a large dependence of the reverse bias current as a function of N_a , whereas CoFe and NiFe present more stable reverse current values. After annealing at 400°C , changes in the current behavior are observed for all Schottky diodes. In this case also the deterioration of the diode parameters can be directly linked to the diffusion of magnetic material into silicon.

The bias-dependent SBH has been extracted from the slope of $\ln(J_r/T^2)$ as a function of $1/kT$, with J_r being the reverse-bias current density and T the absolute temperature, assuming thermionic emission-diffusion mechanism [6, 5] (as already described in Sec.3.5.1). For this purpose temperature-dependent JVs have been measured in the temperature range from 298 to 358 K. The SBH extracted for a reverse bias of $V_m = 0.2$ V is depicted on the left of Fig.3.19 as a function of N_a and T_A . In addition, the ideality factor, n , has been extracted from the linear fit of the RT semi-logarithmic JV curves at low forward bias and is shown at the right hand side

of the the same figure. Typical Arrhenius plots, used for the extraction of $\phi_{B,eff}$ of as-deposited Schottky diodes are depicted in Fig.3.20 as a function of the FM electrode material and N_a . The good linear fit strongly indicates thermionic emission as the dominant current transport mechanism for all FMs and N_a . It should be pointed out that also for annealed Schottky diodes a good fit with thermionic emission diffusion theory has been observed, despite strong interdiffusion.

Compared to the n-Si diodes, the diodes on p-Si present much larger ideality factors. This can be seen in many cases in the literature. The Schottky barrier height for the as-deposited junctions lies between 0.3 to 0.5 eV. The observed changes of $\phi_{B,eff}$ and n as a function of N_a cannot be attributed to the image force and depletion layer width on N_a , as in the case of n-Si diodes, where only mild variations were observed. Contribution from interface states-mediated tunneling can, on the other hand, invoke such large variations of $\phi_{B,eff}$ and n with N_a . Specifically, the presence of metal induced gap states (MIGS) at the vicinity of the semiconductor's valence band is compatible with two main observations: (i) that the changes in $\phi_{B,eff}$ and n are highly correlated and (ii) that these only appear for one doping type [34]. The J_r presents small bias dependence for all but one of the investigated diodes. The exception is the 10^{15} cm^{-3} -doped diode, the JV of which features a low reverse bias hump, denoting the transition from depletion to inversion. This transition is not present for larger N_a due to the higher voltage required to invert the interface. The $\phi_{B,eff}$ decreases with the annealing temperature with an accompanying increase of n . The most pronounced changes in the junctions' transport properties once again are observed for the NiFe case due to aforementioned reasons. CoFe and CoFeB diodes on highly doped silicon present the highest robustness against thermal budget.

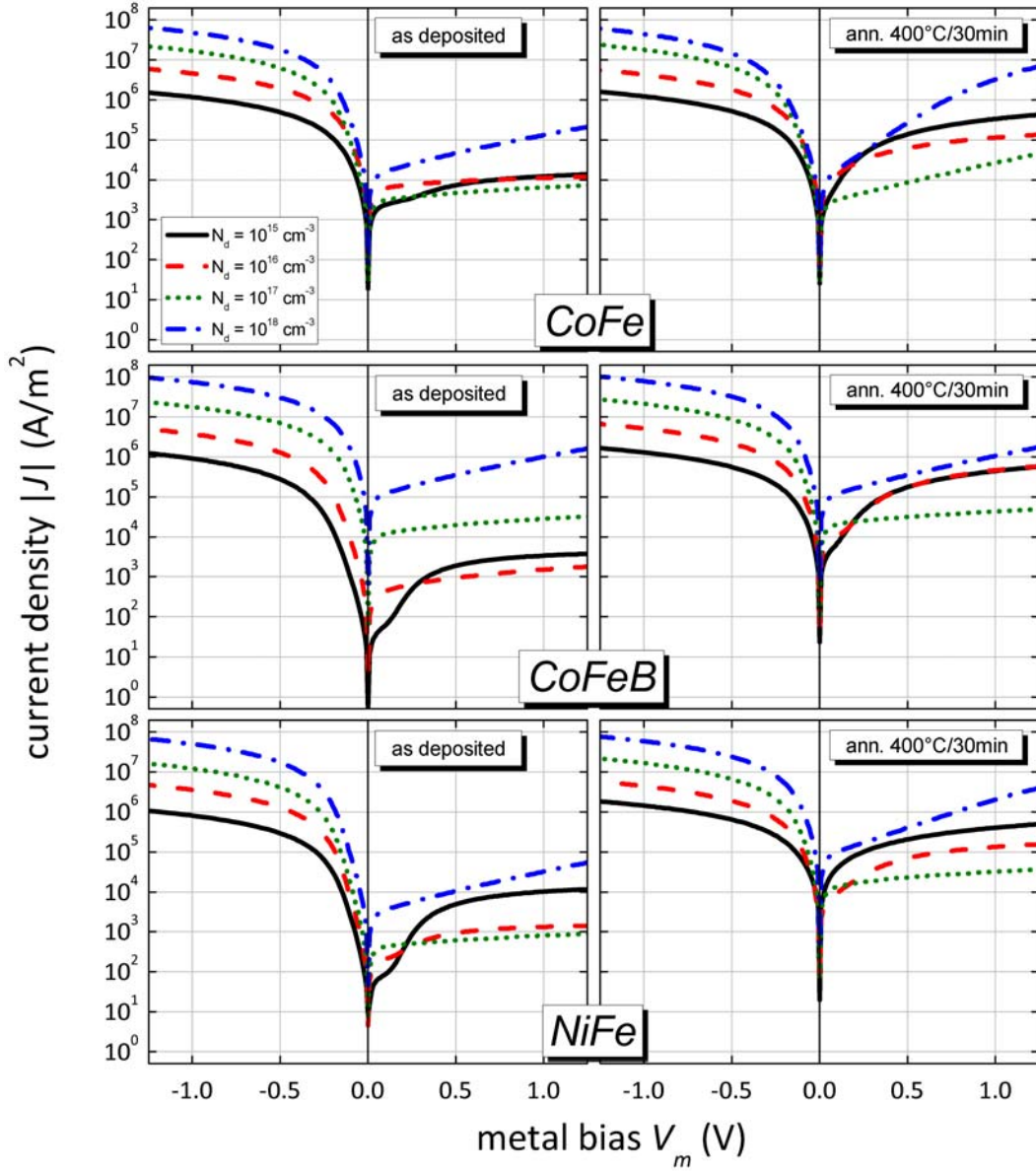


Figure 3.18: Room temperature IV measurements of ferromagnetic Schottky diodes on $n\text{-Si}(100)$ with four different doping densities of 10^{15}cm^{-3} (black full), 10^{16}cm^{-3} (red dashed), 10^{17}cm^{-3} (green dotted) and 10^{18}cm^{-3} (blue chain) for rectangular elements of $10\times 15\mu\text{m}^2$. The IVs for the as deposited case are shown on the left hand side and for an annealing of 400°C for 30min in Ar on the right hand side for three different ferromagnetic materials CoFe (top row), CoFeB (middle row) and NiFe (bottom row).

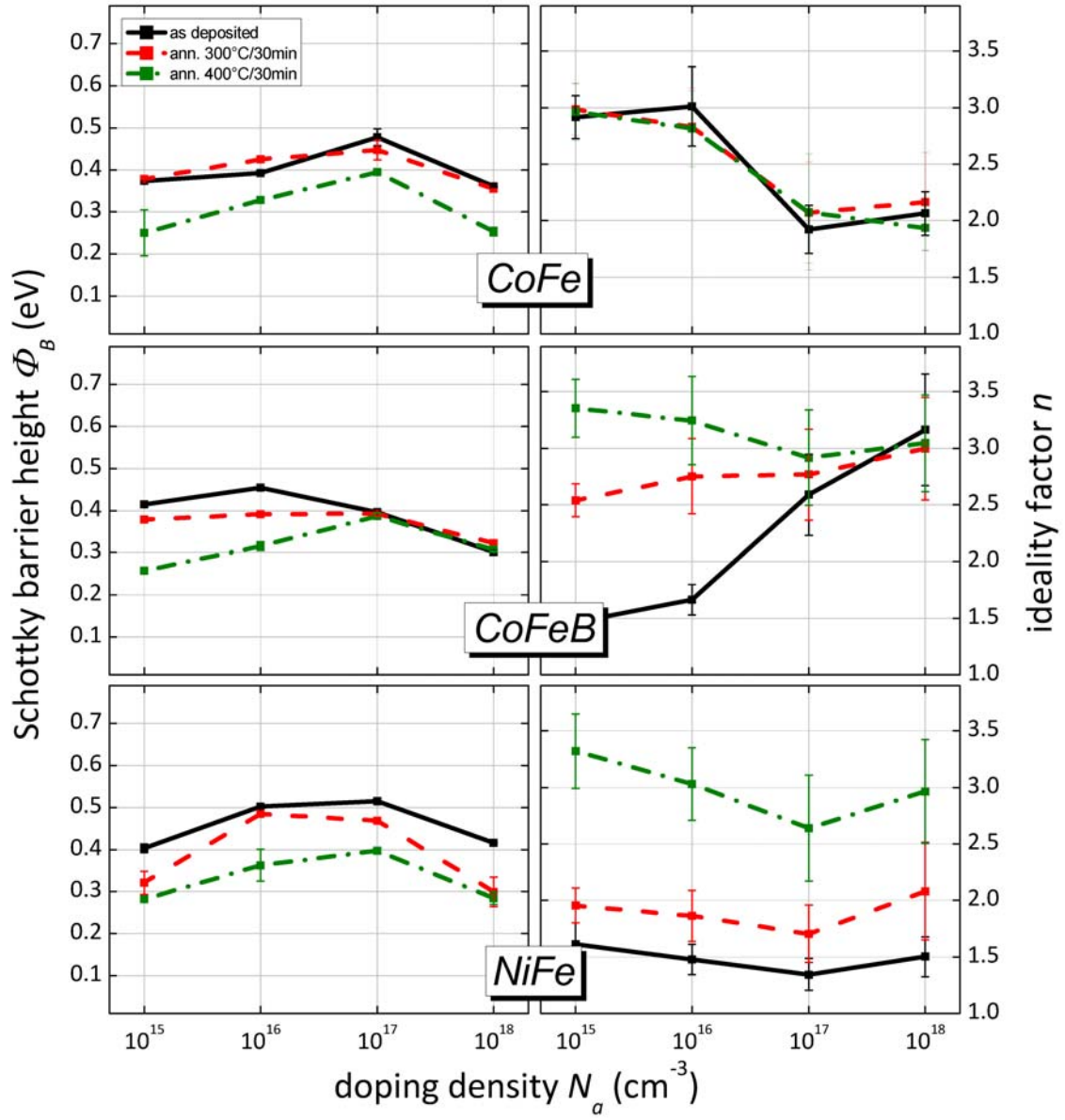


Figure 3.19: Plots of the average SBH and ideality factor for different FM electrodes over the doping density, for the as-deposited diodes (black full), annealed at 300°C (red dashed) and 400°C (green chain) at a reverse bias of 0.2 V.

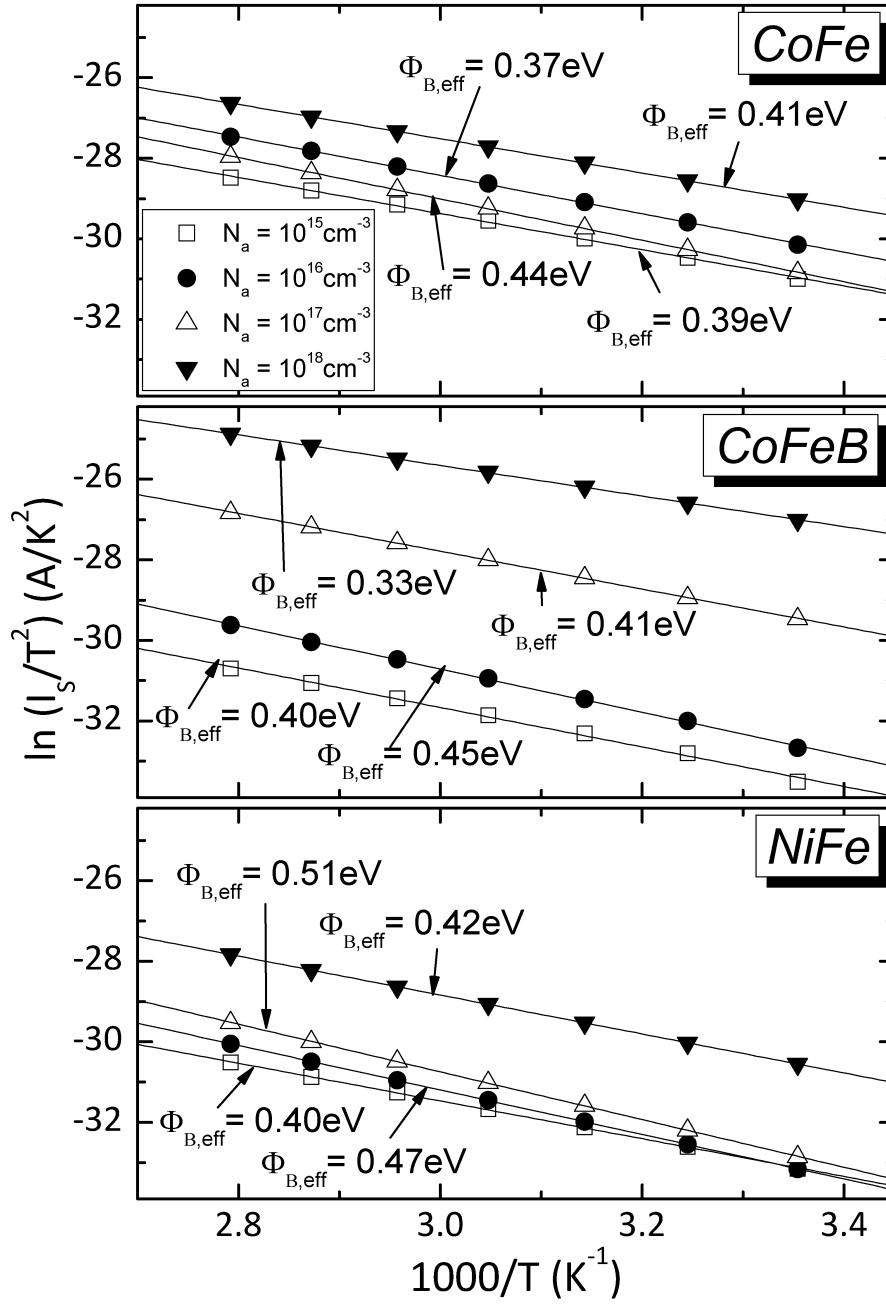


Figure 3.20: Arrhenius plots of the saturation current $\ln(I_s/T^2)$ versus $1/T$ for 10^{15} cm^{-3} doped n-Si with CoFe (top), CoFeB (middle) and NiFe (bottom). The effective barrier height $\Phi_{B,eff}$, corresponding to the slope of the linear fit, is depicted for the as-deposited case (open square), annealed at 300° C (full circle) and 400° C (open triangle) at a reverse bias of 0.2 V .

3.6.2 Ferromagnetic p-Si MIS tunneling diodes

The inclusion of the MgO insulating layer controls through its characteristics (thickness, height, carrier effective masses) the transmission probabilities of the majority and minority tunnel currents [6, 22, 11]. The JVs of all different investigated MIS diodes presented on the left in Fig.3.21 and Fig.3.22 are compatible to what is expected from minority carrier-dominated devices [22]. The observations supporting this, are: (i) J_r increases with decreasing N_a , contrary to the Schottky diodes. This agrees with the enhanced minority carrier generation for low doping densities, related with an extended depletion region. (ii) J_r is independent of the barrier thickness. This indicates that the semiconductor can generate some maximum amount of minority carrier current, which is a characteristic of the semiconductor alone. The generation current at reverse bias is proportional to the intrinsic carrier concentration, n_i , in the semiconductor. This should lead to a thermal activation energy, E_a , equal to half of the silicon's band gap, i.e. approx. 0.6 eV. The activation energy E_a can be extracted from Arrhenius plots of $\ln(J_r/T^2)$ versus $1/kT$, according to the formula $J_r \propto T^2 \exp(-E_a/kT)$. In Fig.3.23 such plots are shown for as-deposited MIS diodes with 1.5 nm MgO as a function of FM and N_a . The experimentally extracted E_a -values are shown on the right of Fig.3.21 and Fig.3.22 for 1.5 nm and 2.5 nm MgO as a function of N_a and T_A , respectively, for a reverse bias of $V_m = 1.0V$ for both MgO thicknesses. In Fig.3.24 the reverse bias dependent activation energy for a CoFeB MIS is presented, giving E_a -values between 0.5 and 0.7 eV for the largest part of the applied values and for all doping densities $N_a \geq 10^{16} \text{cm}^{-3}$. The activation energy for $N_a = 10^{15} \text{cm}^{-3}$ is already very low at low reverse-bias and further drops to nearly zero at larger bias. The current is therefore relatively temperature insensitive, varying approx. as T^2 . The reason for the vanishing E_a for the lowest doped MIS diodes is that at zero bias the silicon's interface is already inverted. Inversion results by the presence of positive charges in the MgO layer due to oxygen deficiency. Such a deficiency is anticipated for sputtered MgO in pure Ar atmosphere. The inverted Si interface provides a sufficient amount of minority carriers to support a large tunnel current through the oxide. Larger doping densities make the inversion of the silicon's interface increasingly difficult. The same trend of E_a as a function of the reverse bias, as presented for CoFeB MIS diodes in Fig. 3.24, applies for CoFe and NiFe.

Contrary to the reverse bias, the forward bias current for $t_{MgO} = 1.5 \text{ nm}$ is more than 1 order of magnitude higher than for the $t_{MgO} = 2.5 \text{ nm}$ case for all FMs, reflecting that not the semiconductor but the tunnel barrier is now limiting the current flow. At forward bias we expect that the dominant contribution arises from electron current from the metal to the silicon's conduction band.

At low forward bias the hump, marked in Fig.3.21 and 3.22 by arrows, denotes the transition from depletion to accumulation. It is clearly visible for $N_a = 10^{15} \text{cm}^{-3}$ and distinguishable for 10^{16}cm^{-3} . This feature is shifted to lower bias values when the MgO thickness is increased. From the magnitude of the shift, $\Delta V \approx 0.12V$, we can extract the fixed oxide charge density, Q_{ox} , using the relation: $\Delta V = Q_{ox}(1/C_1 - 1/C_2)$, where C_1 and C_2 are the capacitance of a 1.5 and

2.5nm MgO layer, respectively. Taking $\epsilon_r = 8.3$ [24] as the relative dielectric constant of MgO, we find that $Q_{ox} \approx 3 \times 10^{12} \text{ cm}^{-2}$.

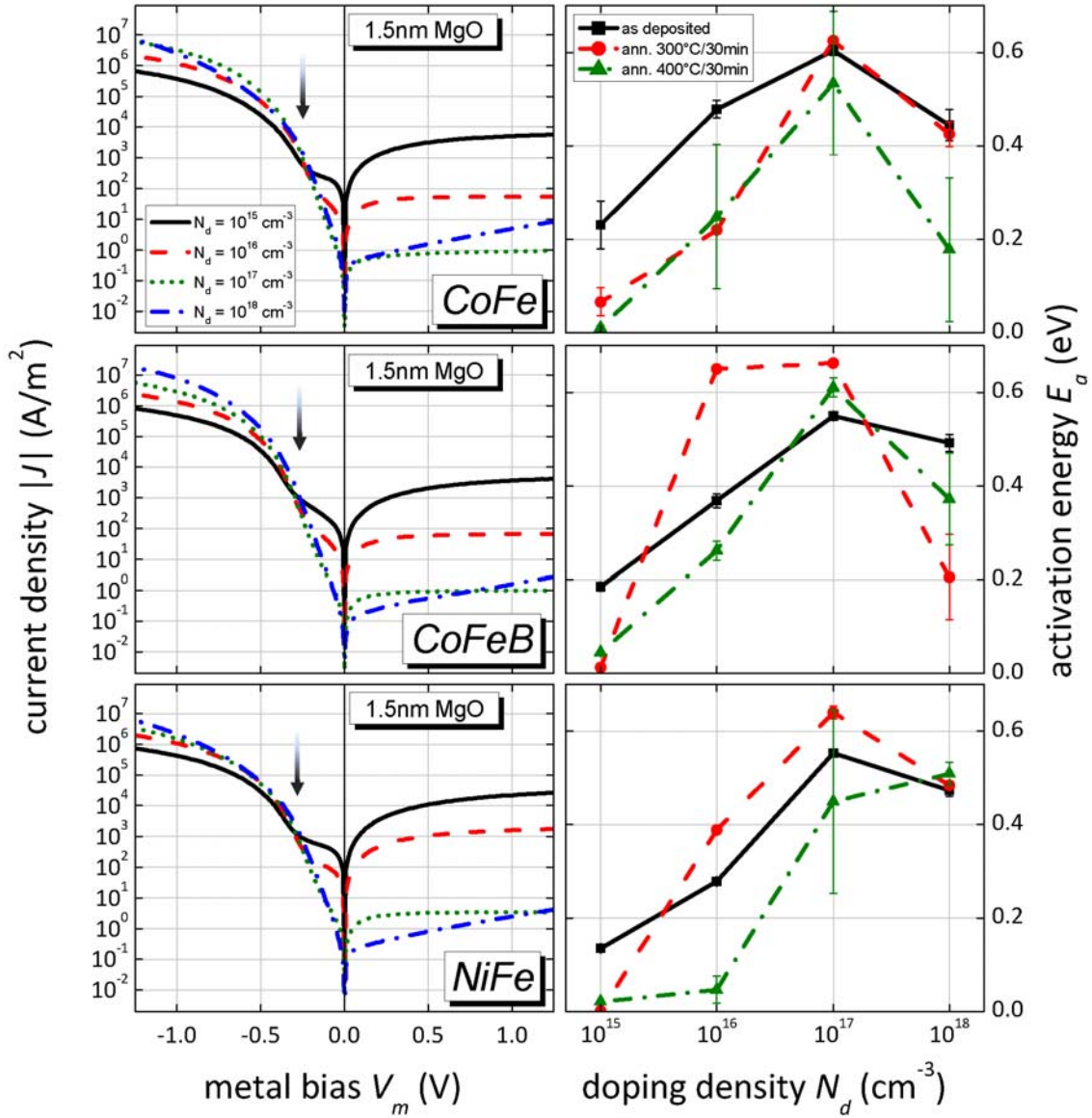


Figure 3.21: Room temperature IV measurements of as-deposited ferromagnetic MIS diodes with a 1.5 nm MgO tunneling barrier on p-Si(100) with four different doping densities of 10^{15} cm^{-3} (black full), 10^{16} cm^{-3} (red dashed), 10^{17} cm^{-3} (green dotted) and 10^{18} cm^{-3} (blue chain) for rectangular elements of $10 \times 15 \mu\text{m}^2$. The corresponding activation energy (right side) has been extracted from temperature dependent IV measurements at a static reverse voltage of 1.0 V for the as deposited case (black full), annealed at 300°C (red dashed) and 400°C (green chain) for 30min in Ar.

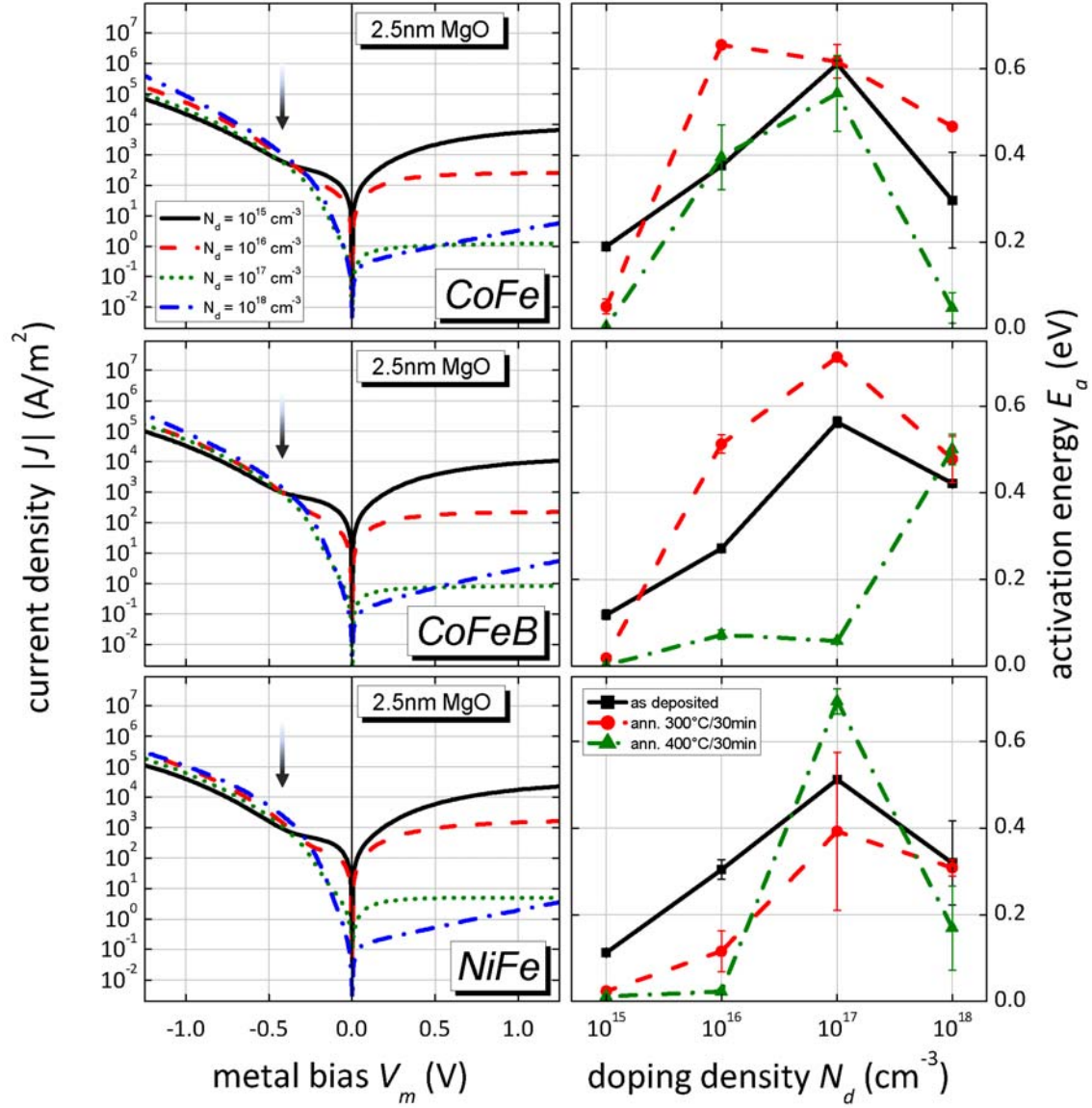


Figure 3.22: Room temperature IV measurements of as-deposited ferromagnetic MIS diodes with a 2.5 nm MgO tunneling barrier on p-Si(100) with four different doping densities of 10^{15} cm^{-3} (black full), 10^{16} cm^{-3} (red dashed), 10^{17} cm^{-3} (green dotted) and 10^{18} cm^{-3} (blue chain) for rectangular elements of $10 \times 15 \mu\text{m}^2$. The corresponding activation energy (right side) has been extracted from temperature dependent IV measurements at a static reverse voltage of 1.0 V for the as deposited case (black full), annealed at 300°C (red dashed) and 400°C (green chain) for 30min in Ar.

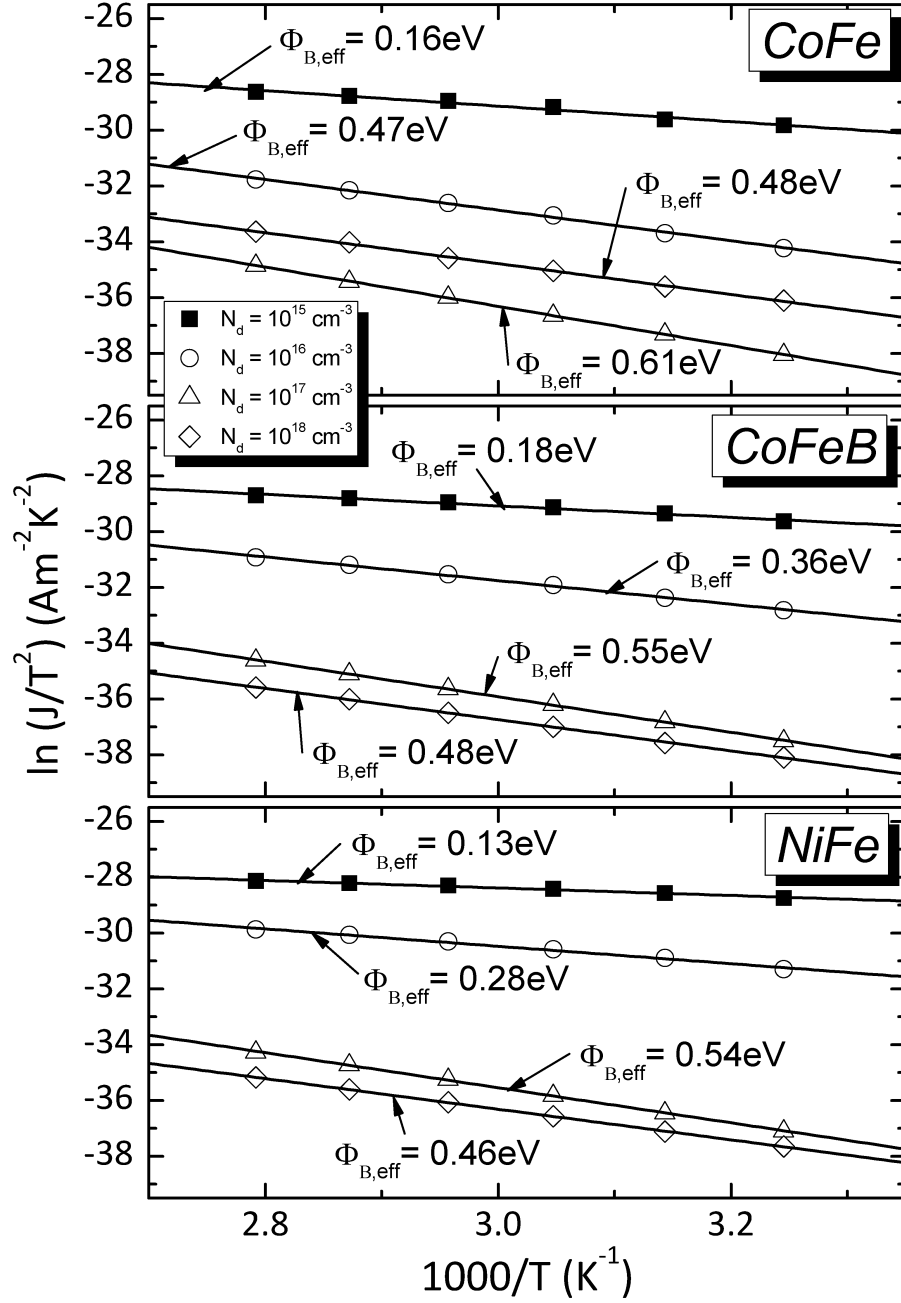


Figure 3.23: Arrhenius plots of the reverse current $\ln(I_R/T^2)$ versus $1/T$ at $-0.3V$ for a $1.5nm$ MgO tunneling barrier and $CoFe$ (top), $CoFeB$ (middle) and $NiFe$ (bottom) as a ferromagnetic electrode. Linear fit of the barrier height at different doping densities of $10^{15}cm^{-3}$ (fillsquare), $10^{16}cm^{-3}$ (opencircle), $10^{17}cm^{-3}$ (opentriangle) and $10^{18}cm^{-3}$ (opendiamond) for the as deposited case of $10 \times 15 \mu m^2$ rectangular junctions.

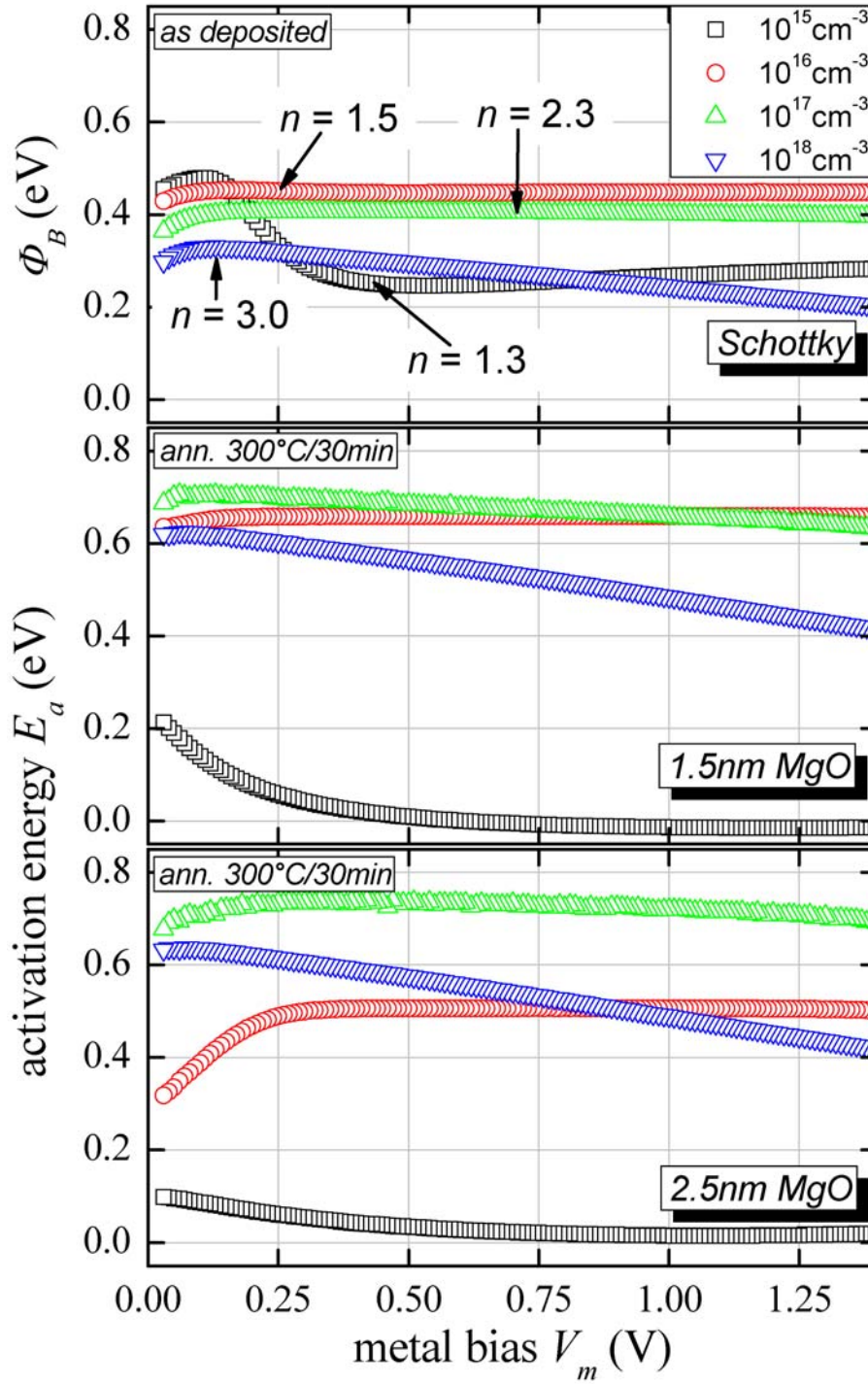


Figure 3.24: Schottky barrier height ϕ_B for p-Si/CoFeB/Ta/Au Schottky diodes and activation energy of p-Si/MgO/CoFeB/Ta/Au MIS diodes with varying MgO thickness and acceptor doping density from 10^{15} to 10^{18} cm^{-3}

3.7 Discussion

According to the conductivity mismatch theory, presented in Section 1.1.4, the resistance-area product window for a measurable magneto-current effect is determined by Eq. 1.31. For silicon with a doping density $N_D = 10^{15} \text{cm}^{-3}$, a corresponding resistivity $\rho_n = 4 \times 10^{-2} \Omega \text{m}$ and a spin relaxation time $\tau_{sf} = 7 \text{ ns}$ [16], the spin-flip length at $T = 300 \text{ K}$ can be calculated, using Eq. 1.27, to a spin diffusion length $l_{sf} = 3.5 \mu\text{m}$. Using this calculated value and a channel length, $t_n = 1 \mu\text{m}$, the RA product has to be within the range:

$$4.6 \times 10^{-8} \Omega \text{m}^2 < RA < 5.7 \times 10^{-7} \Omega \text{m}^2. \quad (3.16)$$

As shown in Section 3.5, n-Si Schottky diodes are characterized by a very low reverse bias current, which corresponds to electron injection. The obtained RA product is 6-7 orders of magnitude higher than the requested values. They are in this sense not appropriate for spin injectors. The inclusion of MgO leads to a significant increase of the reverse bias current, which is accompanied by a remarkable lowering of the effective Schottky barrier height (SBH) for electrons. The latter is partly attributed to the presence of positive oxide charges. In this aspect, they can be considered favorable for a spin injection experiment. On the other hand, the increased density of interface traps, which also may contribute to the low effective SBH is expected to have a detrimental effect on the electron spin polarization due to the long trap capture/emission times relative to the spin relaxation time. Despite the significant reverse current increase for the MgO-employing diodes, the obtained RA values are still 2-3 orders of magnitude too high (Fig. 3.25) for a channel length of $t_n = 1 \mu\text{m}$ and 1-2 orders of magnitude for $t_n = 100 \text{ nm}$. The forward bias that is related to spin detection is characterized by much higher current densities, which approach the requested regime especially for low doping densities (Fig. 3.25).

The problem of high contact resistance for injection could be circumvented by the use of a p-doped region under the injector FM contact, operated at forward bias. In this case of the p-Si diodes, the RA product, determining the magneto-current effect, is calculated the same way as for n-Si. The l_{sf} -value in p-Si is estimated to be the same as in the n-Si case, namely $3.5 \mu\text{m}$ for $N_a = 10^{15} \text{cm}^{-3}$, as literature values are lacking. It should be pointed out, that this leads to a rather optimistic RA range. By increased spin scattering in the case of p-Si the actual range would be narrower and, furthermore, the upper RA threshold value would be decreased.

The pronounced material diffusion in p-Si Schottky diodes, together with their majority transport characteristic, diminishes their suitability for spin injection contacts. In contrast, for MIS diodes, minority carriers dominate the transport characteristic. The spin diffusion length of holes in p-Si is considerably lower than the one for electrons, as described earlier in 1.1.2. For this reason, only MIS diodes are considered as injection/detection contacts to p-Si in the following. In Fig. 3.26 the RA values of CoFe p-Si MIS diodes are shown for forward (-1.0 V) and reverse bias (1.0 V) as a function of N_a and t_{MgO} . CoFe is chosen as one representative FM, while the

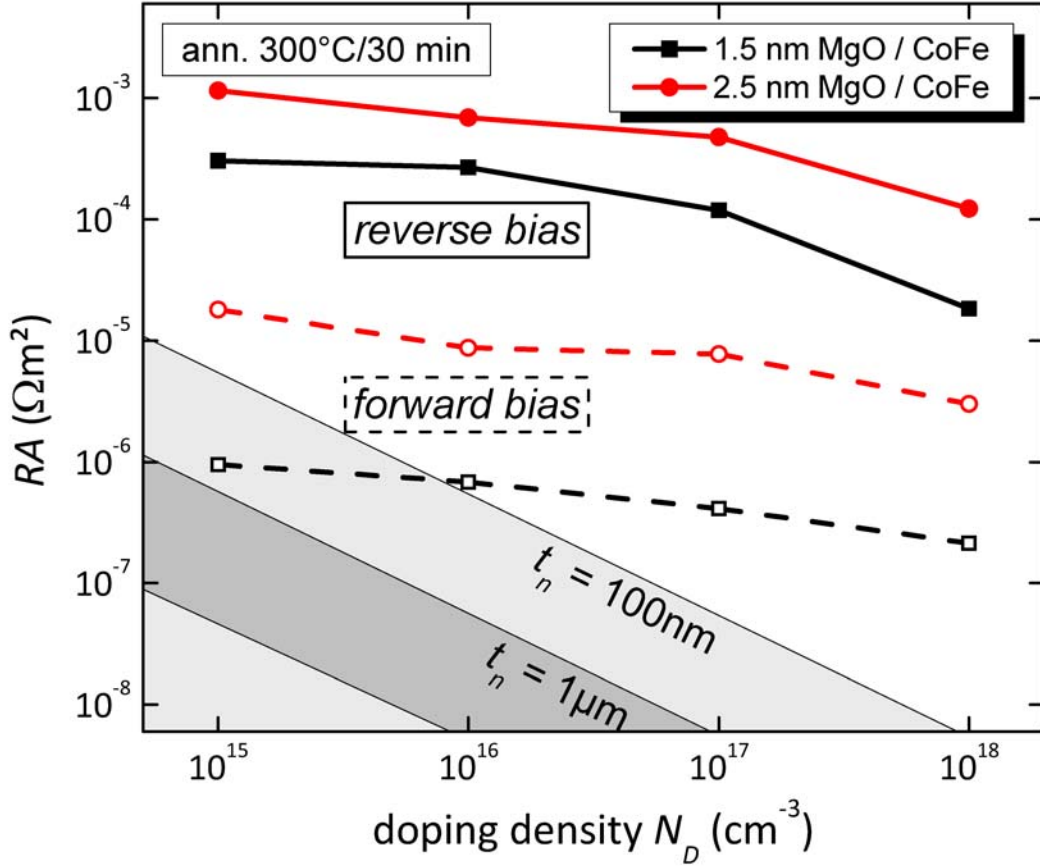


Figure 3.25: Measured resistance area values, RA_m , for n-Si FMIS diodes with CoFe electrodes, annealed at 300°C for 30min in Ar. The RA_m values have been extracted from RT IV measurements at a reverse bias of -1.0 V (full) and a forward bias of 1.0 V (dashed), for CoFe based MIS diodes with a MgO barrier thickness of 1.5 nm (black) and 2.5 nm (red). The needed RA in order to observe a measurable magnetocurrent (MC) is illustrated for two different channel length, t_n of 100 nm (light grey) and 1 μm (dark grey).

same arguments and approximate values apply for CoFeB and NiFe. Indeed, for $N_a = 10^{15}\text{cm}^{-3}$ the reverse bias RA values almost strike the required range, especially for $t_{\text{MgO}} = 1.5\text{ nm}$. For these diodes, the generation of an inversion layer close to the MgO/Si interface results in an activation energy close to zero. One might argue that the trap states inside the MgO, causing this inversion, have a detrimental effect on the spin polarization. However, also for TMR junction incorporating a MgO tunneling barrier, the non-stoichiometry and therefore trap states are shown not to impact the spin polarization during tunneling where the electron-trap interaction time is too short to cause spin scattering [35]. As a result, such MIS diodes on 10^{15}cm^{-3} doped p-Si can be considered favorable for a spin injection experiment. For forward bias the RA value even fulfils the requirement for $t_n = 100\text{ nm}$. In contrast, for larger N_a the extracted RA -values increase, while on the other hand the targeted RA range decreases, resulting in a gain of the conductance mismatch.

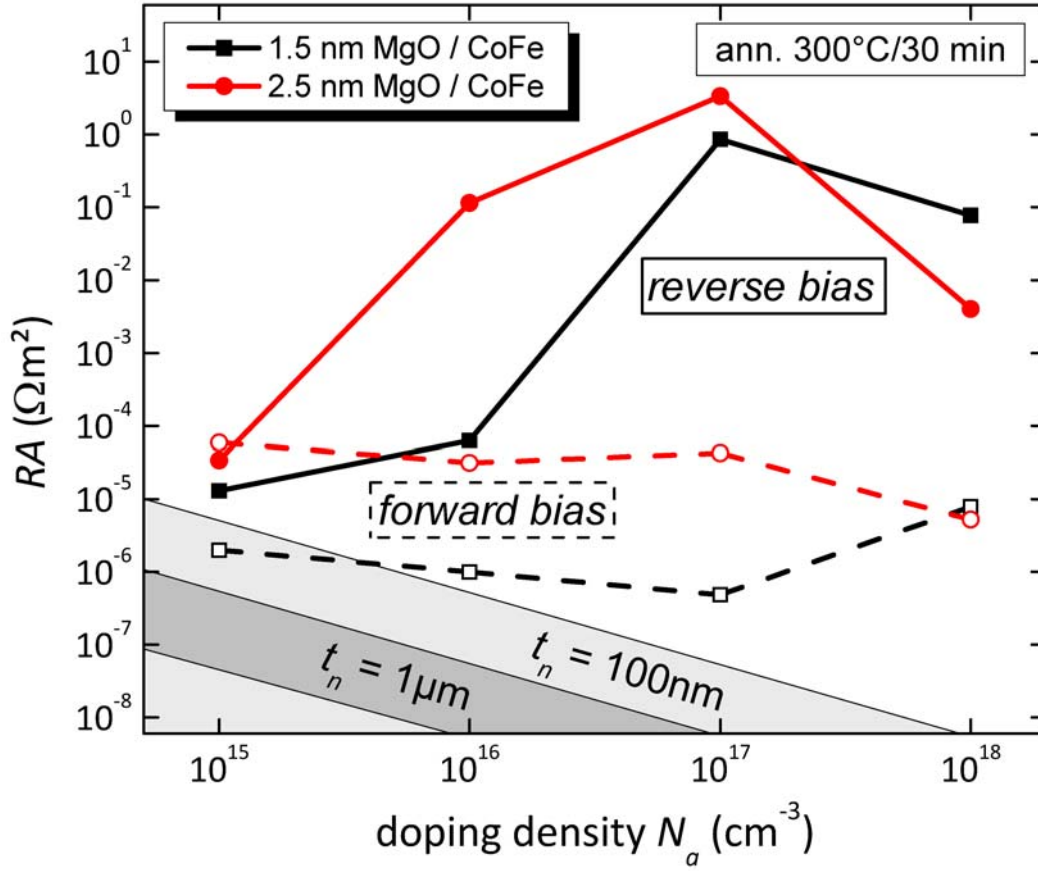


Figure 3.26: Measured resistance area values, RA_m , for p-Si MIS diodes with CoFe electrodes, annealed at 300°C for 30 min in Ar. The RA_m values have been extracted from RT IV measurements at a reverse bias of -1.0 V (full) and a forward bias of 1.0 V (dashed), for CoFe based MIS diodes with a MgO barrier thickness of 1.5 nm (black) and 2.5 nm (red). The needed RA in order to observe a measurable magneto current (MC) is illustrated for two different channel length, t_n of 100 nm (light grey) and 1 μ m (dark grey).

Measurement of the interface trap density of embedded diodes

Besides oxide traps incorporated in MgO, the interface trap density, D_{it} , is shown to influence the transport characteristic of the investigated diodes [11]. The samples used for this investigation feature a MgO thickness of 3 nm, which is found to be large enough to enable capacitance measurements, with 2 nm CoFe as FM electrode capped with TaN on n- and p-doped silicon with a doping density of 10^{15}cm^{-3} . Furthermore, the diodes have been embedded in 700 nm thick SiO_2 , reducing the parasitic capacitance effect of the contact pads to a minimum. The interface trap density was calculated using admittance spectra (G_p/ω vs. ω) measurements. This

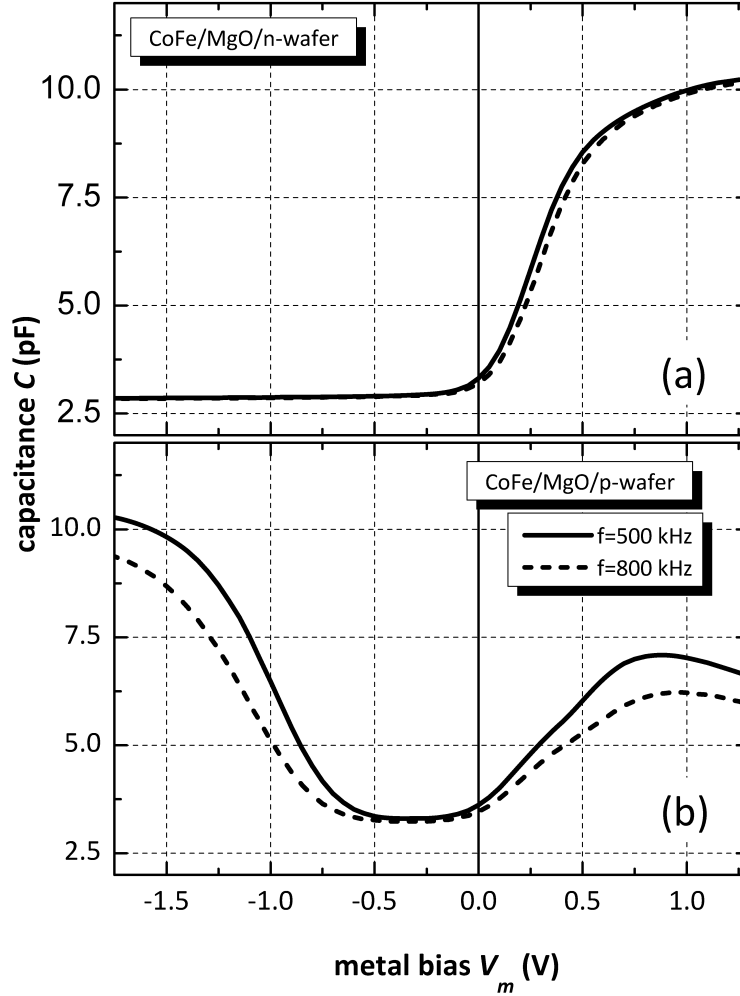


Figure 3.27: High-frequency CV-characteristics of a $400 \mu\text{m}^2$ CoFe/MgO/Si MIS diode at different frequencies.

so called conductance technique has been shown to be accurate even for diodes with ultrathin oxides and thus remarkable leakage current [36, 5, 6, 37]. The measured values have been accounted for the leakage of the oxide by correction of the measured capacitance and conductance with the series resistance. These corrections are discussed in detail in the next chapter. Fig.3.27(a) depicts the C-V characteristic of a $400 \mu\text{m}^2$ large MIS-capacitor for the CoFe/MgO stack on n-doped silicon at frequencies of 500 and 800 kHz. At zero applied bias the semiconductor is at depletion state as illustrated at the high frequency C-V characteristics. For accumulation, which corresponds to positive gate voltage, an oxide capacitance of 10.2 pF can be directly extracted from experimental measurements at 800 kHz. For p-doped Si, though, the creation of an inversion layer is shown to determine mostly the reverse bias current. This is in agreement with the presented C-V curves, where the inversion plateau is missing for reverse bias even at the frequency of 800 kHz.

Fig. 3.28 shows the D_{it} versus applied bias for the CoFe/MgO stack on the n-doped wafer. The relatively high D_{it} in the order of $8 \cdot 10^{13} \text{ cm}^{-2} \text{ eV}^{-1}$ may be related to

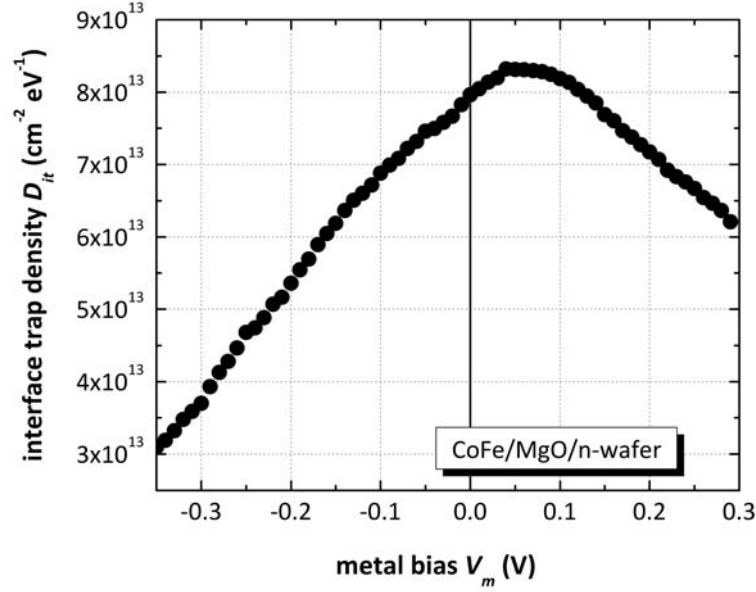


Figure 3.28: Interface trap density D_{it} versus gate bias of a $400\mu\text{m}^2$ CoFe/MgO/n-Si MIS diode, extracted from the maxima of the corrected G_p/ω distributions.

the sputter deposition technique for the growth of the tunnel barrier or the pre-deposition HF-etching of the native SiO_2 . Comparable D_{it} values were found for the p-wafer. The high trap density can also account for a pronounced contribution of trap assisted tunneling to the transport characteristics of the devices. Besides, the high interface trap density, D_{it} , constitutes an additional spin relaxation mechanism, that could diminish the spin injection and detection efficiency.

3.8 Magnetic characterization

Table 3.2: Description of the fabricated diode systems for the magnetic characterization (thickness in nm and composition in at%)

Sample	Multilayer (nominal thickness in nm)
Sample A	Si/MgO(2.5)/Co ₄₀ Fe ₄₀ B ₁₀ (10)/Ta(5)/Au(10)
Sample B	Si/MgO(2.5)/Ni ₈₀ Fe ₂₀ (10)/Ta(5)/Au(10)
Sample C	Si/MgO(1.5)/Co ₇₀ Fe ₃₀ (1)/Ni ₈₀ Fe ₂₀ (4)/Ta(5)
Series D	Si/MgO(x)/Co ₇₀ Fe ₃₀ (2)/Ni ₈₀ Fe ₂₀ (8)/Ta(5)/Au(10), x=0, 0.5, 1.0, 1.5, 2.5

For the magnetic investigation, samples elaborating different ferromagnets and different MgO tunneling barrier thicknesses have been fabricated and given in Table 3.2. The same processing steps were applied as stretched out in section 3.2. Samples A and B comprise CoFeB and NiFe with a respective nominal thickness of 10

nm. Sample C employs a CoFe/NiFe bilayer with thicknesses of 1 nm and 4 nm, respectively, while the same bilayer stack with increased thickness as a function of the MgO tunneling barrier thickness is examined in Series D. Each of the samples features arrays of identical sized contacts, arranged as presented in Fig. 3.3 and 3.4. As already discussed in Section 3.5, the contact sizes were increased during the etching processes for sample preparation by approximately 50 nm in each direction. Therefore, contacts with the width $w = 400, 500, 550$ and 600 nm and length $l = 3100$ and 1600 nm, result in eight different arrays with aspect ratios ranging from 7.75 and 2.67.

The magnetic properties of these contacts have been investigated using Magneto-optical Kerr effect (MOKE) and magnetic force microscopy (MFM) techniques. For the latter a 60 nm thick MgO dielectric layer has been deposited on the samples in order to decrease the magnetic interaction between the magnetic tip and the sample, which could alter its domain structure. For MFM scans, commercial magnetic low-moment tips have been used, still giving adequate magnetic contrast.

Fig. 3.29 shows easy-axis MOKE loops of the Samples A, B and D ($x = 2.5$ nm) for a constant element size of $400\text{nm} \times 3100\text{nm}$. All samples show low switching fields, a high remanence and almost square magnetic hysteresis loops. Sample C, containing NiFe, the MOKE loop shows a deviation from a ideal square loop switching, more precisely the magnetic switching takes place through multiple intermediate states. Such kind of switching gives evidence to closed magnetic domains being formed, lowering the average spin polarization coming from such contacts. As a result, only diodes incorporating CoFe/NiFe and CoFeB are further considered in the following.

Another important parameter, that can be extracted from the MOKE magnetization loops, is the switching field distribution ΔH_s . To extract this, the magnetization ($M - H$) loops are fitted with the error function $y(x) = A + B \cdot \text{erf} \frac{x-x_0}{dx}$, using the assumption of a square like switching characteristic of individual elements, as well as a symmetric switching distribution. The derivative of the error-function is a Gaussian distribution, where H_s is the distribution's mean-value and ΔH_s is twice the standard deviation, σ ($\Delta H_s = 2\sigma$).

Figures 3.30(a) and (b) show easy-axis MOKE loops for contacts of 3100 nm length and varying widths for different thicknesses of the CoFe/NiFe bilayer system, deposited on 1.5 nm MgO (Sample C and Series D, $x = 1.5$ nm). Fig. 3.30(c) and (d) present H_s and ΔH_s values for all arrays. As expected, the switching field is directly correlated to the magnetic layer thickness, where H_s is halved for half the magnetic layer thickness [38]. ΔH_s gives the same trend, decreasing with lower ferromagnetic thickness. Furthermore, H_s strongly depends on the width of the contacts, following a $1/w$ dependence [39, 40]. For the case of a thicker ferromagnetic electrode the width-dependence is a little more pronounced. For instance, H_s changes by 43%, comparing $1600\text{nm} \times 600\text{nm}$ sized elements and $1600\text{nm} \times 400\text{nm}$ ones. Increasing the FM thickness changes the difference in H_s to 47%, for the same element sizes. Such small variation for different FM thicknesses can be attributed to slight changes in edge definition and contact shape.

In general, end domains are considered to play the most important role for the magnetic switching process of such kind of structures. Small magnetic end domains have

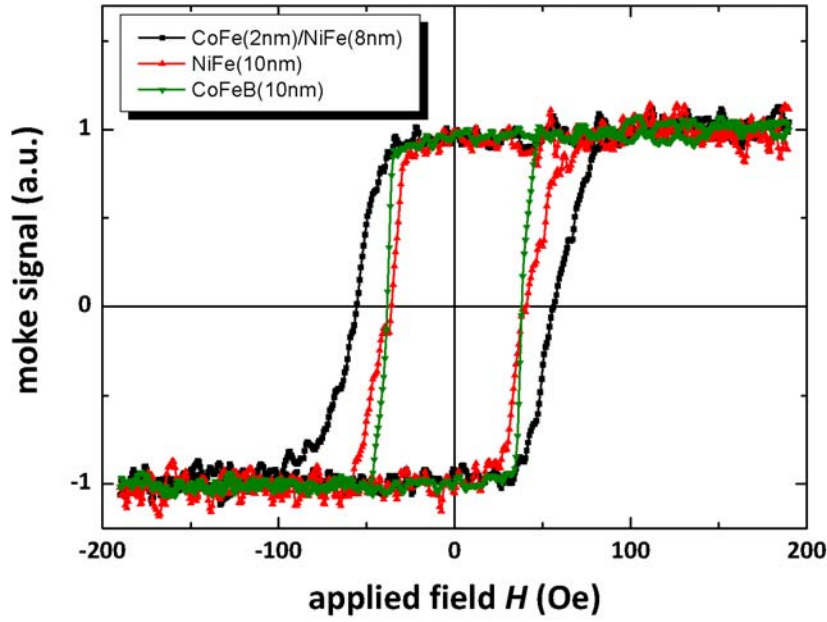


Figure 3.29: Easy-axis MOKE measurements of MIS diodes incorporating 2.5 nm MgO with different ferromagnetic electrodes, recorded for a constant element size $400\text{nm} \times 3100\text{nm}$.

been shown to form in the blunted elements' edges, propagating along the element with increasing reverse magnetic field, reversing the elements' magnetization. Due to higher magnetostatic energy in smaller contacts, the formation of end domains is more difficult to accomplish, leading to an increased H_s . Additionally, the dependence of H_s on the elements' length is increasing for larger widths. This indicates an increasing dependence of the switching process on the element's body magnetization. However, ΔH_s shows low variation as a function of the elements' width, while the switching distribution is in general larger for the thicker FM layer and shorter contacts with $l = 1600$ nm. As a result, increasing the FM layer thickness is increasing H_s but on the same time the magnetic selectivity, defined as the switching field difference from contacts with different widths.

Another interesting aspect is the dependence of the magnetic switching characteristics from the MgO tunneling barrier thickness. In Fig. 3.31(a) and (b) easy axis $M - H$ loops from Series D are depicted, for contact sizes of $1600\text{nm} \times 500\text{nm}$ and $3100\text{nm} \times 400\text{nm}$, respectively. The results for H_s and ΔH_s as a function of the MgO thickness are summarized in Fig. 3.31(c) to (f) for arrays with both lengths of 3100 nm and 1600 nm. Schottky diodes ($x = 0$) feature the lowest switching field. For the inclusion of a tunneling barrier H_s increases for all arrays up to $x = 1.5$ nm. Further increase of the MgO thickness up to $x = 2.5$ nm shows a different tendency as a function of the contact width. For the smaller widths a slight decrease of H_s is observed, whereas for larger widths H_s is further increasing. The origin of this width dependent behavior is not clear. However, no structural inhomogeneities have been observed that could explain this. ΔH_s is increasing with the MgO thickness, a

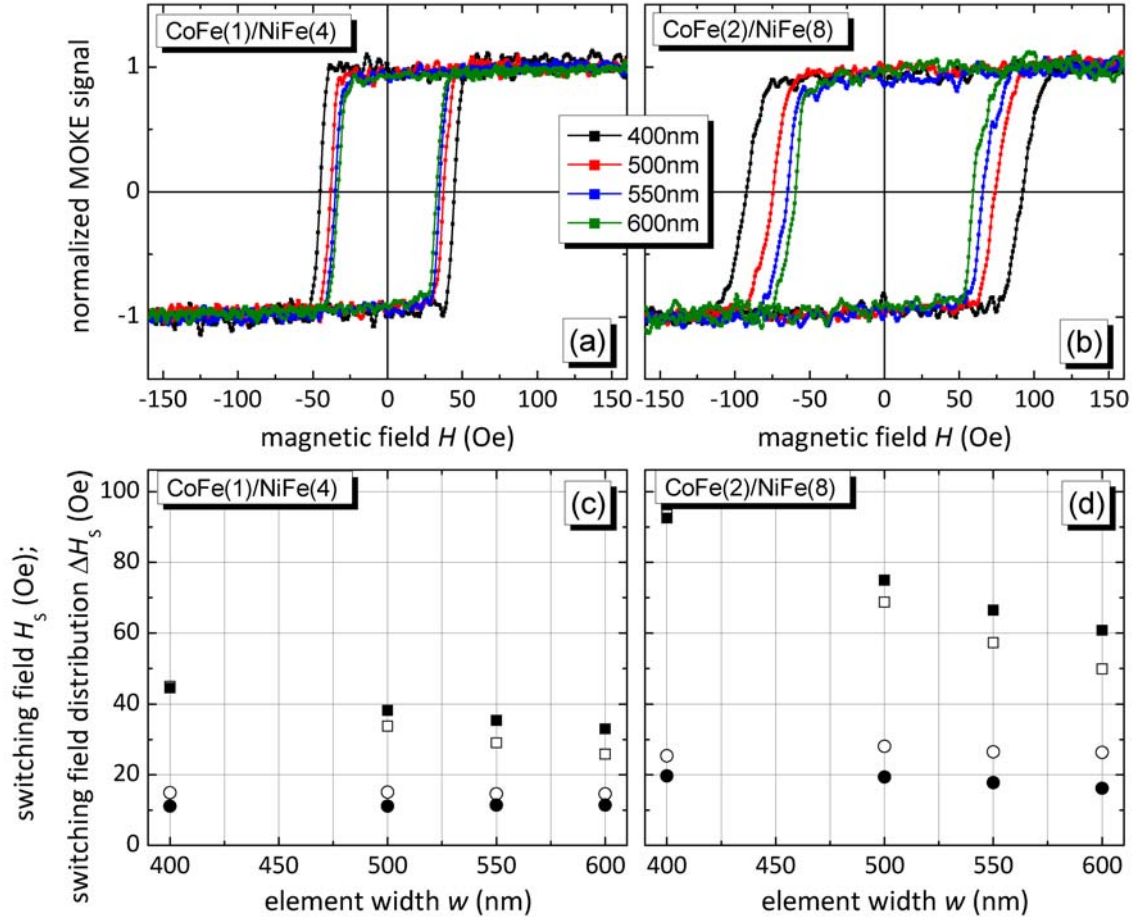


Figure 3.30: (a) and (b) easy-axis MOKE loops for $l=3100\text{nm}$ contacts with different thickness of the CoFe/NiFe bilayer system both with 1.5 nm MgO tunneling barrier. (c) and (d) Switching field H_s (squares) and switching field distribution ΔH_s (circles) as a function of the element width for lengths of 3100nm (full) and 1600nm (empty)

character that is possibly related to increasing roughness of the MgO/FM interface. Clear magnetic selectivity is observed for all MgO thicknesses, however the lowest selectivity is observed for $x = 2.5$ nm. The remanent magnetization is high for all arrays and not changing with the MgO thickness.

For CoFeB-based contacts (Sample A) the same general switching characteristic is obtained, shown in Fig. 3.32. In contrast to CoFe/NiFe contacts where the film structure is polycrystalline, CoFeB is amorphous in the as deposited state. Despite both ferromagnets have approximately the same magnetic net moment, the switching field of CoFeB is approximately half the H_s for CoFe/NiFe (Series D, $x = 2.5$ nm). Also the switching field distribution is approximately half. This feature can be attributed to vanishing magneto-crystalline anisotropy in the case of amorphous CoFeB. Since the concept of a spinFET features the front-end implementation of the magnetic contacts, demanding a thermal stability of at least 400°C. Therefore both of these promising contact structures, CoFe/NiFe and CoFeB, have been studied af-

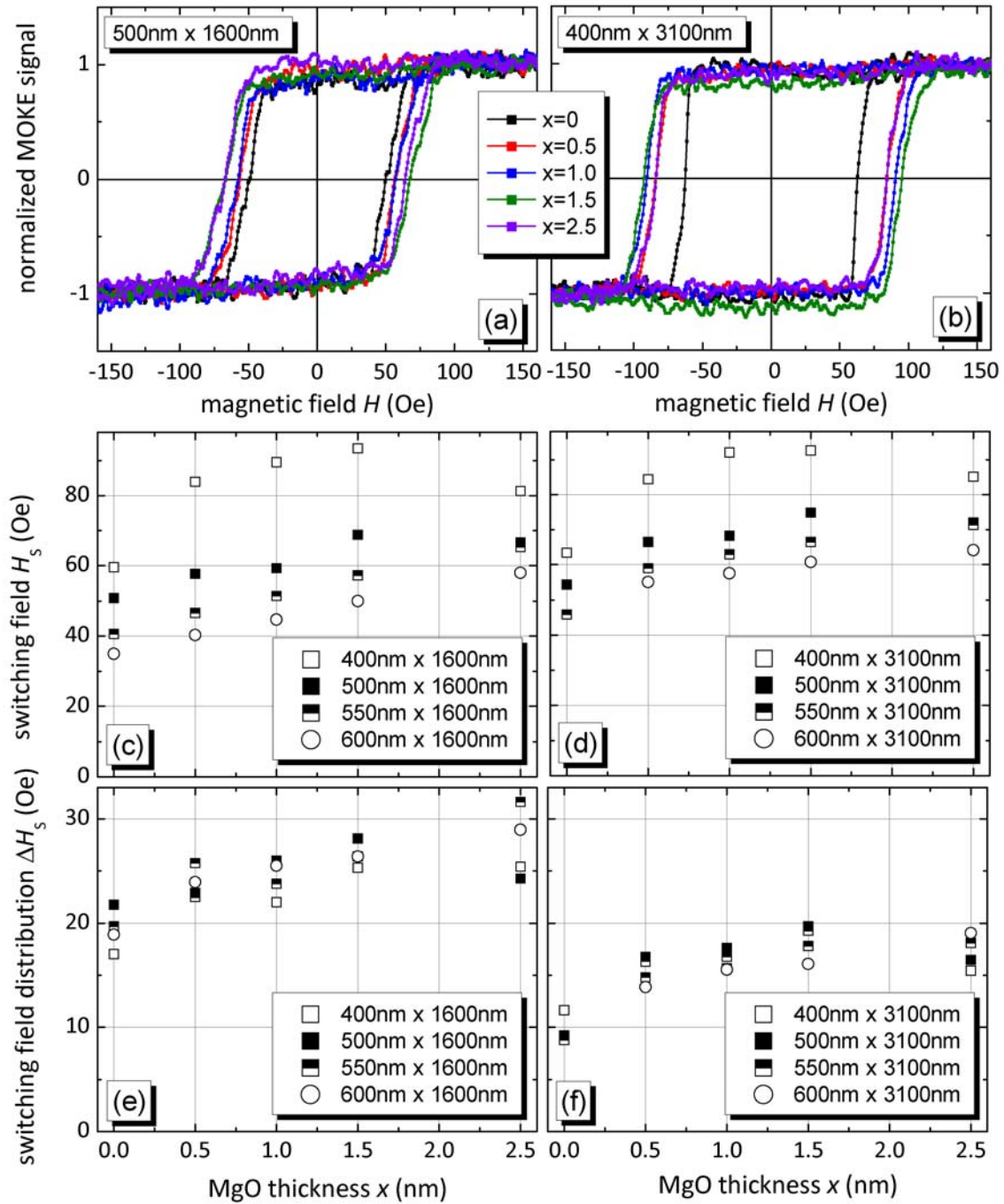


Figure 3.31: (a) and (b) easy axis MOKE loops of CoFe/NiFe contacts as a function of the MgO thickness. (c)-(f) Switching field H_s and switching field distribution ΔH_s as a function of the MgO thickness

ter an annealing in a vacuum oven system. In Fig. 3.33 the magnetic switching loops 400nm×3100nm contacts for CoFe/NiFe (Series D, $x = 2.5$ nm) and CoFeB (Sample A) samples are shown in the as deposited and after an annealing of 400°C and 500°C for 30 min. Both samples have reproducible switching for an annealing up to

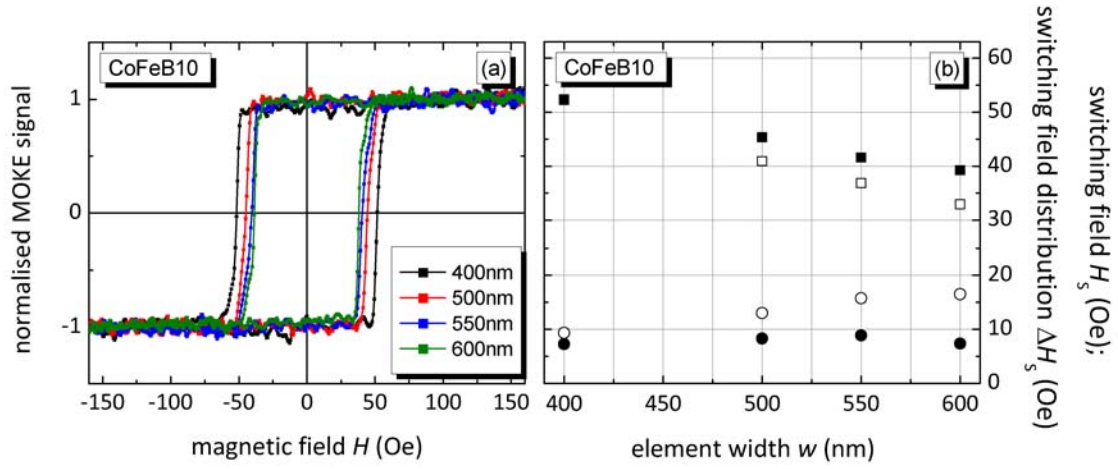


Figure 3.32: (a) Easy axis MOKE loops for contact with amorphous CoFeB (Sample B). (b) Switching field (squares) and switching field distribution (circles) as a function of the contact width for element lengths of 3100 nm (filled points) and 1600 nm (empty points)

400°C. However, for annealing at 500°C the H_s of CoFeB is dramatically increased, related to an extensive film crystallization, as shown in Section 3.5. In comparison, the switching of the CoFe/NiFe bilayer is a lot less altered with annealing. In conclusion, the switching characteristics of CoFeB for annealing up to 400°C is highly suited for a spinFET, coming with the drawback of poor thermal stability for higher temperature treatment.

After studying the magnetic characteristics of discrete diodes by means of MOKE measurements, the magnetic properties for different injector/detector pairs of Sample C are investigated. While MOKE is recording the magnetic information of a large

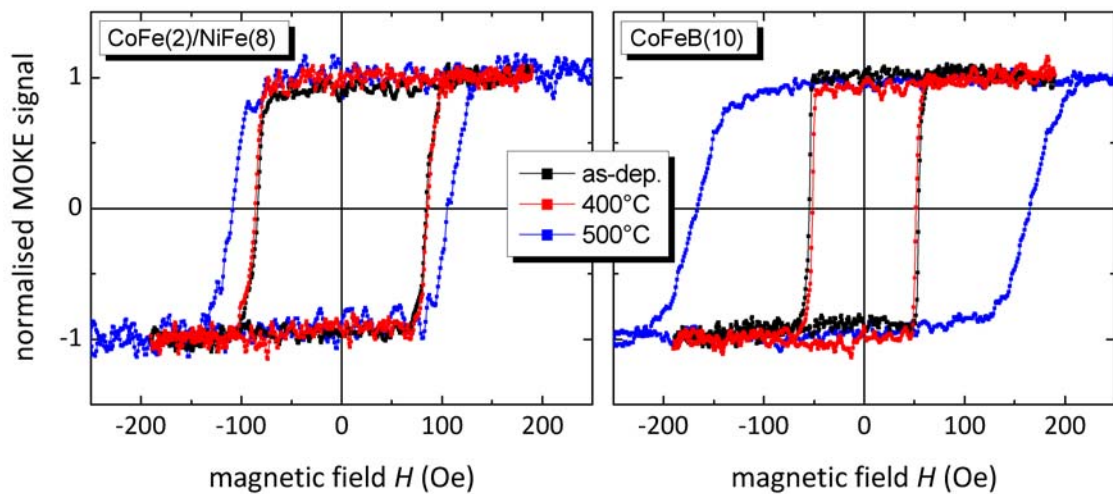


Figure 3.33: MOKE loops for 400nm x 3100nm contacts with CoFe/NiFe and CoFeB ferromagnets for different annealing states

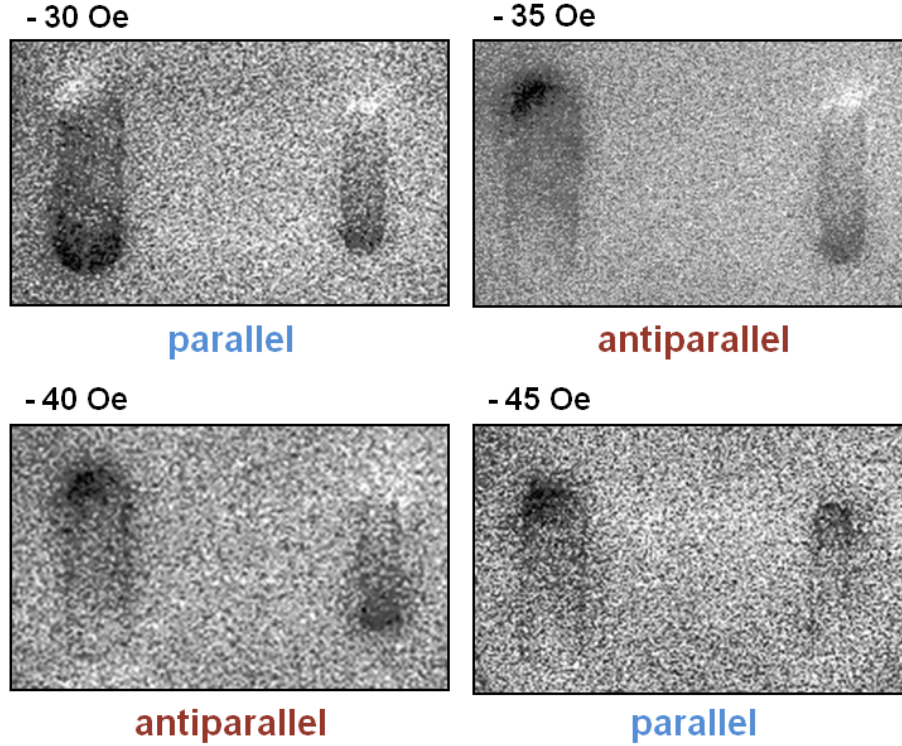


Figure 3.34: MFM images of injector/detector pairs of Sample C showing different alignment states as a function of the magnetic field

ensemble of contacts, with the aid of MFM also isolated injector/detector pairs can be studied. For each MFM scan, the sample has been saturated outside the microscope and subsequently increasing reverse magnetic fields in steps of 5 Oe have been applied. The MFM images have been recorded at remanence magnetization. In Fig. 3.34 a series of MFM images of Sample C is depicted for one injector/detector pair of $500\text{nm} \times 1800\text{nm}$ and $300\text{nm} \times 1500\text{nm}$. For $H = -35$ Oe both contacts are aligned in parallel, before the magnetization of the larger contact is reversing for $H = -40$ Oe. This antiparallel state is sustained for $H = -45$ Oe, while also the smaller contact is switched for $H = -50$ Oe. For this particular pair, a magnetic selectivity of at least 10 Oe is obtained, providing a large enough window for electrical measurements. The same experiment has been carried out for different injector/detector combinations, summarized in Table 3.3. For most of the combinations magnetic selectivity is observed with a comparable window in the range of 10 Oe. However, for one combination including a low aspect-ratio contact of $1000\text{nm} \times 1500\text{nm}$ a flux-closure state is obtained, where no distinct parallel or antiparallel state could be related to this state.

Table 3.3: Magnetic configurations of injector/detector pairs for Sample C as a function of the applied field

Field (Oe)	$1.0 \times 4.0\mu m^2 /$ $0.3 \times 3.0\mu m^2$	$0.5 \times 3.0\mu m^2 /$ $0.3 \times 2.5\mu m^2$	$0.5 \times 1.8\mu m^2 /$ $0.3 \times 1.5\mu m^2$	$1.0 \times 1.5\mu m^2 /$ $0.3 \times 1.5\mu m^2$
-25	P	P	P	close domain structure
-30	AP	P	P	
-35	AP	P	AP	
-30	AP	AP	AP	
-45	P	AP	AP	
-50	P	AP	P	
-55	P	P	P	

Conclusion - Magnetic characterization

The magnetic properties of different magnetic contact structures to silicon have been investigated. The contacts have blunted edges with varying aspect ratios. CoFe/NiFe bilayers, NiFe and CoFeB feature a low magnetic switching field, found to be suitable for the usage of injection/detection contacts in a spinFET. The remanence magnetization is generally high for these three ferromagnetic layers. The elements width is shown to be the determining factor for the switching field, where H_s is increasing with lower width, while the contact length has less impact. It is found that magnetic end-domains in the elements' blunted edges play the dominant role in the magnetization reversal process, which are more difficult to form for lower widths. The inclusion of a MgO tunneling barrier between silicon and the FM leads to an increase of the magnetic switching field as well as the switching field distribution. For annealing at temperatures higher than 400°C, CoFeB is extensively crystallized coming along with a dramatic increase in the switching field, while this is not the case for the polycrystalline CoFe/NiFe system. The magnetic selectivity of all investigated samples is large, making all the stack suitable for a spinFET device. Selective switching of single injector/detector pairs has been tested by means of MFM measurements for a CoFe/NiFe bilayer system, showing clear parallel and antiparallel states for most of the size combinations, where the aspect ratios is high enough.

3.9 Conclusion

In conclusion, the structural, electrical and magnetic transport properties of Schottky and MgO-based MIS diodes on n-Si(001) and p-Si(001) have been studied, as a function of the ferromagnetic electrode, tunneling barrier thickness, doping density and thermal annealing. The MgO barrier remains amorphous even after

annealing at 400°C. The reason for that is attributed to a combination of the thickness of the MgO layer (2.5 nm) and the large lattice mismatch between Si and cubic MgO. In case of the n-Si diodes, the SBH of as-deposited Schottky diodes is independent of the metal workfunction, with a magnitude of approx. 0.65 eV, while the rectification is highly pronounced. The diodes show moderate changes after annealing at 300°C. An annealing at 400°C changes the diode characteristics for CoFeB and NiFe considerably, especially for low N_d . CoFe Schottky diodes, on the other hand, present relatively high thermal stability. As-deposited MIS diodes have considerably lower effective SBH values, ranging from 0.2 to 0.3 eV as a function of N_d , independent of the ferromagnetic electrode and the MgO thickness. These are further lowered after annealing at 300°C and 400°C and reflect high reverse current densities and low rectification. The low effective SBH for MIS diodes is attributed to the relatively high fixed oxide charge density and interface traps. The obtained contact resistance values for the Schottky diodes are far too high for injection or detection, while for MIS diodes they are closer to the requested regime.

In the case of p-Si diodes, injection of spin-polarized carriers from the metal to the semiconductor takes place at forward bias in the case of ferromagnetic contacts to p-type silicon. For Schottky diodes the dominant current contribution flows to the valence band of the semiconductor, where spin relaxation takes place in the same time scale as momentum relaxation, leading to fast carrier depolarization [16]. At large forward bias, the electron current towards silicon's conduction band can be pronounced. Especially for large doping densities a high current density is achieved. Even in this case, the injection of electrons takes place at a hole-accumulated silicon interface, leading to spin dephasing due to electron-hole interaction. On the other hand, MIS diodes are dominated by minority carrier transport. Overall, high forward-bias current densities are achieved, almost independently of the doping density. Owing to the aforementioned inversion layer for the lowest doped diodes, considerable electron current from the metal to the silicon can be injected at relatively low forward bias, while the semiconductor's surface is still inverted or depleted of holes. This helps decreasing the electron-hole interaction arising from an otherwise accumulated interface and profiting from a higher spin polarization related with low injection voltages. Conclusively, the presence of the inversion layer for low-doped, p-type diodes can be exploited in order to create a contact with low resistance and a limited electron-hole interaction. For reverse-bias the presence of the inversion layer also acts as an adequate supply of minority carriers for electron detection.

The magnetic switching characteristics of CoFe/NiFe and CoFeB diodes are found to be suitable for spin injection and detection contacts to silicon. The inclusion of a MgO tunnel barrier between ferromagnet and semiconductor leads to an increase of the switching field and the switching field distribution of the contacts. The diodes show square-like switching, featuring a high remanence magnetization, where the switching field is defined more by the element's width than on their length. The domains in the elements' blunted edges originate the magnetization reversal. A large magnetic selectivity is achieved, enabling an approximately 10 Oe wide window of antiparallel magnetization for injector/detector pairs.

REFERENCES OF CHAPTER 3

- [1] Fork, D., Ponce, F., Tramontana, J., and Geballe, T. *Appl. Phys. Lett.* **58**, 2294 (1991).
- [2] Istratov, A. and Weber, E. *Appl. Phys. A* **66**, 123 (1998).
- [3] Istratov, A., Hieslmair, H., and Weber, E. *Appl. Phys. A* **69**, 13 (1999).
- [4] Weber, E. *Appl. Phys. A* **30**, 1 (1983).
- [5] Schroder, D. *Semiconductor Material and Device Characterization*. Wiley & Sons, 2nd edition edition, (1989).
- [6] Sze, S. M. *Physics of Semiconductor Devices*. John Wiley & Sons, second edition, (1981).
- [7] Xu, Y.-N. and Ching, W. Y. *Phys. Rev. B* **43** (1991).
- [8] Rashba, E. I. *Physical Review B* **62**(24), 16267 (2000).
- [9] Fert, A. and Jaffrès, H. *Physical Review B* **64**(18), 4420 (2001).
- [10] Schmidt, G., Ferrand, D., Molenkamp, L. W., Filip, A. T., and van Wees, B. J. *Physical Review B* **62**(8), 4790 (2000).
- [11] Uhrmann, T., Dimopoulos, T., Brückl, H., Lazarov, V. K., Kohn, A., Paschen, U., Bär, L., and Rührig, M. *Journal of Applied Physics* (2007).
- [12] Min, B. C., Lodder, J. C., Jansen, R., and Motohashi, K. *Journal of Applied Physics* **99**(08), 701 (2006).
- [13] Sugiura, K., Nakane, R., Sugahara, S., and Tanaka, M. *Applied Physics Letters* **89**(07), 2110–2112 (2006).
- [14] Min, B. C., Motohashi, K., Lodder, C., and Jansen, R. *Nature Materials* **5**, 817 (2006).
- [15] Kikkawa, J. M. and Awschalom, D. D. *Physical Review Letters* **80**(19), 4313–4316 May (1998).

-
- [16] Zutic, I., Fabian, J., and Sarma, S. D. *Review of Modern Physics* **76**, 323–410 (2004).
 - [17] Hudait, M. and Krupanidhi, S. *Physica B* **307**, 125 (2001).
 - [18] Mönch, W. *Phys. Rev. Lett.* **58**, 1260 (1987).
 - [19] Istratov, A., Zhang, P., McDonald, R., Smith, A., Seacrist, M., Moreland, J., Shen, J., Wahlich, R., and Weber, E. *J. Appl. Phys.* **97**, 023505 (2005).
 - [20] McHugo, S., McDonald, R., Smith, A., Hurley, D., and Weber, E. *Appl. Phys. Lett.* **73**, 1424 (1998).
 - [21] Lee, J., Uhrmann, T., Fidler, J., Dimopoulos, T., and Brückl, H. *Proceeding of 11th Joint MMM-Intermag Conference (to appear in J. Appl. Phys.)* (2010).
 - [22] Shewchun, J. and Green, M. A. *Journal of Applied Physics* **46**(12), 5179–5184 (1975).
 - [23] Temple, V. A. K., Green, M. A., and Shewchun, J. *Journal of Applied Physics* **45**(11), 4934–4943 (1974).
 - [24] Kohn, A., Kovacs, A., Uhrmann, T., Dimopoulos, T., and Brückl, H. *Appl. Phys. Lett.* , 042506 (2009).
 - [25] Norman, C. and Thomas, R. *Trans. on Nuclear Science* **2**, 933 (1977).
 - [26] Pulfrey, D. L. *IEEE Transactions on Electron Devices* **25**(11), 1308–1317 (1978).
 - [27] Wagner, L., Young, R., and Sugerman, A. *IEEE Electron Device Letters* **EDL-4**, 320 (1983).
 - [28] Verret, D. *IEEE Electron Device Letters* **EDL-5**, 142 (1984).
 - [29] Soylu, M. and Abay, B. *Microelectronic Engineering* **86** (2009).
 - [30] Guo, J., Feng, M., Guo, R., Pan, F., and Chang, C. *Appl. Phys. Lett.* **67**, 2657 (1995).
 - [31] Nakagomi, S., Spetz, A. L., Lundström, I., and Tobias, P. *IEEE Sensors Journal* **2**, 379 (2002).
 - [32] Uhrmann, T., Dimopoulos, T., Kovacs, A., Kohn, A., Weyers, S., Paschen, U., Smoliner, J., and Brückl, H. *Journal of Physics D: Applied Physics* **42**, 145114 (2009).
 - [33] Safarov, V. *french patent, No. W0 2004/061856 A2* (2004).
 - [34] Mönch, W. *J. Vac. Sci. Technol. B* **17**, 1867 (1999).

-
- [35] Yuasa, S. and Djayaprawira, D. D. *Journal of Physics D: Applied Physics* **40**, 337–354 (2007).
 - [36] Vogel, E. M., Henson, W. K., Richter, C. A., and Suehle, J. S. *IEEE Transactions on Electron Devices* **47**(3), 601 (2000).
 - [37] Nicollian, E. H. and Goetzberger, A. *IEEE Transactions on Electron Devices* **12**, 108–117 (1965).
 - [38] Kirk, K. J., Chapman, J. N., and Wilkinson, C. D. W. *Journal of Applied Physics* **85**(8), 5237–5242 (1999).
 - [39] Chou, S. *Journal of Applied Physics* **79**, 6101 (1996).
 - [40] Rührig, M., Khamsehpour, B., Kirk, K. J., Chapman, J. N., Aitchison, P., McVitie, S., and Wilkinson, C. D. W. *IEEE Transactions on Magnetics* **32**(5), 4452–4457 (1996).

CHAPTER 4

MGO-BASED MOS CAPACITORS

The beneficial impact of a crystalline MgO tunneling barrier on the spin injection efficiency has been underlined already. On the other hand, in the previous chapter we showed lack of crystallinity of the MgO layer sputtered directly on silicon and additionally large interface trap density, both of which strongly impact the electrical transport properties. This chapter discusses a possible solution for both issues, namely the growth of a thin SiO₂ layer previous to the MgO tunneling barrier. Metal-oxide-semiconductor (MOS) capacitors are used to characterize the structural and the electrical properties of the SiO₂/MgO dielectric bi-layer in comparison to MgO and SiO₂ dielectrics.

4.1 Introduction and scope

The formation of diodes with a low interface trap density is a further requirement for efficient spin injection contacts, as defects cause energy states in the band gap leading to electron capture. The capture and emission time of such states is in the microsecond regime [1, 2, 3, 4] while spin relaxation takes place at least one order of magnitude faster, resulting in the loss of spin polarization for captured electrons. The MIS diodes, investigated in the previous section, showed an apparent trap assistance in their transport behavior. For this reason, the control of the interface state density, D_{it} , is a central aspect for sputter-deposited MgO dielectrics.

On the other hand, an epitaxial MgO(001) tunneling barrier is the deliberate choice for high tunneling spin polarization. Spin-filtering effects have been already shown in magnetic tunnel junctions as well as CoFe-based tunneling diodes on GaAs [5, 6]. *Ab-initio* calculations investigating the silicon(001) complex band structure concerning spin injection from epitaxial Fe(001), revealed a total spin polarization for $k_{||} = 0$ [7]. This feature is attributed to the Δ_1 symmetry of the silicon wave function at the center of the Brillouin zone, blocking the Fe(001) minority spin channel, lacking this

symmetry feature. In this case, the conduction sites are shown to depend strongly on the level of the Fermi energy in the band structure. Crystalline MgO(001) is known to have a spin filtering effect for the Δ_1 symmetry at $k_{||} = 0$, cutting out the current contributions from other tunneling paths, leading to a considerable enhancement of spin polarization [7].

The sputtering deposition of epitaxial MgO(001) on the Si(001) surface has been shown to be challenging due to a large lattice mismatch of 22.5%. Using molecular beam epitaxy and pulsed laser deposition an epitaxial deposition of MgO on Si has been reported, characterized by intermixing and the formation of an interfacial oxide layer [8, 9, 10]. For barrier thicknesses compatible to MOSFET devices (2-4nm) and CMOS processing temperatures (up to 550°C), stress relaxation is anticipated, resulting in interface defects, e.g. dislocations, adding considerably to the D_{it} -value. Other high-k dielectric materials, when deposited directly on silicon, show as well a large interface trap density [11, 12]. To address this issue, a thin SiO₂ film is deposited prior to the high-k material, resulting in a high quality interface to silicon and increasing the dielectric performance in comparison to direct deposition of the high-k layer.

In the following a similar approach is investigated, growing a thin SiO₂ layer prior to MgO. Metal-oxide-semiconductor (MOS) capacitors, incorporating a CoFe electrode, are used to characterize the structural properties and the electrical performance of the SiO₂/MgO dielectric bi-layer in comparison to MgO and SiO₂ dielectrics.

4.2 Fabrication

Different types of MOS capacitors have been fabricated for structural and electrical investigation, elaborating three different dielectric layers, namely MgO(5 nm), SiO₂(2.5 nm)/MgO(2.5 nm), and SiO₂(5 nm), all with Co₇₀Fe₃₀ FM electrodes and Ta/Au capping layers. All different stacks have been prepared by room temperature magnetron sputter-deposition, DC for metals and RF for the ceramic MgO target. Employing n-Si(001) substrates with a doping density $N_d = 10^{15}\text{cm}^{-3}$ and 50nm thick thermal oxide on top (Fig. 4.5(a)), the substrates were firstly etched in buffered HF, resulting in a H₂ terminated clean Si surface (Fig. 4.5(b)). For the deposition of the single MgO dielectric, the sample has been transferred directly into the sputtering tool after etching. For the other samples thermal SiO₂ has been regrown at 850°C in pure O₂ atmosphere, followed by a 950°C annealing for 1 min in pure Ar and a forming gas step at 450°C for 5 min. Approximately 1 nm of the SiO₂ dielectric has been removed using low-concentration diluted HF, before transfer to the sputtering tool. All the samples have been heated *in-situ* to 200°C for evaporating condensed water prior to sputtering-deposition (Fig. 4.5(c)). In the following UV lithography has been used to define the capacitance structures (Fig. 4.5(d)). In a further sputtering step a Ta(10 nm)/Au(200 nm) hard-mask was deposited (Fig. 4.5(e)) and structured by simple lift-off processing (Fig. 4.5(f)). Finally, ion beam etching was used to transfer the masked regions into the sputter deposited stack. The etching

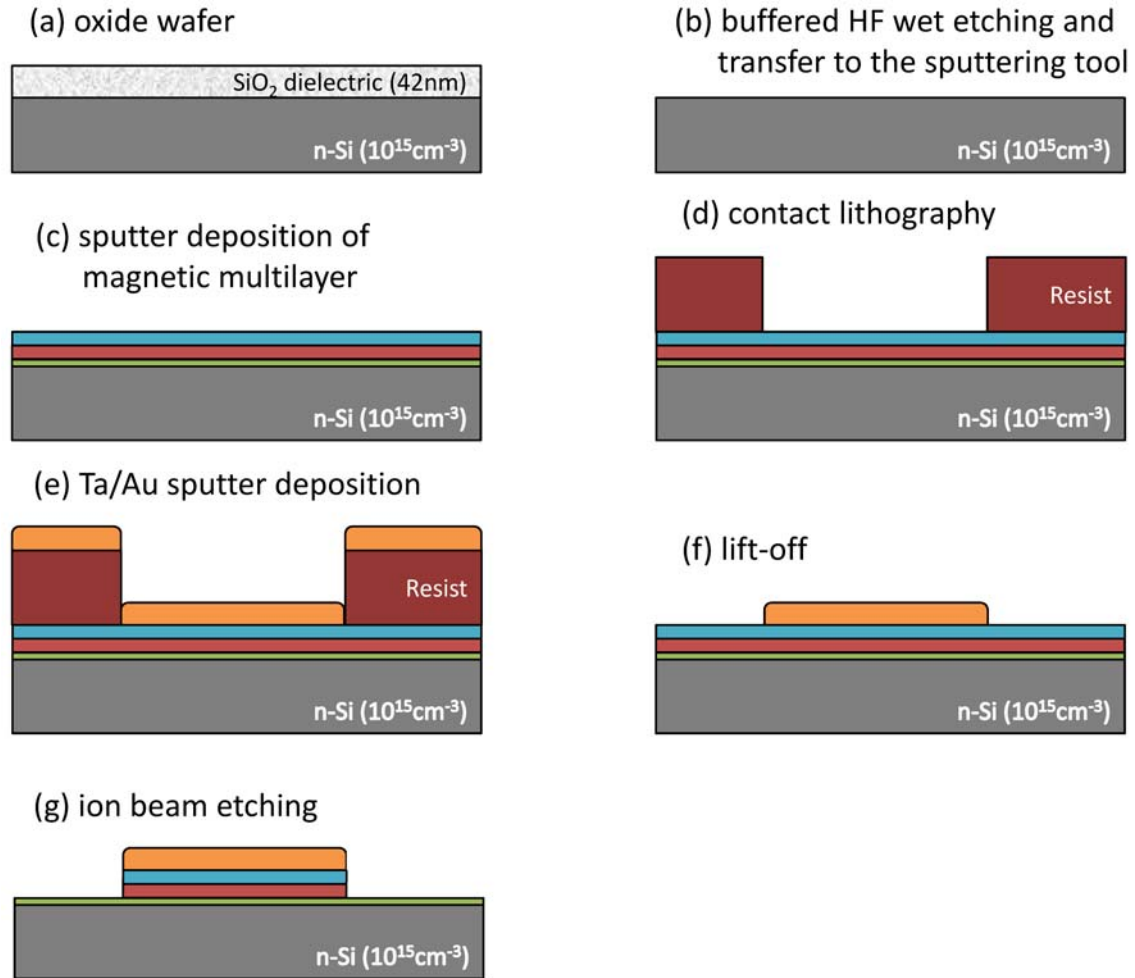


Figure 4.1: Individual processing steps for MOS capacitors

depth has been controlled by secondary ion mass spectrometry to prevent damage to the Si surface (Fig. 4.5(g)). Thereafter, some of the samples have been annealed at 400°C for 30 min in Ar or forming gas (10% H₂ and 90% N₂) to densify the oxide and improve the structural quality.

4.3 Structural characterization

The structural comparison of SiO₂/MgO and MgO barriers has been conducted by means of transmission electron microscopy (TEM). The crystallographic structure has been examined by high-resolution TEM (HRTEM). To examine the structural stability of the samples, the chemical composition has been characterized by scanning TEM (STEM) using a z-contrast high angle annular dark-field (HAADF) detector. Cross-sectional samples were oriented along to the Si[110] zone-axis, verifying the investigation of the layers edge-on. The scanning TEM (STEM) line scans were

conducted along the Si[001] direction with a probe diameter under 0.2 nm. The shown line scans, Electron Energy Loss Spectra (EELS) and the signal from the Mg K signal from Energy Dispersive X-Ray (EDX) were collected at spatial intervals of <0.5 nm.

In an initial experiment, the thermal stability of a 2.5 nm MgO layer on 50 nm thick thermal SiO₂ has been examined. The structure has been characterized in the as-deposited state as well as after annealing at 300°C. In Fig. 4.2(a) a HRTEM image of this structure after annealing is depicted aside to the HAADF STEM image of the respective region (Fig. 4.2(b)). Fig. 4.2(c) shows the relation between the intensities of EDX Mg K α and HAADF signals collected during a line scan, where the schematic position is indicated in Fig. 4.2(b). Both, the HRTEM analysis and the EDX line scan, determining the full width half maximum of the Mg K α signal, revealed a MgO thickness of 2.4 ± 0.3 nm for the as-deposited and annealed state. This confirmed that no considerable intermixing between MgO and SiO₂ occurs during deposition or annealing. Most interestingly, the HRTEM image shows the full crystallization of the MgO barrier.

In the subsequent experiment MOS capacitors have been fabricated, where Fig. 4.3 shows the cross-sectional HRTEM images of the ones with (a) MgO(5 nm) and (b) SiO₂(2.5 nm)/MgO(2.5 nm) dielectrics, with the Fourier transform of the barrier region depicted in the inset. For the single MgO(5 nm) dielectric layer the first part of the MgO layer with a thickness ~ 2 nm stays amorphous after annealing at 400°C for 30 min, while the rest layer thickness of ~ 3 nm crystallizes into cubic phase with preferred (001) orientation. The large lattice mismatch is accounted for the first amorphous layer, while after this first nucleation layer crystalline growth is achieved. As a consequence, sputtered MgO layers with a thickness in the range of 1-3 nm are too thin for crystallization [13, 14]. For the SiO₂/MgO bi-layer dielectric MgO as well crystallizes in (001) crystallographic orientation on the amorphous SiO₂ buffer. The lattice parameters, extracted from the Fourier transform of the crystalline barrier region, reveals approximately the bulk value (accuracy $<2\%$). For both samples the crystalline growth of MgO may be explained by stress-free crystallization on an amorphous substrate.

The use of a dielectric double-layer elaborating MgO(001) as a tunneling barrier for spin injection is thought to be beneficial for the spin polarization. However, for spin injection diodes a total dielectric thickness around 5 nm is far too thick for a substantially high tunneling current. Therefore, a SiO₂/MgO tunneling barrier with an overall thickness of 3 nm has been finally examined. Furthermore, Co₆₀Fe₂₀B₂₀ is chosen as a FM electrode material, exhibiting the highest magneto-resistance changes in MTJs with crystalline MgO barriers [15]. In Fig. 4.4(a) a cross-sectional HRTEM image of such CoFeB/MgO(1.5 nm)/SiO₂(1.5 nm)/Si diode is presented after thermal annealing at 550°C for 60 min, exceeding considerably standard CMOS processing temperatures. The dielectric layer thicknesses of 1.6 nm and 1.7 nm (± 0.3 nm) can be differentiated. The Fourier transform of the crystalline barrier region is shown in the inset, evidencing that even when 5 unit cells-thick, the structure is cubic with (001) orientation with respect to Si. The CoFeB magnetic electrode shows dispersed crystalline regions (not visible in this zoom-in). The chemical sta-

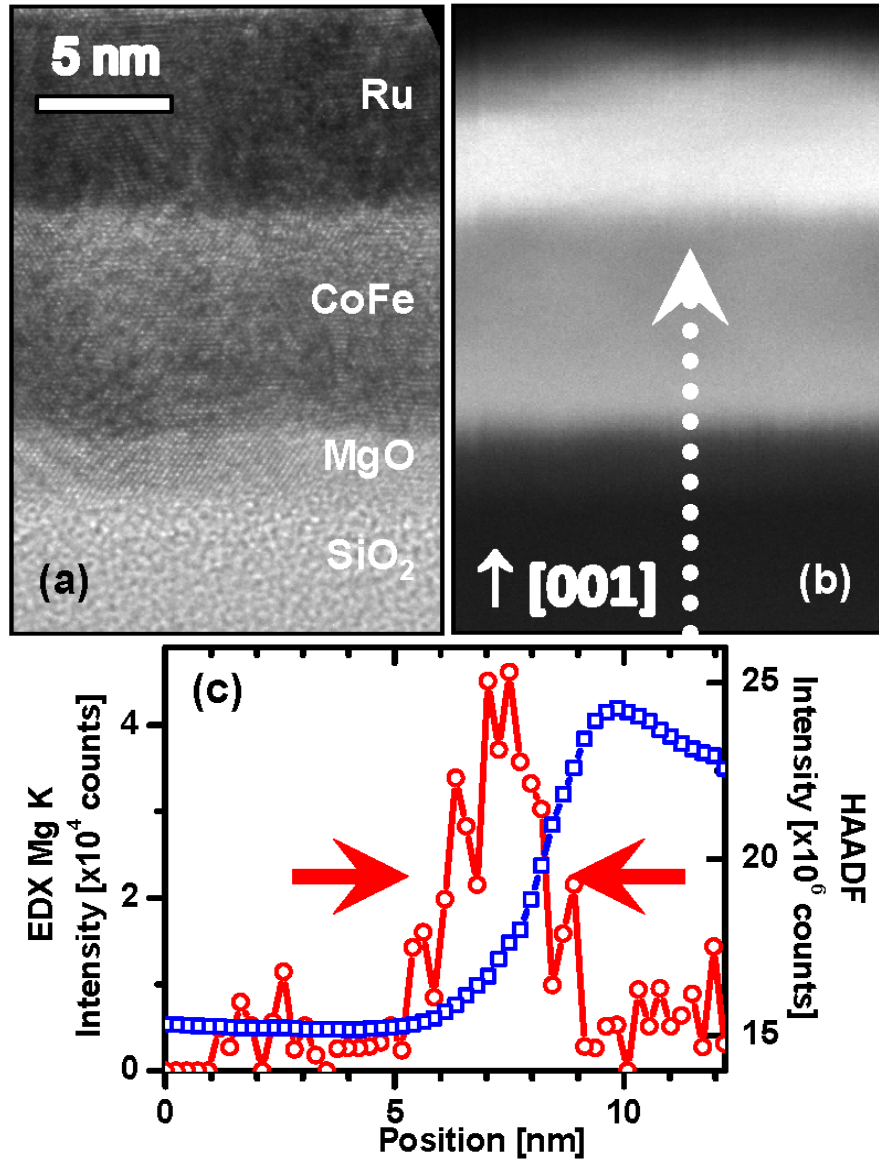


Figure 4.2: (a) Cross-sectional HRTEM and (b) z-contrast HAADF STEM images of a Ru/CoFe/MgO(2.5nm)/SiO₂(50 nm)/Si sample after annealing at 300° C for 60 min. (c) Intensities of EDX Mg K α and HAADF signals for a STEM line scan in direction indicated in (b)

bility of this structure has been determined by means of STEM line scans, where HAADF, EDX Mg K and EELS (core-loss edges: O K, Fe L and Co L) signals were determined simultaneously. The sketched arrow in the HAADF image, Fig. 4.4(b), denotes the scan direction. Low loss EELS verified that the sample thickness is below one inelastic mean free path of the incident electrons, enabling quantitative analysis. The areal density calculations are shown in Fig. 4.4(c) for O, Co and Fe, where the detailed calculation procedure can be found in [16]. In addition, the Mg

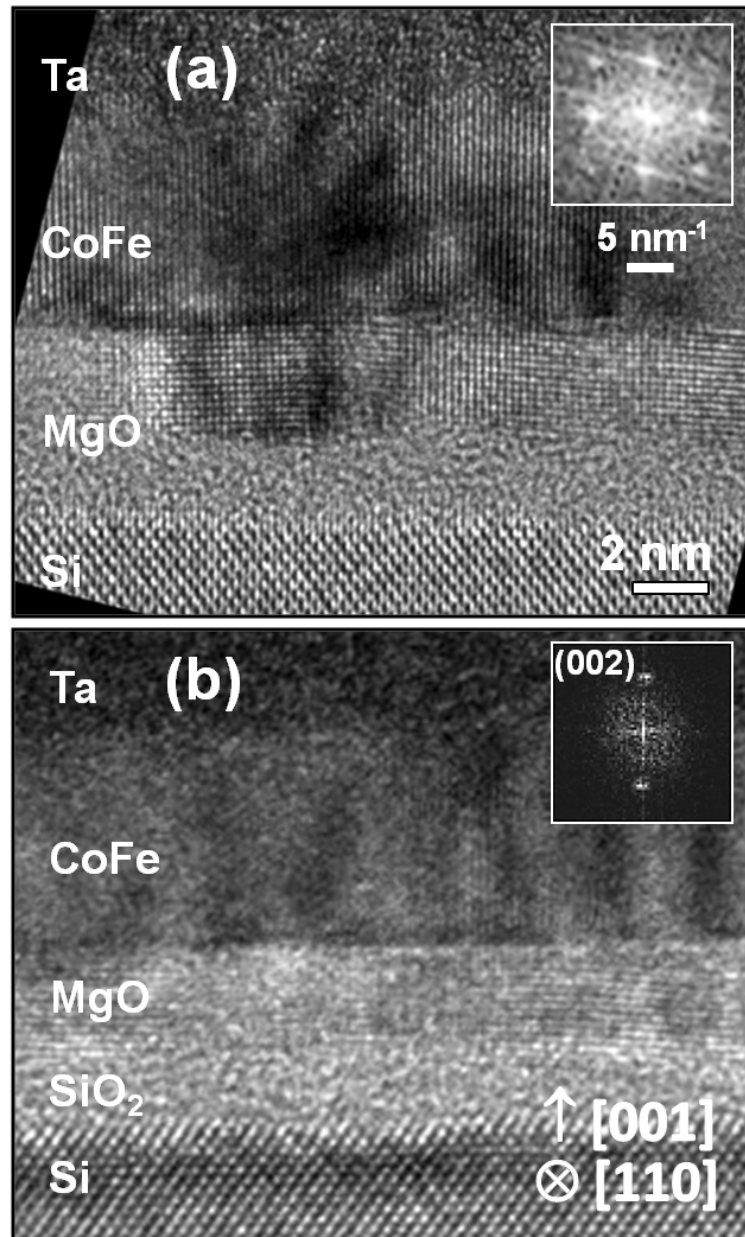


Figure 4.3: Cross-sectional HRTEM images of (a) MgO(5nm) and (b) MgO(2.5nm)/SiO₂(2.5nm) structures after annealing at 400° C for 60 min. The inset shows the Fourier transforms from the crystalline MgO regions of the barrier.

K EDX signal is presented in in the same graph. In summary, layers containing Mg and O are distinguished clearly with FWHM of measured profiles of 1.8 ± 0.2 nm and 3.2 ± 0.2 nm, respectively, being in agreement to the HRTEM results for MgO and SiO₂/MgO regions.

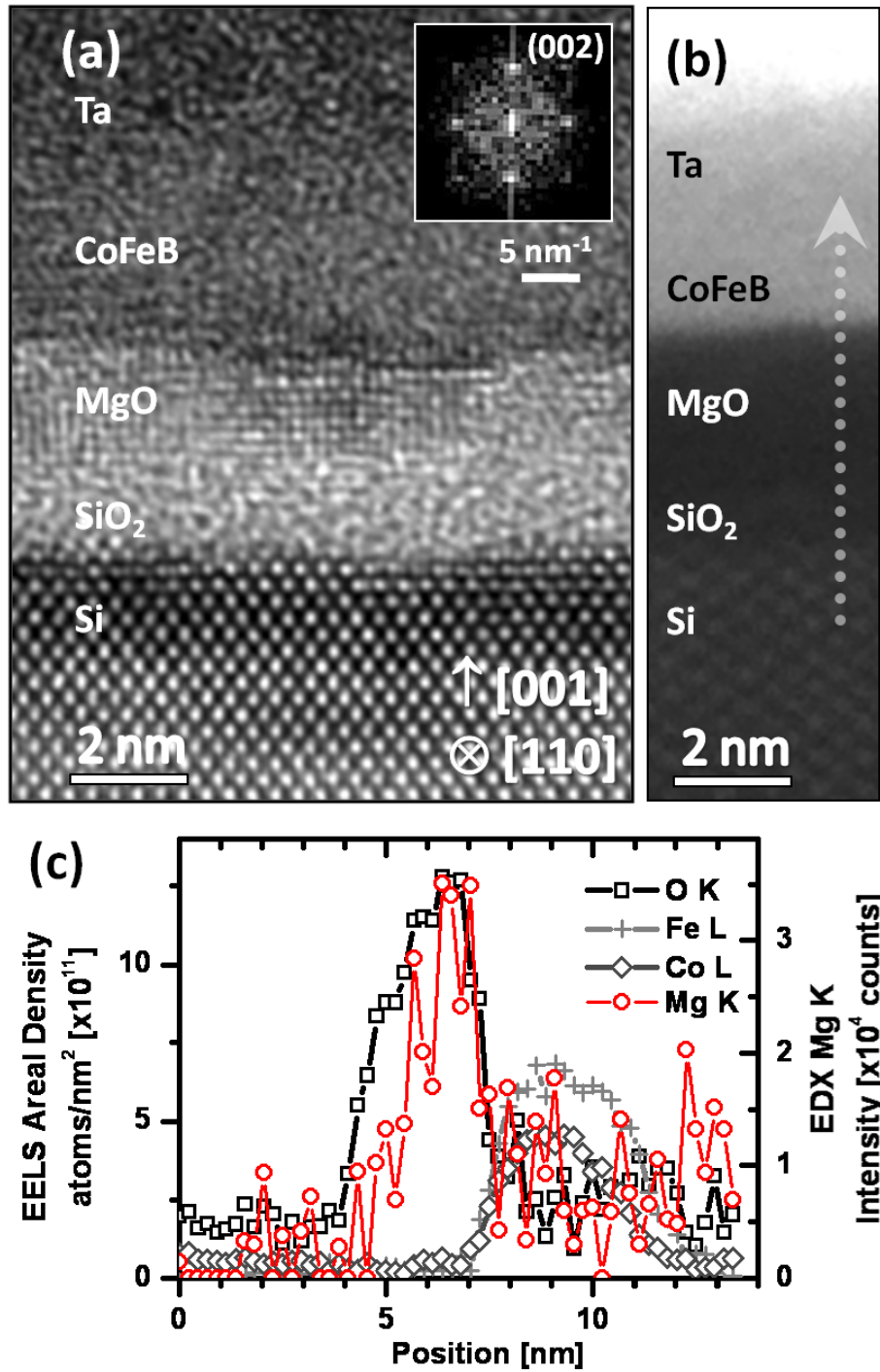


Figure 4.4: Cross-sectional HRTEM (a), and Z-contrast HAADF STEM (b) images of a Ta/CoFeB/MgO(1.5 nm)/SiO₂(1.5 nm)/Si sample after annealing at 550°C for 60 min. (c) The intensities of EDX Mg K α and EELS O K, Fe L, Co L signals collected during a STEM line scan, for a line-scan which direction is sketched in (b).

4.4 Electrical characterization

For the electrical characterization of the MOS capacitors different analysis methods have been elaborated, namely current-voltage (IV), capacitance-voltage (CV) and frequency dispersive conductance (G_p/ω) measurements. Every single technique reveals specific information of the dielectric.

The electrical measurement setup for MOS capacitors is shown on the left of Fig.4.5. Aside to that, the equivalent circuit of MOS capacitors is depicted, consisting of the oxide capacitance C_{ox} , the voltage dependent depletion layer capacitance C_s , the frequency dependent interface trap capacitance C_{it} and the frequency dependent parallel conductance G_p corresponding to the trap assisted emission of carriers via interface traps. Furthermore, the tunneling conductance G_t and the series resistance R_s are introduced to account for tunneling currents and the measurement setup, respectively. The measured parallel conductance, G_m , and parallel capacitance, C_m , can be translated to the components of the aforementioned equivalent circuit. To account for the series resistance, corrected values for the capacitance and conductance are calculated, using the expressions below [2]:

$$C_c = \frac{C_m}{(1 - G_m R_s)^2 + \omega^2 C_m^2 R_s^2} \quad (4.1)$$

$$G_c = \frac{\omega^2 C_m C_c R_s - G_m}{G_m R_s - 1} \quad (4.2)$$

The flat band voltage, V_{FB} , corresponds in an ideal MOS diode to the work function difference between semiconductor and metal, Φ_{ms} , needed to eliminate the band bending. Since in real devices also oxide charges are present, V_{FB} is shifted, according to [2] (for a MOS diode on n-Si with positive oxide charges):

$$V_{FB} = \Phi_m - \chi_s - \frac{E_{g,s}}{2q} + \Phi_{bulk} - \frac{Q_f}{C_0} \quad (4.3)$$

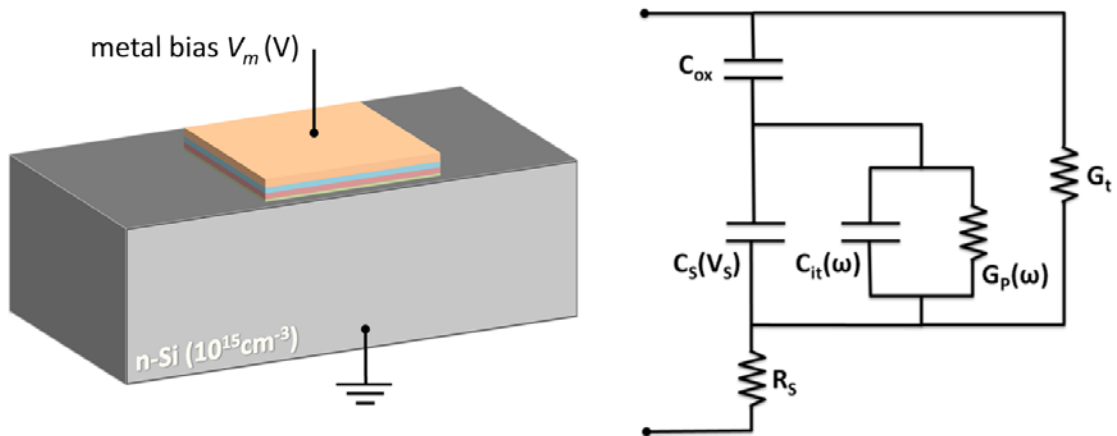


Figure 4.5: Schematic measurement setup of a MOS capacitors (left) and their equivalent circuit (right)

where Q_f is the fixed oxide charge density and C_0 is the area normalized oxide capacitance, defined as $C_0 = \epsilon_r \epsilon_0 / t_{ox}$ with the relative permittivity ϵ_r , the free space permittivity $\epsilon_0 = 8.85 \times 10^{-12}$ F/m and the oxide thickness t_{ox} .

Another characteristic is the interface trap density, D_{it} . For the quantitative determination of D_{it} different measurement techniques are possible. In this work, the conductance method as well as the quasi-static method have been elaborated, as introduced in the following. For the conductance method, D_{it} is extracted from admittance spectra (G_p/ω vs. ω) measurements [1, 2, 3]. This technique has been shown to be accurate even for MOS capacitors with ultrathin or leaky oxides and therefore presenting remarkable leakage current during the CV measurement [17]. With the corrected values as a basis, the G_p/ω can be calculated using the following formula, where G_{ac} is the corrected conductance excluding for the tunneling conductance G_t :

$$G_{ac} = G_c - G_t \quad (4.4)$$

$$\frac{G_p}{\omega} = \frac{\omega C_{ox}^2 G_{ac}}{G_c^2 + \omega^2 (C_{ox} - C_c)^2} \quad (4.5)$$

The plot of the normalized parallel conductance G_p/ω as a function of the angular frequency shows peaks at the angular frequency ω_{max} , corresponding to the maximum response of the interface traps. The value of G_p/ω as well as the peak frequency are shifted with applied bias. Therefore, the interface trap density distribution can be calculated for every applied bias using the relation:

$$D_{it} = \frac{2.5}{qA} \left(\frac{G_p}{\omega} \right)_{\omega_{max}} \quad (4.6)$$

Besides the conductance method, the quasi-static method has been applied to extract information about the interface traps. The idea behind this technique is the limited response time of interface traps. CV curves are recorded once at low frequency (lf) and a second time at high frequency (hf), where the interface traps cannot respond. While usually high frequency measurements at 1 MHz suffice to rule out the contribution of the interface states to the CV characteristic, low frequency measurements have to be well thought, since interface traps and minority carrier inversion charges have to be able to respond to the ac probe frequency [3]. Using these hf and lf CV measurements, the D_{it} -value at certain bias can be determined from [3]:

$$D_{it} = \frac{C_{ox}}{q} \left(\frac{C_{lf}/C_{ox}}{1 - C_{lf}/C_{ox}} - \frac{C_{hf}/C_{ox}}{1 - C_{hf}/C_{ox}} \right) \quad (4.7)$$

where C_{lf} and C_{hf} are the corrected capacitance values for low and high frequency, respectively.

Fig. 4.6 presents capacitance-voltage (CV) measurements, recorded at frequency steps of 1000, 100, 10, 1, 0.5, 0.1 kHz of samples annealed at 400°C for 30 min in Ar, corrected for the series resistance. The relative hf-permittivity, ϵ_r , of the thermally grown SiO₂ and the sputter deposited MgO can be extracted, using the dielectric thicknesses determined by HRTEM measurements and the oxide capacitance, C_{ox} , extracted from high frequency CVs (1MHz) under accumulation (high positive metal

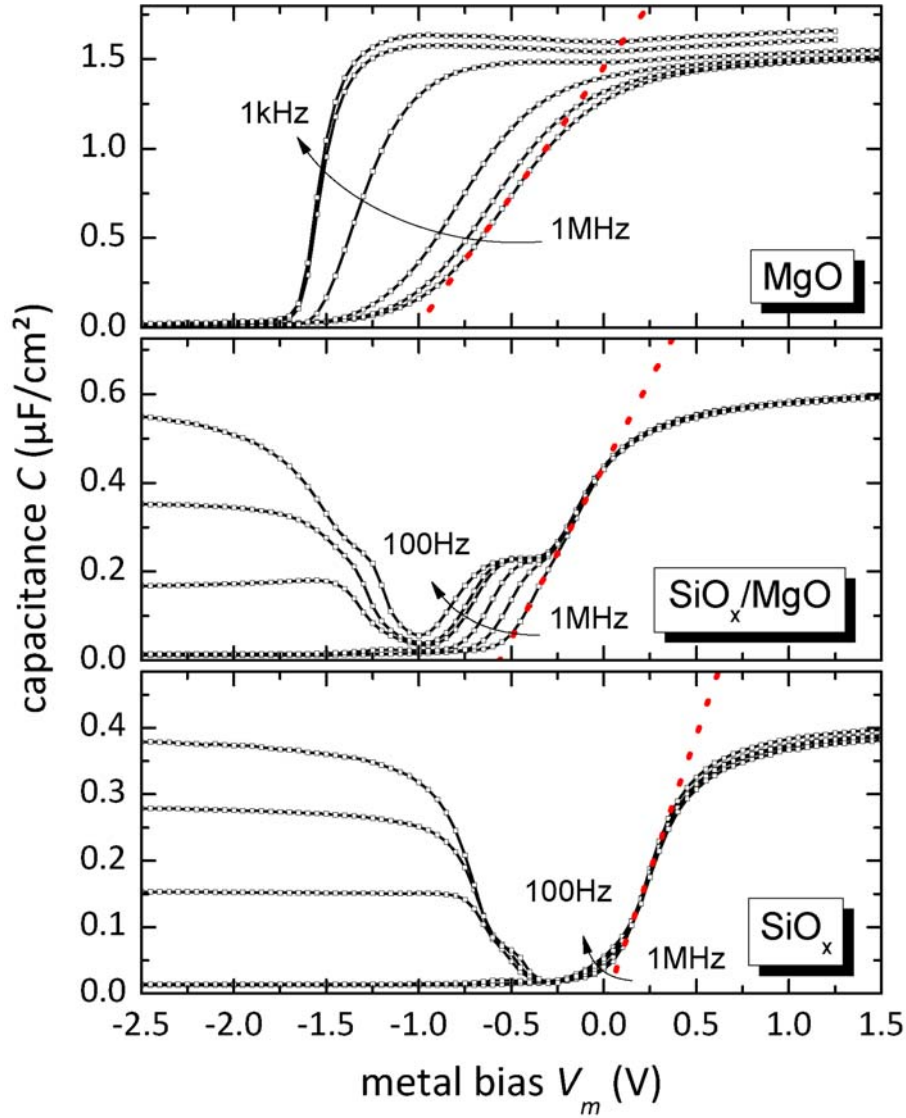


Figure 4.6: CV measurements of CoFe-based MOS capacitors with MgO, SiO₂/MgO, and SiO₂ dielectrics after 400° C/30 min Ar annealing. (Frequencies: 1000, 100, 10, 1, 0.5, and 0.1 kHz)

bias). The extracted permittivity values for MgO and SiO₂ are 8.4 and 2.3, respectively [18]. For the SiO₂/MgO bi-layer the permittivity of 3.5 exactly matches the calculated value, assuming a series connection of two plate capacitors of SiO₂ and MgO each with 2.5 nm dielectric thickness. Furthermore, the flat band voltage has been determined from hf-CVs, where the influence of the interface traps is low. The incorporation of MgO results in a shift of V_{FB} to more negative values. More specifically, V_{FB} is 0.1 V for SiO₂ and -0.55 V and -1.3 V for SiO₂/MgO and MgO dielectrics, respectively. The hf-CVs show a change in the slope at depletion, being smaller for MgO than for SiO₂ or the bi-layer stack. Despite the fact that interface states do not respond to the ac probe frequency, they do respond to the sweep of

the gate voltage [3]. This charging of the interface states changes the surface potential and therefore the band bending as a function of the gate voltage, leading to a stretch-out of the hf-CV curve. The pronounced frequency dispersion around V_{FB} evidences the larger D_{it} -value for MgO and MgO/SiO₂ compared to pure SiO₂.

The distribution of the interface trap density as a function of the surface potential, ϕ_s , is depicted in Fig.4.7 for SiO₂ and the dielectric bi-layer. These results have been obtained using the quasi-static technique. Unfortunately, for all annealing states of the MgO barrier as well as the as-deposited state of the SiO₂/MgO dielectric this technique could not be applied, since leakage currents were too large. For the displayed distributions of SiO₂, all measurements show a D_{it} maximum around $\phi_s = E_V + 0.8$ eV, with a value $4 \times 10^{12} \text{cm}^{-2} \text{eV}^{-1}$ in the as deposited state, decreasing to $4 \times 10^{11} \text{cm}^{-2} \text{eV}^{-1}$ and $2 \times 10^{11} \text{cm}^{-2} \text{eV}^{-1}$ for post-metallization annealing at 400°C in FG and Ar, respectively. As-deposited junctions have a minimum D_{it} valued of $3 \times 10^{11} \text{cm}^{-2} \text{eV}^{-1}$ for $\phi_s = E_V + 0.45$ eV. For the annealed junctions, the minimum of $D_{it} = 6 \times 10^{10} \text{cm}^{-2} \text{eV}^{-1}$ is shifted to $\phi_s = E_V + 0.55$ eV. It should be pointed out that there is no difference observed in D_{it} as a function of annealing gas for SiO₂ dielectrics.

For the SiO₂/MgO dielectric bi-layer the D_{it} distribution is shifted compared to SiO₂. More specifically, the position of maximum trap density is slightly decreased to approx. $E_V + 0.7$ eV for both annealing states. For this case, the forming gas annealed sample shows a maximum value of $D_{it} = 3 \times 10^{12} \text{cm}^{-2} \text{eV}^{-1}$, while the trap density observed for the Ar annealed sample is $6 \times 10^{12} \text{cm}^{-2} \text{eV}^{-1}$. More obvious is the increase of the acceptor like interface traps, shifting the absolute minimum to the vicinity of the conduction band at $\phi_s = E_V + 1.0$ eV. For SiO₂, the local D_{it} -minimum around mid-gap is decreased to $\phi_s = E_V + 0.42$ eV and a D_{it} -value of $5 \times 10^{11} \text{cm}^{-2} \text{eV}^{-1}$ or forming gas annealing. For Ar annealing a minimum at $\phi_s = E_V + 0.35$ eV with a interface trap density of $8 \times 10^{11} \text{cm}^{-2} \text{eV}^{-1}$ is observed. Additionally, for all the samples, D_{it} -values have been verified using the conductance technique. The conductance technique, though, only gives information in a limited regime of the surface potential. Table 4.1 compares D_{it} -values at flatband condition for the different dielectrics for all annealing states, determined by means of CV and G_p/ω measurements.

The relative permittivity is generally higher for MgO-based samples in the as-deposited state, being related to the higher leakage current during the CV measurement. The LCR meter is not able to compensate to full extent the tunneling currents under accumulation for such thin oxides. The shift of V_{FB} to more positive voltages as a function of the annealing is clearly present for all the samples, ranging between $\Delta V_{FB} = 0.2$ to 0.4 V. As it has been previously mentioned besides the oxide traps also the interface trap density determines V_{FB} . The D_{it} value at flat-band condition of the annealed MgO capacitors present no improvement compared to the as-deposited capacitors. On the contrary, annealing improves D_{it} by at least one order of magnitude for the capacitors incorporating SiO₂.

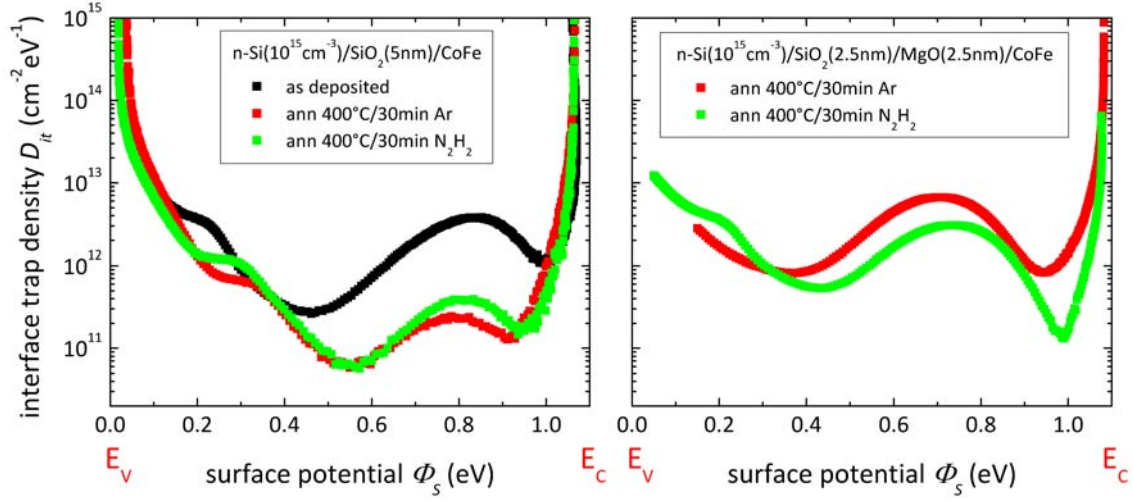


Figure 4.7: Interface trap density measurements of CoFe-based MOS capacitors with SiO₂ and SiO₂/MgO dielectrics as a function of the surface potential ϕ_s

Current transport through the Oxide

In the ideal case, current transport through the dielectric of a MOS diodes should be zero. In real MOS diodes, however, current conduction through the oxide is present, varying as a function of the external electric field and the oxide thickness. Recording the current density versus the applied voltage (JV), allows the determination of the dominating conduction mechanism. In the following the most important tunneling conduction mechanisms are introduced, before JV characteristics of MgO-based MOS diodes are investigated.

Fowler Nordheim Tunneling The band diagram for Fowler Nordheim Tunneling (FNT) is displayed in Fig. 4.8(a). For high applied metal bias the conduction band of the dielectric is highly distorted. The projected tunneling barrier width is therefore lowered, leading to direct tunneling through the triangular dielectric barrier. The most determining parameter for FNT tunneling is the tunneling barrier height. The current density corresponding to FNT transport is given by the expression [3]:

$$J_{FNT} = A^* E_{ox} \exp\left(-\frac{B^*}{E_{ox}}\right), \quad \text{with,} \quad (4.8)$$

$$A^* = \frac{q^3 m_0}{8\pi h m_{ox} \phi_{B,el}} = 1.54 \times 10^{-6} \frac{m_0}{m_{ox}} \frac{1}{\phi_{B,el}} \left[\frac{A}{V^2} \right] \quad (4.9)$$

$$B^* = \frac{8\pi \sqrt{2m_{ox} \phi_{B,el}^3}}{3hq} = 6.83 \times 10^7 \sqrt{\frac{m_{ox}}{m_0}} \sqrt{\phi_{B,el}^3} \left[\frac{V}{cm} \right] \quad (4.10)$$

where m_{ox} is the effective electron mass inside the oxide, m_0 the free electron mass, $\phi_{B,el}$ the effective barrier height at the silicon-oxide interface, and $E_{ox} = V_m/t_{ox}$

Table 4.1: Characteristic properties of MgO-based MOS capacitors

Sample		MgO	SiO ₂ /MgO	SiO ₂
dielectric thickness t_{ox} (nm)		5.0	2.6/2.5	5.0
oxide capacitance C_{ox} ($\mu\text{F}/\text{cm}^2$) extracted at 1 MHz	as deposited	1.763	0.711	0.331
	ann. 400°C/30min/Ar	1.497	0.604	0.404
	ann. 400°C/30min/FG	1.515	0.598	0.371
relative permittivity ϵ_r	as deposited	9.9	4.0	1.9
	ann. 400°C/30min/Ar	8.4	3.5	2.3
	ann. 400°C/30min/FG	8.5	3.4	2.1
flat band voltage V_{FB} (V)	as deposited	-1.75	-1.10	-0.3
	ann. 400°C/30min/Ar	-1.30	-0.7	0.1
	ann. 400°C/30min/FG	-1.40	-0.9	0.1
interface trap density D_{it} ($\text{cm}^{-2}\text{eV}^{-1}$) at flat band	as deposited	5×10^{13}	1×10^{14}	3×10^{12}
	ann. 400°C/30min/Ar	5×10^{13}	6×10^{12}	2×10^{11}
	ann. 400°C/30min/FG	6×10^{13}	3×10^{12}	4×10^{11}

the electric oxide field. This effective barrier height already includes barrier height lowering and quantization effects at the silicon interface. Furthermore, these equations are only valid for the assumption that the electrons in the emitting electrode can be described by a free Fermi gas, the electrons have a single effective mass inside the barrier, and the tunneling probability derives by taking into account only the electron momentum component normal to the interface. In the case all these assumptions apply, the JV according to FNT follows:

$$\ln \left(\frac{J}{E_{ox}^2} \right) = \ln A^* - \frac{B^*}{E_{ox}} \quad (4.11)$$

A plot of $\ln \left(\frac{J}{E_{ox}^2} \right)$ as a function of the inverse electric field inside the oxide, also known as Fowler-Nordheim-Plot. The linear portion of such plot identifies FNT as dominant transport process.

Direct Tunneling For an oxide thickness $t_{ox} < 4\text{-}5$ nm and a voltage drop over the tunneling barrier $V_{ox} < \phi_B = \phi_m - \chi_i$, direct tunneling of electrons from the metal to the semiconductor is allowed. As a consequence, already for small metal bias, V_m , considerable current conduction is present. The band diagram for direct tunneling (DT) is presented in Fig. 4.8(b). The current density for DT can be expressed analytically [3]:

$$J_{DT} = A^* E_{ox}^2 \exp \left(\frac{-B^* [1 - (1 - qV_{ox}/\Phi_{B,el})^{1.5}]}{E_{ox}} \right) \quad (4.12)$$

where A^* and B^* are defined same as for FNT conduction (Eq. 4.10). While the extracted barrier height, $\Phi_{B,el}$, for DT and FNT are identical, for DT the effective mass inside the barrier is different since electrons tunnel directly into the conduction band minimum of silicon, in contrast to tunneling into the conduction band of the oxide for FNT.

Trap Assisted Tunneling During fabrication or hot carrier injection, trap states within the band gap of the oxide may be generated. The band diagram for trap assisted tunneling (TAT) is presented in Fig. 4.8(c). For low distances of the trap to the metal, tunneling of electrons may already occur at low voltages. If the trap state has a higher potential than silicon's conduction band, the trapped electron may directly tunnel into silicon's conduction band or into another free trap state. For an increasing voltage drop in the oxide, trap assisted tunneling is more and more intermixed with Fowler-Nordheim tunneling, until at large voltages FN conduction is entirely dominating.

Frenkel-Poole Emission Frenkel-Poole emission describes the thermal emission of carrier, supported by an electric field, into Coulomb traps in the conduction band of the oxide. The band diagram of Frenkel-Poole emission (FP) is displayed in Fig. 4.8(d). The thermal energy would not be sufficient to emit a carrier, while an electric field causes a reduction of the barrier height on the side of the traps, enabling carrier transport. Before the capture of an electron traps are positively charged. After capturing an electron the charge of the traps is compensated, eliminating their electrical effect until emission of the captured electron. The current density related to FP conduction can be expressed, assuming an equal barrier height, ϕ_{FP} , for all traps [19]:

$$J_{FP} = CE_{ox} \exp\left(-\frac{q\phi_{FP} - \beta\sqrt{E_{ox}}}{kT}\right) \quad \text{with,} \quad (4.13)$$

$$\beta = \sqrt{\frac{q^3}{\pi\epsilon_0\epsilon_r}} \quad (4.14)$$

where C is a constant and β the Frenkel-Poole constant.

Frenkel-Poole emission is not obviously visible in measured JV characteristics of MOS diodes. However, by plotting $\ln \frac{J}{E_{ox}}$ as a function of $\sqrt{E_{ox}}$, the so called Frenkel-Poole plot, results in a straight line where FP is the dominating transport mechanisms.

Fig. 4.9 (a) and (b) display the JV characteristics of the CoFe-based MOS diodes incorporating MgO(5nm) and SiO₂(2.5nm)/MgO(2.5nm) dielectric layers, shown in the as deposited state and after annealing at 400°C/30min in Ar and FG atmosphere. Obviously, for the MgO dielectric stack the annealing does not change the transport characteristic. For the SiO₂/MgO stack, though, a change in the

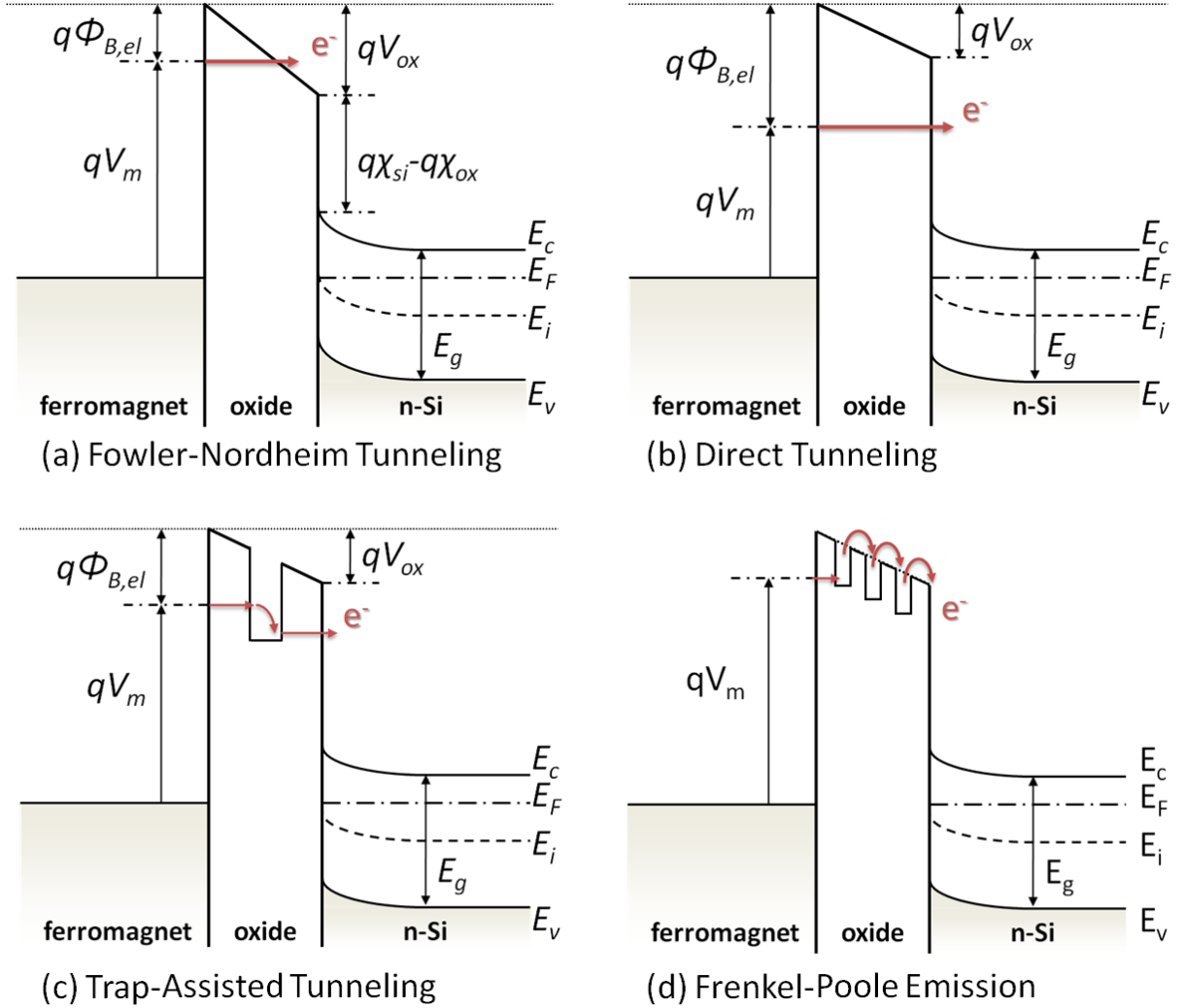


Figure 4.8: Band diagrams different current conduction mechanisms in MOS diodes: Fowler-Nordheim tunneling (a), Direct Tunneling (b), Trap-Assisted Tunneling (c) and Frenkel-Poole Emission (d)

JV characteristic is present after annealing. From the structural characterization, presented in Section 4.3, this change can be related to the crystallization of MgO in a cubic phase, when deposited on SiO₂. In contrast for pure MgO, the interfacial region remains amorphous after annealing. The JV characteristics are plotted in a Fowler-Nordheim plot in Fig. 4.9 (c) and (d). The linear fits in the FN-plots of the annealed dielectric bilayer (Fig. 4.9(c)) identify current conduction by Fowler-Nordheim tunneling for E_{ox} ranging from 1.0×10^{-9} to 1.6×10^{-9} (V/m)⁻¹. This range corresponds to a forward bias from 3.0 V to 4.9 V. For the MgO barrier the FN-plot, though, does not reveal a linear part, excluding conduction by Fowler-Nordheim tunneling. The calculation of the barrier height for MgO/SiO₂ capacitors from the slope of the linear fits, according to Eq. 4.10, and an effective electron mass $m_{ox} = 0.35$ (as given in Table 3.1) leads to an electron barrier height $\phi_{B,el}$ of 2.21 eV and 2.16 eV for Ar and forming gas annealing, respectively. For

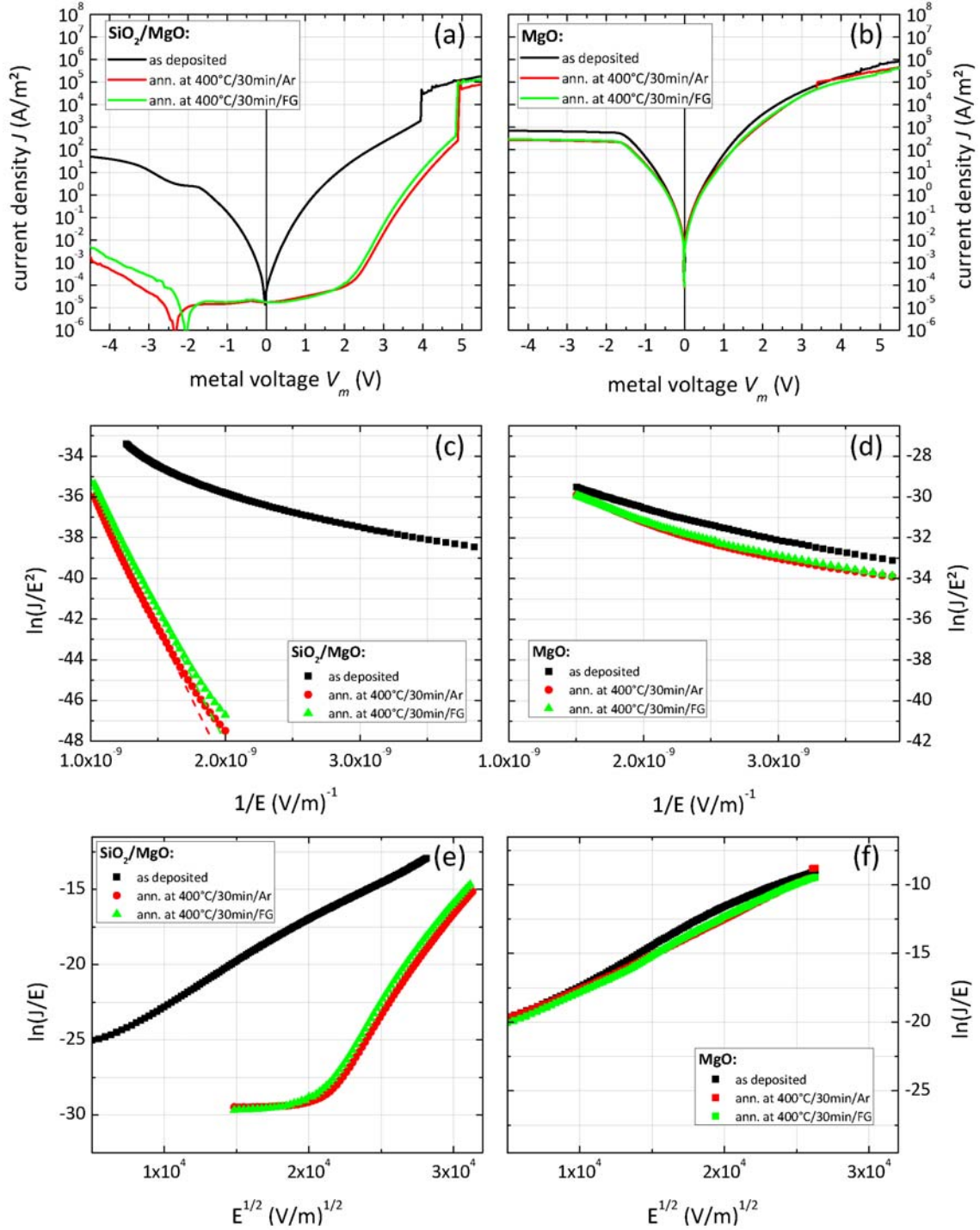


Figure 4.9: Room-temperature JV characteristics of CoFe-based MOS diodes incorporating $\text{MgO}(5\text{nm})$ and $\text{SiO}_2(2.5\text{nm})/\text{MgO}(2.5\text{nm})$ presented in the as-deposited state as well as after annealing at $400^\circ\text{C}/30\text{min}$ in Ar and forming gas (FG) atmosphere, with their respective Fowler-Nordheim (c - d) and Frenkel-Poole plots (e - f).

the as-deposited state of the SiO_2/MgO dielectric as well as the MgO dielectric, conduction by Fowler-Nordheim tunneling does not apply. Further investigating

the current transport properties with respect to Frenkel-Poole (FP) emission (Fig. 4.9 (e) and (f)) results in straight lines for all cases. However, for MgO and the as-deposited bilayer dielectric such large currents are anticipated to result from FP emission. In these cases already at low metal bias ($|V_m| < 1\text{ V}$) high current is conducted, where the electric field is too low to lift electrons into coulomb traps in the conduction band of the dielectric. The shallow slope of the FP plots for these cases are thought to be related to trap assisted tunneling, arising from the amorphous nature of the MgO. On the other hand for the annealed bilayer dielectric FP conduction is as well present, starting at a metal bias $V_m = 2.3\text{ V}$. The presence of FNT and FP as a conduction mechanism may be explained due to the dielectric bilayer of SiO₂ and MgO. Both dielectrics feature a different band gap, resulting in a discontinuous conduction band which serves as a potential well for FP emission. The oxides' breakdown voltage for SiO₂/MgO and MgO differs as a function of the thermal annealing increasing from 3.95 V ($E_{ox} = 7.9 \times 10^8\text{ V}$) for the as-deposited state to 4.9 V ($E_{ox} = 9.8 \times 10^8\text{ V}$) for the annealed states of the SiO₂/MgO dielectric. For the MgO dielectric the oxide integrity is lower, showing a dielectric breakdown voltage of 3.5 V ($E_{ox} = 7.0 \times 10^8\text{ V}$) for all annealing states.

4.5 Conclusion

In conclusion, the structural and electrical properties of CoFe-based MOS capacitors incorporating SiO₂, SiO₂/MgO and MgO dielectrics have been investigated. MgO, when deposited on thermally grown SiO₂, crystallizes in a cubic phase with preferred (001) crystallographic orientation. Further annealing up to 550°C/60 min does not lead to significant intermixing, neither with the SiO₂ barrier nor the ferromagnetic CoFe electrode. Conversely, for MgO directly deposited on silicon no crystallization is observed for the initial 1-2 nm, attributed to the large lattice mismatch between MgO and silicon.

The CV characteristics of the MOS capacitors are significantly influenced by their D_{it} values, being as high as $5 \times 10^{13}\text{ cm}^{-2}\text{ eV}^{-1}$ for MgO after annealing at 400°C. In comparison to MgO, annealed MOS capacitors incorporating SiO₂/MgO feature one order of magnitude reduced D_{it} value, which is further reduced by one order of magnitude for pure SiO₂.

Finally, the carrier transport mechanisms for MgO and SiO₂/MgO capacitors have been investigated. For SiO₂/MgO barriers annealing changes the conduction process from trap assisted tunneling to Frenkel-Poole emission and Fowler Nordheim tunneling. This clearly shows the increase of the oxide integrity after crystallization due to annihilation of trap states in the MgO layer. On the other hand the decrease in D_{it} as well suggests increasing oxide integrity. However, annealing does not change the transport properties of MgO, where trap assisted tunneling is dominating for all annealing states.

REFERENCES OF CHAPTER 4

- [1] Sze, S. M. *Physics of Semiconductor Devices*. John Wiley & Sons, second edition, (1981).
- [2] Nicollian, E. H. and Goetzberger, A. *IEEE Transactions on Electron Devices* **12**, 108–117 (1965).
- [3] Schroder, D. *Semiconductor Material and Device Characterization*. Wiley & Sons, 2nd edition edition, (1989).
- [4] Chakraborty, S., Bera, M. K., Bose, P. K., and Maiti, C. K. *Semiconductor Science and Technology* **21**, 335–340 (2006).
- [5] Yuasa, S. and Djayaprawira, D. D. *Journal of Physics D: Applied Physics* **40**, 337–354 (2007).
- [6] Jiang, X., Wang, R., Shelby, R., and Parkin, S. *IBM Journal Research and Development* **50**(1), 111 (2006).
- [7] Mavropoulos, P. *Phys. Rev. B* **78**, 054446 (2008).
- [8] Fork, D., Ponce, F., Tramontana, J., and Geballe, T. *Appl. Phys. Lett.* **58**, 2294 (1991).
- [9] Miao, G., Chang, J., van Veenhuizen, M., Thiel, K., Seibt, M., Eilers, G., Münzenberg, M., and Moodera, J. **93**, 142511 (2008).
- [10] Ning, M., Mi, Y., Ong, C., Lim, P., and Wang, S. *J. Phys. D: Appl. Phys.* **402**, 3678 (2007).
- [11] Wilk, G. D. and Wallace, R. M. *Applied Physics Letters* **74**, 2854 (1999).
- [12] Wilk, G. D. and Wallace, R. M. *Applied Physics Letters* **76**, 112 (2000).
- [13] Uhrmann, T., Dimopoulos, T., Brückl, H., Lazarov, V. K., Kohn, A., Paschen, U., Bär, L., and Rührig, M. *Journal of Applied Physics* (2007).

- [14] Uhrmann, T., Dimopoulos, T., Kovacs, A., Kohn, A., Weyers, S., Paschen, U., Smoliner, J., and Brückl, H. *Journal of Physics D: Applied Physics* **42**, 145114 (2009).
- [15] Djayaprawira, D. D., Tsunekawa, K., Nagai, M., Maehara, H., Yamagata, S., and Watanabe, N. *Applied Physics Letters* **86**(09), 2502–2504 (2005).
- [16] Kohn, A., Kovacs, A., Uhrmann, T., Dimopoulos, T., and Brückl, H. *Appl. Phys. Lett.* , 042506 (2009).
- [17] Vogel, E. M., Henson, W. K., Richter, C. A., and Suehle, J. S. *IEEE Transactions on Electron Devices* **47**(3), 601 (2000).
- [18] Kar, S. *IEEE Transactions on Electron Devices* (50), 2112 (2003).
- [19] Harrell, W. and Frey, J. *Microelectronic Engineering* **22(1-4)**, 281 (1993).

CHAPTER 5

CONCLUSION AND PERSPECTIVES

The realization of a spin field effect transistor (spinFET) constitutes the fundamental idea of this thesis. A spinFET consists of two ferromagnetic (FM) source and drain electrodes, connected by a semiconductor (SC) transport channel. Such device would facilitate information processing and data storage within one unit, employing a magneto-current effect. However, the successful implementation of a spinFET faces different challenges: (i) injection of spin-polarized current from the FM source contact to the SC channel, (ii) spin conserving current transport through the SC channel, (iii) detection of the spin information at the FM drain contact. Silicon as a host material features the key advantage of a long spin lifetime due to its lack of a nuclear spin. Silicon's inversion symmetric unit cell additionally results in a higher spin lifetime due to reduced spin-orbit interaction, compared to III-V compound semiconductors. On the other hand, spin-orbit interaction facilitates the spin-manipulation in compound semiconductors, while for silicon spin-manipulation can only be achieved by means of external magnetic fields. Up to date, the implementation of a spinFET on silicon stays elusive, partly due to the inability to solve, using optical techniques, the spin injection, detection and transport separately. This means that we can only address all these issues at ones, in a complete devices, using electrical means.

In Chapter 1 the major obstacle for spin injection in the form of the conductivity mismatch between the FM contacts and silicon has been identified. The insertion of a tunneling barrier is beneficial to surpass this obstacle if the resistance area (RA) product of the contacts can be tuned into a narrow range. This range is determined by the silicon doping density and as a consequence the spin lifetime and the conductivity of the semiconductor channel. The amplitude of the magneto-current effect on the other hand is mostly determined by the spin polarization of the injected current. Consequently, the desired properties of source and drain contacts can be summarized as follows: (i) appropriate RA product, (ii) high tunneling spin polarization and (iii) controlled magnetic switching.

In Chapter 3 the structural, electrical and magnetic properties of ferromagnetic Schottky diodes and MgO-based tunneling diodes have been investigated, elaborat-

ing CoFe/NiFe, NiFe and CoFeB ferromagnetic electrodes, fabricated by sputter deposition. Both, Schottky and metal-insulator-semiconductor (MIS) diodes, show an almost atomically flat silicon surface and a sharp interface to the sputter deposited layers, with no sign of a native oxide. The structural investigation showed polycrystalline CoFe and NiFe ferromagnetic layers, while CoFeB and MgO are amorphous after deposition. For annealing up to 400°C, CoFeB shows dispersed crystalline regions. The MgO stays amorphous even after annealing, due to the large lattice mismatch between MgO and Si. The MIS diodes show no sign of intermixing, examined by EFTEM measurements, where even a MgO layer with a thickness of 1.5 nm offers a reliable diffusion barrier. For the Schottky diodes extensive interdiffusion is present for CoFe/NiFe and NiFe diodes. For CoFeB, on the other hand the diffusion seems to be below the resolution limit of EFTEM technique.

In the following, the electrical properties of Schottky and MIS diodes have been investigated as a function of the silicon doping type (n- and p-doping) and density, ranging from 10^{15} to 10^{18}cm^{-3} . For n-Si Schottky diodes, the reverse bias, corresponding to electron injection, is 6-7 orders of magnitude higher than the requested RA values. Including MgO as a tunneling barrier leads to substantial increase of the injection current, resulting from a substantial lowering of the effective Schottky barrier height (SBH). This is partly attributed to the presence of positive oxide charges. On the other hand, interface traps, as well, contribute to the lowering of the SBH. A large amount of interface traps, though, has a detrimental effect on the spin polarization of the injected electrons, since the capture/emission times are high relative to the spin lifetime. In any case, even for the MIS diodes, the RA values are still 2-3 orders of magnitude too large for highly efficient spin injection. The RA values under forward bias of the diodes are closer to the required resistance range, especially for low doped n-Si.

For p-Si Schottky diodes majority transport has been identified as dominant conduction mechanism. In contrast, MgO-based MIS diodes on p-Si are characterized by their minority carrier transport characteristic. In the case of Schottky diodes, the main current contribution flows into the valence band of silicon where spin relaxation happens on the same timescale as momentum relaxation, leading to fast carrier depolarization. As a consequence, p-Si MIS diodes are favoured, where electron transport into the semiconductor conduction band dominates. In this case, injection of spin-polarized electrons takes place under forward bias. For large forward bias high current densities can be achieved for all doping densities, though, injection takes place into a hole accumulated silicon surface, where electron-hole interaction leads to fast spin depolarization. However, it has been further shown that under low forward bias for low doped p-Si, an inversion layer is present at the interface, resulting in a vanishing Schottky barrier and consequently in a large injection current. The absence of holes for an inverted silicon interface increases the spin-lifetime. Furthermore, spin polarization of the injected electrons is increased for low injection voltages as well. In conclusion, the presence of the inversion layer for p-Si MIS diodes can be exploited to manufacture low resistive contacts with low electron-hole spin interaction. Additionally, the presence of the inversion layer,

featuring a low barrier height for spin detection as well, should lead to improved spin detection efficiencies. This inversion layer is attributed to the presence of positive oxide charges within the MgO tunneling barrier. One might be concerned about spin-depolarization caused by an interaction of oxide traps with tunneling electrons. However, for TMR junctions incorporating a non-stoichiometric MgO tunneling barrier, the electron-trap interaction time has been shown to be too short to cause spin scattering. As a result, MIS diodes on 10^{15}cm^{-3} doped p-Si are considered good candidates for spin injection and detection contacts. Indeed, the RA values under forward bias have been shown to strike the required range for a semiconductor channel length of 100 nm and also the reverse current is close to this regime.

Apart from the oxide traps incorporated in MgO, interface traps have been shown to influence the transport characteristics of the investigated diodes. The extraction of the interface trap density, D_{it} , showed a relatively high D_{it} -value of $8 \cdot 10^{13} \text{cm}^{-2}\text{eV}^{-1}$. This magnitude, being at least 2 orders of magnitude larger than in state-of-the-art CMOS devices, is most likely related to the sputter deposition technique for the deposition of the tunnel barrier. Comparable D_{it} -values were found on both, n- and p-doped silicon. This high trap density can account for the pronounced contribution of trap assisted tunneling to the overall transport characteristic. A large amount of interface traps can constitute an additional spin relaxation channel, diminishing the overall spin injection and detection efficiency.

The magnetic switching requirements for the injection/detection contacts, being: (i) small switching field, (ii) high remanent magnetization and (iii) magnetic selectivity, have been fulfilled for CoFe/NiFe and CoFeB. NiFe-based electrodes show magnetization reversal via multi domain switching, which is a delimiting factor for proper device operation. The inclusion of MgO has been shown to increase the switching field and switching field distribution of the contacts. However, CoFe/NiFe and CoFeB diodes show a square-like switching field, featuring a high remanence magnetization. The size-dependence of the switching field is defined by the elements' width rather than their length. Magnetization reversal originates from end domains, generated in the elements' blunted edges. A magnetic selectivity of around 10 Oe, where the magnetization of injector/detector pair show antiparallel magnetic alignment is achieved.

In Chapter 4 the structural and electrical properties of CoFe-based MOS capacitors incorporating $\text{SiO}_2(5\text{nm})$, $\text{SiO}_2(2.5\text{nm})/\text{MgO}(2.5\text{nm})$ and $\text{MgO}(5\text{nm})$ dielectrics have been investigated, with an overall thickness of 5 nm. MgO directly deposited on silicon remains amorphous over the first 1-2 nm, due to the large lattice mismatch to silicon. In contrast, when deposited on thermally grown SiO_2 , MgO crystallizes in a cubic phase with preferred (001) crystallographic orientation. Even for a reduced dielectric thickness of $\text{SiO}_2(1.5\text{nm})/\text{MgO}(1.5\text{nm})$ our investigation shows extended crystallization of the MgO layer, enabling pronounced tunneling transport through the oxide layer. For high temperature annealing up to $550^\circ\text{C}/60 \text{ min}$, no intermixing has been shown, neither with the SiO_2 barrier nor the ferromagnetic CoFe electrode.

The capacitance-voltage characteristics of the different MOS capacitors are signifi-

cantly influenced by their D_{it} values. While capacitors with MgO have a interface trap density as high as $5 \times 10^{13} \text{cm}^{-2} \text{eV}^{-1}$, after annealing at 400°C , MOS capacitors incorporating SiO_2/MgO feature one order of magnitude reduced D_{it} value, which is further reduced by one order of magnitude for pure SiO_2 .

Finally, the carrier transport mechanisms for $\text{MgO}(5\text{nm})$ and $\text{SiO}_2(2.5\text{nm})/\text{MgO}(2.5\text{nm})$ have been compared. For SiO_2/MgO barriers, annealing changes the conduction mechanism from trap-assisted tunneling to Frenkel-Poole emission and Fowler Nordheim tunneling. This change in transport clearly indicates the increase of the oxide integrity after crystallization due to annihilation of the trap states in MgO. In contrast, annealing has barely any effect on the transport properties of the MgO capacitor, where trap assisted tunneling is dominating for all annealing states.

Perspectives

Combining the gained knowledge from this thesis and recent theoretical calculations may facilitate the successful device implementation of a spinFET. Ab initio calculations, treating silicon (001) complex band structure for spin injection from epitaxial $\text{Fe}(001)$, reveal 100% spin polarization for $k_{\parallel} = 0$.¹ This conduction feature is attributed to the Δ_1 symmetry of the Si wave function at the center of the $\text{Si}(001)$ Brillouin zone, blocking the $\text{Fe}(001)$ minority spin channel, which lacks this symmetry feature. In the case of $\text{Fe}(001)/\text{Si}(001)$ Schottky diodes, the conduction

¹Mavropoulos, P. *Phys. Rev. B* **78**, 054446 (2008).

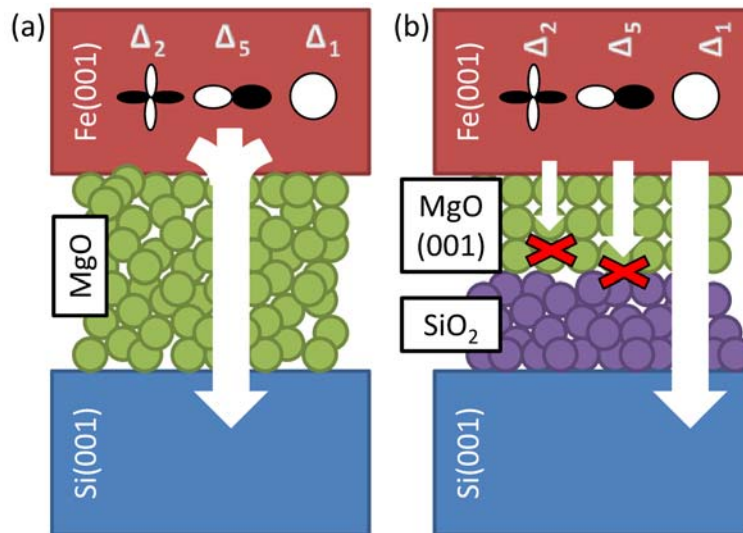


Figure 5.1: Schematic of expected current contributions for spin injection in silicon (001) through (a) amorphous MgO and (b) $\text{SiO}_2/\text{MgO}(001)$ barrier

sites in the band structure are determined by the Fermi level inside the Schottky barrier. Using MgO(001), which is known for its spin filtering properties for the Δ_1 symmetry at $k_{\parallel} = 0$, should rule out the contribution from other conduction sites in the band structure, enhancing the spin injection efficiency to Si. To this end, the achievement of crystalline MgO(001), when deposited on top of thermally grown SiO₂, is believed to be crucial for injection/detection contacts of a spinFET. Fig. 5.1 displays the expected difference in tunneling current contributions for amorphous MgO - where also wave functions with a low spin polarization propagate through the barrier - and SiO₂/MgO(001). For SiO₂/MgO(001) the large attenuation length of the Δ_3 and Δ_5 symmetry wavefunctions, results in a dominant conduction of the highly spin-polarized Δ_1 symmetry. The calculation of the expected MR effect for a two-terminal device structure using SiO₂/MgO(001) contacts is shown in Fig. 5.2. Clearly, the increase of the contacts' spin polarization is increasing the expected magneto current effect, while a shorter length of the transport channel is further boosting the effect. In addition, SiO₂/MgO(001) barriers offer a reduced interface trap density, resulting in lower spin relaxation. As shown in Chapter 3, p-type silicon with a doping density of 10^{15}cm^{-3} leads for both spin injection and spin detection to the most promising results. The results presented in this thesis demonstrate that the close approach of the resistance-area product to the required range, combined with superior dielectric and spin-filtering properties, give the SiO₂/MgO(001) bilayer the highest potential for use as tunnel barrier in spinFET ferromagnetic contacts.

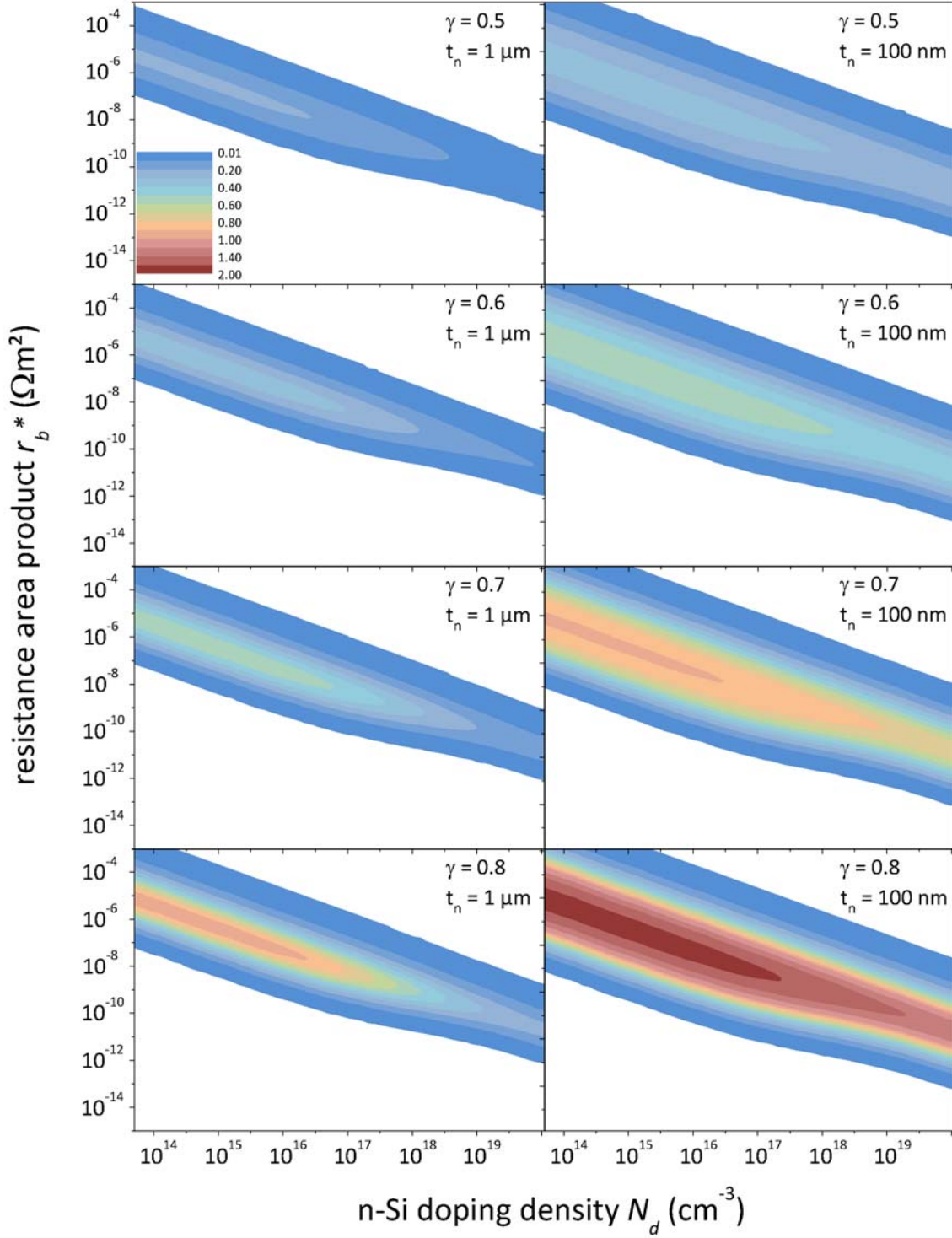


Figure 5.2: Magneto resistance effect of an FM/I/Si/I/FM structure as a function of the silicon doping density, for two channel lengths $t_{sc} = 100\text{nm}$ and $t_{sc} = 1.0\mu\text{m}$ and varying spin asymmetry coefficients of the MgO tunneling barrier $\gamma = 0.5, 0.6, 0.7$ and 0.8 . The calculation employed experimental values for Co, with $r_{fm} = \rho_{fm}l_{sf}^{fm} = 4.5 \times 10^{-15}\Omega\text{m}^2$, $\beta = 0.47$ and $l_{sf}^{fm} = 60\text{nm}$ (the calculations have been carried out using Equ. (23) and (25) from Fert A. and Jaffrès H. *Physical Review B* **64**, 184420 (2001).)

LIST OF FIGURES

0.1	Datta-Das-transistor	3
1.1	Illustration of the different spin relaxation mechanisms	11
1.2	Spin-injection results of Johnson and Silsbee	16
1.3	Magneto-resistance of Fe/Cr multilayers	17
1.4	Schematic of the TMR-effect in a magnetic tunnel junction	19
1.5	Schematic of current contributions through and amorphous and crystalline tunneling barrier	20
1.6	Simplified equivalent circuit for a FM/SC/FM hybrid spin-electronic junction	21
1.8	Comparison of fundamental physical influences at FM/NM interfaces	25
1.9	Calculated MR effects of FM/I/SC/I/FM structures with different geometries	26
1.10	Non-local spin injection results for Fe ₃ Si/Si(111) Schottky diodes . .	28
1.11	Non-local spin injection results for Fe/Al ₂ O ₃ /Si tunneling diodes . . .	29
1.12	Experimental implementation of ballistic spin injection in silicon . . .	30
1.13	Conventional MRAM design	34
1.14	Schematic of a hybrid silicon-based MRAM design	35
2.1	Principle of different TEM modes	47
2.2	Working principle of an atomic force microscope	49
2.3	Different possible magneto-optical measurement setups	51
3.1	Schematic layout of ferromagnetic source and drain contacts to silicon	56
3.2	Processing steps of embedded layer that could explain diodes	58
3.3	AFM images showing an array of contacts and a zoom-in of the ends of the contacts	59
3.4	Plain-view TEM images of NiFe(10 nm)/Ta/Au	60
3.5	High resolution TEM image of a MIS diode edge region	60
3.6	HRTEM images of CoFeB based tunneling diodes	61
3.7	Temperature stability of a CoFeB MIS diodes analyzed by EFTEM . .	61
3.8	Temperature stability of a CoFe MIS diodes analyzed by EFTEM . .	63
3.9	TEM comparison of Schottky and MIS diodes annealed at 400°C . . .	64
3.10	Energy diagram of ideal Schottky and MIS diode	65
3.11	Band diagram of a MIS diode in accumulation, depletion and inversion	67

3.12	Room temperature IV measurements of ferromagnetic Schottky diodes on n-Si(100)	73
3.13	Schottky barrier height and ideality factor of n-Si FM Schottky diodes	74
3.14	Arrhenius plots of the saturation current for n-Si FM Schottky diodes	75
3.15	Room temperature IV measurements and SBH of ferromagnetic MIS diodes with a 1.5 nm MgO tunneling barrier on n-Si(100)	78
3.16	Room temperature IV measurements and SBH of ferromagnetic MIS diodes with a 2.5 nm MgO tunneling barrier on n-Si(100)	79
3.17	Arrhenius plots of the reverse current for a 1.5nm MgO tunneling barrier	80
3.18	Room temperature IV measurements of ferromagnetic Schottky diodes on p-Si(100)	83
3.19	Schottky barrier height and ideality factor of p-Si FM Schottky diodes	84
3.20	Arrhenius plots of the saturation current for p-Si FM Schottky diodes	85
3.21	Room temperature IV measurements and SBH of ferromagnetic MIS diodes with a 1.5 nm MgO tunneling barrier on p-Si(100)	87
3.22	Room temperature IV measurements and SBH of ferromagnetic MIS diodes with a 2.5 nm MgO tunneling barrier on p-Si(100)	88
3.23	Arrhenius plots of the reverse current for a p-Si MIS diode with 1.5nm MgO	89
3.24	Schottky barrier height and activation energy of CoFeB based p-Si Schottky and MIS diodes	90
3.25	Extracted resistance area values for n-Si MIS diodes with CoFe electrodes	92
3.26	Extracted resistance area values for p-Si MIS diodes with CoFe electrodes	93
3.27	CV-characteristics of CoFe/MgO/n-Si MIS diodes	94
3.28	Extracted interface trap density for a CoFe-based n-Si MIS diode . .	95
3.29	MOKE measurements of MIS diodes with different ferromagnetic electrodes	97
3.30	Magnetic switching characteristics of CoFe/NiFe bilayer contacts . . .	98
3.31	Magnetic switching characteristics of CoFe/NiFe bilayer contacts . . .	99
3.32	Switching characteristics of contact employing CoFeB	100
3.33	MOKE loops for CoFe/NiFe and CoFeB based contacts for different annealing conditions	100
3.34	MFM images of injector/detector pairs after at different magnetic fields	101
4.1	Individual processing steps for MOS capacitors	111
4.2	Structural stability of MgO on thick thermal SiO ₂	113
4.3	HRTEM images of MOS capacitors with MgO and SiO ₂ /MgO dielectrics	114
4.5	Schematic measurement setup of MOS capacitors	116
4.6	CV measurements of MgO-based MOS capacitors	118
4.7	D _{it} measurements of MgO-based MOS capacitors	120
4.8	Band diagrams of different conduction mechanisms through oxide barriers	123

4.9	JV characteristics of MgO and SiO ₂ /MgO MOS diodes along with respective Fowler-Nordheim and Frenkel-Poole plots	124
5.1	Schematic of the expected current contributions for spin injection in silicon (001) through an amorphous MgO and a SiO ₂ /MgO(001) barrier	132
5.2	Calculated MR effects of FM/I/SC/I/FM for silicon as a function of the doping density and the spin asymmetry	134

LIST OF TABLES

1.1	Comparison of MRAM features with other memory technologies . . .	33
3.1	Energy band parameters for ferromagnetic Schottky and MIS diodes .	69
3.2	Description of the fabricated diode systems for the magnetic characterization	95
3.3	Magnetic configuration of injector/detector pairs as a function of the applied field	102
4.1	Characteristic properties of MgO-based MOS capacitors	121

ACKNOWLEDGEMENTS

Prof. Dr. Jürgen Smoliner for his excellent advisory and help to manage the thesis and courses at the same time. Thanks for always being there for discussions and his help with the cryo measurement setup.

Prof. Dr. Christoph Eisenmenger-Sittner from the *Solid State Physics Institute* for reviewing this thesis and discussion.

Dr. Theo Dimopoulos for ... that's gonna be a long list: his excellent guidance through this thesis, long clarifying discussions, his endless patience, new ideas for experiments, the ability to motivate for new tracks and most of all his permanent optimism. Thanks for guiding me through this learning process of a PhD thesis. I also would like to thank you and your family for the many fun hours beside work.

Priv. Doz. Dr. Hubert Brückl for giving me the opportunity to do my PhD thesis in his group and his great support.

Dr. Amit Kohn, Dr. Vlado Lazarov, Dr. Andras Kovacs and *Dr. Daniel Kirk* from *Oxford Materials* for their support in TEM characterization and scientific discussions.

Dr. Manfred Rührig and *Dr. Ludwig Bär* from Siemens CT in Erlangen for their experimental support in the beginning of the thesis.

Dr. Jehyun Lee and *Prof. Dr. Josef Fidler* for their TEM support and the interesting TEM seminar at the USTEM in Vienna.

Dr. Thomas Meier, Dr. Jörg Schotter, Dr. Michael Kast and *Dr. Christoph Stepper* for experimental support and many helpful discussions.

Finally the whole department Nano-Systems at the AIT, especially *Moritz, Astrit, Philipp, Stefan, Paul, Roman, Kerstin* and *Leoni* for the great time at work with lot of fruitful discussions and also the fun times aside work.

Daniel Schwarz for his great support during his Diploma Thesis on spin injection in silicon, very nice discussions and the fun we shared.

Last but not least my parents *Walter and Luise* for their endless love and support throughout my study. My sister *Judith* and brother *Stefan* for their support.

Most probably my biggest thanks goes to my girlfriend *Christine* for her love and support, giving me the energy to go on and all her patience until this thesis was finalized.

CURRICULUM VITAE

Personal Data

Name	Thomas Uhrmann
Address	Hochstr. 11, 94121 Salzweg, Germany
Date of birth	05/28/1982
Place of Birth	Hutthurm, Germany
Nationality	german

Education

01/2006 - 05/2010	Dr. Tech. in Electrical Engineering, Institute of Solid State Electronics, Technical University of Vienna, Vienna, Austria
10/2001 - 11/2005	Dipl.Ing.(FH) in Mechatronics, University of Applied Science Regensburg, Regensburg, Germany
09/1992 - 08/2001	Gymnasium Untergriesbach, Untergriesbach, Germany
09/1989 - 08/1992	Volksschule Wegscheid, Wegscheid, Germany

Professional Experience

since 01/2010 Business Development Manager at EV Group.

01/2006 - 12/2009	Ph.D. thesis at the AIT Austrian Institute of Technology (Nano-Systems) and the Technical University of Vienna (Institut of Solid State Electronics): "Evaluation of sputter-deposited MgO-based tunneling diodes for silicon spintronics", Advisors: Jürgen Smoliner, Theodoros Dimopoulos, Hubert Brückl.
--------------------------	---

- 03/2005 - 11/2005** Diploma Thesis at Siemens AG, Corporate Technology (Materials and Microsystems) Erlangen, Germany: "GMR (Giant Magneto Resistance) Sensoren auf polymerem Trägermaterial", Advisors: Ludwig Bär, Manfred Rühlig, Alfred Lechner.
- 02/2004 - 08/2004** Internship with OSRAM Opto Semiconductors Inc., San Jose, California, USA, Advisors: Rahul Gupta, Franky So.
- 10/2002 - 01/2003** Internship with Infineon Technologies AG, Regensburg, Germany, Advisor: Uwe Höcke.